Optimisation of photon detector tynode membranes using electron-matter scattering simulations

Theulings, A.M.M.G.

DOI
10.4233/uuid:fd01db04-7432-443f-9c00-49d66db1ab2c

Publication date
2020

Document Version
Final published version

Citation (APA)
Theulings, A. M. M. G. (2020). *Optimisation of photon detector tynode membranes using electron-matter scattering simulations*. [Dissertation (TU Delft), Delft University of Technology]. https://doi.org/10.4233/uuid:fd01db04-7432-443f-9c00-49d66db1ab2c

Important note
To cite this publication, please use the final published version (if applicable).
Please check the document version above.

Optimisation of photon detector tynode membranes using electron-matter scattering simulations

Optimisation of photon detector tynode membranes using electron-matter scattering simulations

Proefschrift

ter verkrijging van de graad van doctor
aan de Technische Universiteit Delft,
op gezag van de Rector Magnificus prof. dr. ir. T.H.J.J. van der Hagen,
voorzitter van het College voor Promoties,
in het openbaar te verdedigen op dinsdag 29 september 2020 om 15:00 uur

door

Anne Marguerite Marie Ghislaine Theulings

Ingenieur der Technische Natuurkunde,
Technische Universiteit Delft, Delft, Nederland,
geboren te Groningen, Nederland.

Dit proefschrift is goedgekeurd door de

promotor: prof. dr. ir. H. van der Graaf
promotor: dr. C.W. Hagen

Samenstelling promotiecommissie:

Rector Magnificus,	voorzitter
Prof. dr. ir. H. van der Graaf,	Technische Universiteit Delft
Dr. C.W. Hagen,	Technische Universiteit Delft

Onafhankelijke leden:

Dr. J.M. Smedley,	State University of New York at Stonybrook
Prof. dr. ing. B. van Eijk,	Universiteit Twente
Dr. A. Caviglia,	Technische Universiteit Delft
Prof. dr. P. Dorenbos,	Technische Universiteit Delft
Prof. dr. ir. C. Vuik,	Technische Universiteit Delft

Het leven is toch een groot mysterie?
Ik snap er tenminste geen donder van.

Tonke Dragt

Samenvatting

Het doel van het onderzoek beschreven in dit proefschrift was het ontwikkelen van een simulatiepakket dat gebruikt kan worden voor het ontwerpen van de **Ti**med **P**hoton **C**ounter (TiPC). De TiPC is een detector voor individuele laagenergetische fotonen. Het werkingsprincipe van de TiPC berust op de vermenigvuldiging van een elektronen signaal door transmissie dynodes, oftewel tynodes. De uitvoerbaarheid van de TiPC hangt af van de mogelijkheid om tynodes te ontwikkelen met een voldoende hoge secundaire elektronenopbrengst. Hierom is het nodig om tynodes te ontwikkelen welke een secundaire elektronenopbrengst hebben van 4 of meer secundaire elektronen per primair elektron. De primaire elektron energie die hier voor nodig is, ligt bij voorkeur zo laag mogelijk.

Het is natuurlijk mogelijk om veel verschillende prototypes te maken voor de tynodes en al deze prototypes te testen door de secundaire elektronenopbrengst te meten. Echter, het is niet heel efficiënt om alle mogelijke ontwerp opties voor de tynodes af te gaan, omdat de secundaire elektronenopbrengst afhangt van zowel het materiaal als de geometrie van de tynode. Het is veel efficiënter om Monte Carlo simulaties te gebruiken om een onderbouwde keuze te kunnen maken voor het fabriceren van een beperkt aantal prototypes, om zo tot het optimale prototype te komen.

Het in dit proefschrift beschreven werk is begonnen met het Monte Carlo simulatiepakket dat door Kieft en Bosch [1] ontwikkeld is. Tijdens het onderzoek is dit simulatiepakket verder ontwikkeld en zijn verbeteringen in het model voorgesteld en doorgevoerd. In dit geval gaat het om verbeteringen van de modellen voor elastische en inelastische interacties van elektronen

met vaste stoffen alsmede van het model dat bepaalt of een elektron van het ene naar het andere materiaal gaat wanneer het de grens tussen deze twee materialen bereikt. Vervolgens is voor silicium, goud en aluminiumoxide onderzocht wat het effect van de modelverbeteringen was. Hoewel de nieuwe modellen fysisch correcter zijn dan de oorspronkelijke modellen van Kieft en Bosch, waren de nieuwe modellen toch iets slechter in het reproduceren van experimentele secundaire elektron emissie curves van silicium en goud dan de originele modellen van Kieft en Bosch. De curves van aluminiumoxide werden juist beter gereproduceerd door de verbeterde modellen dan de originele modellen. Er zitten echter haken en ogen aan het vergelijken van gesimuleerde waarden met experimentele waarden doordat het niet altijd duidelijk is wat de exacte toestand van het materiaaloppervlak is en doordat niet altijd goed is omschreven of er rekening is gehouden met oplaadeffecten in het geval van isolatoren en halfgeleiders. Een andere aanpassing die gedaan is aan het simulatiepakket is het opsplitsen van de berekeningen van de botsingsdwarsdoorsnedes aan de ene kant en de daadwerkelijke Monte Carlo simulatie aan de andere kant. Door hier twee losse pakketten van te maken, hoeven de dwarsdoorsnedes nog maar één keer berekend te worden per materiaal, in plaats van telkens wanneer een nieuwe simulatie wordt gestart.

Het nieuwe simulatiepakket is vervolgens gebruikt om de transmissie secundaire elektronenopbrengst te berekenen voor aluminiumoxide membranen van verschillende diktes. De simulatieresultaten gaven inzicht in de verschillen tussen reflectie en transmissie secundaire elektronenemissie en toonden aan dat de transmissie secundaire elektronenopbrengst altijd lager is dan de reflectie secundaire elektronenopbrengst. Met de simulaties was het bovendien mogelijk om de membraandikte te optimaliseren zodat de hoogste transmissie secundaire elektronenopbrengst werd verkregen. Voor aluminiumoxide membranen ligt de optimale dikte rond de 8 nm.

Om een specifiek materiaal te simuleren, zijn natuurlijk de materiaal parameters nodig. Een van de materiaal parameters is de zogenaamde energieverliesfunctie. Dit kan echter een zeer lastige parameter zijn om te vinden of te weten te komen. Bijvoorbeeld in het geval van silicium rijk siliciumnitride met verschillende doteringsniveaus. In deze gevallen is gebruik gemaakt

van het dichtheidsfunctionaaltheorie formalisme om de energieversliesfunctie *ab initio* te berekenen en deze vervolgens te gebruiken in het Monte Carlo simulatiepakket. Door het gebruik van het dichtheidsfunctionaaltheorie formalisme is het mogelijk om te samenstelling en de moleculaire structuur van het gesimuleerde materiaal zeer precies te bepalen.

Verder is een poging gedaan om experimenteel de secundaire elektronenopbrengst van silicium rijk siliciumnitride te bepalen met behulp van Röntgen foto-elektronenspectroscopie. De onderzochte substraten hadden verschillende doteringsniveaus van silicium en verschillende oppervlakte structuren. De resultaten konden echter niet gebruikt worden op de van te voren verwachtte manier om een kwantitatieve waarde voor de reflectie secundaire elektronenemissie te verkrijgen. De resultaten konden wel gebruikt worden om kwalitatief te kunnen vaststellen dat een oppervlakte beëindiging met waterstof de secundaire elektronenopbrengst van silicium rijk siliciumnitride verhoogt. Er is getracht de experimentele spectra verkregen met Röntgen foto-elektronenspectroscopie te reproduceren met het simulatiepakket. De gesimuleerde spectra vertoonden significante verschillen met de experimentele spectra. Het meenemen van de resolutie en openingshoek van de experimentele detector in de simulaties heeft een deel van de verschillen overbrugd, andere verschillen bleven zichtbaar. Dit maakt duidelijk dat het simulatiepakket niet is geoptimaliseerd voor het simuleren van een foton als primair deeltje.

Uiteraard is het simulatiepakket ook gebruikt voor het daadwerkelijke doel waarvoor het ontwikkeld is: de membraandikte van magnesiumoxide membranen is geoptimaliseerd door transmissie secundaire elektronenopbrengst curves te simuleren voor magnesiumoxide membranen van verschillende diktes. Magnesiumoxide staat er om bekend dat het last kan hebben van oplaadeffecten. Om deze reden zijn twee verschillende opties onderzocht met het simulatiepakket; onbehandelde magnesiumoxide membranen en magnesium oxide membranen met een chroom laag van 1 nm dikte aan de reflectie zijde van het membraan. De optimale membraan dikte bleek 17 nm voor onbehandeld magnesiumoxide, met een optimale primaire energie, de energie nodig voor het behalen van de maximale secundaire elektronenopbrengst,

van 1300 eV. Wanneer het magnesiumoxide is voorzien van een dunne laag chroom, bleek de optimale membraan dikte 19 nm (+ 1 nm chroom), met een optimale primaire energie van 1550 eV.

Over het geheel genomen is het gelukt om een veelzijdig simulatiepakket te ontwikkelen dat gebruikt kan worden voor het ontwerpen van prototypes voor de tynodes. Het simulatiepakket kan gebruikt worden voor het optimaliseren van de membraan dikte voor de tynodes en geeft een indicatie van de primaire elektron energie die nodig is om de maximale secundaire elektronenopbrengst te verkrijgen. Echter, de simulatieresultaten van de secundaire elektronenopbrengst kunnen momenteel alleen kwalitatief gebruikt worden en niet kwantitatief. Er is meer werk nodig om het simulatiepakket verder te ontwikkelen zodat ook deze simulatieresultaten kwantitatief gebruikt kunnen worden.

Summary

The object of this thesis work was to develop a (Monte Carlo) simulation package that can be used to aid in the design of the **Ti**med **P**hoton **C**ounter (TiPC). The TiPC is a single photon detector whose working principle is based upon the multiplication of an electron signal by transmission dynodes, or tynodes. For TiPC to be feasible, it is necessary to develop tynodes that have a secondary electron yield of more than 4, preferably with a primary electron energy as low as possible.

In theory it is possible to make many prototype tynodes and test them all by measuring their secondary electron yield curves. However, this would be a time consuming and not very cost effective process, since the secondary electron yield of a tynode depends on many material and geometrical parameters. To investigate the whole parameter space is hardly feasible. Monte Carlo simulations are ideally suited to this case and can be used to narrow down the parameter space significantly.

In this thesis the Monte Carlo simulation package developed by Kieft and Bosch [1] was further developed. Model improvements to the elastic scattering, inelastic scattering and boundary crossing models were proposed and implemented and the effects of the model improvements were investigated for silicon, gold and alumina. Although the original models contained some errors and phenomenological parameters which are no longer present in the new models, the new models did slightly worse for silicon and gold and far better for alumina in reproducing experimental yield curves than the original models of Kieft and Bosch. However, comparing simulated values to experimental values can be tricky due to unknown or undocumented sur-

face conditions in the experiments and due to charging effects in the case of insulators and semiconductors. The simulation package was also split up into two modules to speed up the starting up of a simulation. Now the cross sections are calculated in a different package, so that the cross sections only need to be calculated once per material instead of once for every simulation.

Once the simulation package was in place, it was used to calculate the transmission secondary electron yield of alumina membranes of different thickness. The simulation results gave insight in the differences between reflection and transmission secondary electron emission and showed that the transmission secondary electron yield is always lower than the reflection secondary electron yield. With the simulations it was possible to optimise the membrane thickness to obtain the highest transmission secondary electron yield. The maximum transmission secondary electron yield was obtained for an 8 nm thick membrane.

In order to run a simulation with the simulation package, material parameters are necessary. One of these is the energy loss function. This function is not always known, for example in the case of silicon rich silicon nitride with different silicon doping levels. In this work we have shown that it is possible to use *ab initio* calculated energy loss functions from density functional theory in the simulation package. With the use of these calculated energy loss functions, it is possible to control the composition and the molecular structure of the simulated material very precisely.

In an attempt to obtain experimental results for the secondary electron yield of the different forms of silicon rich silicon nitride that were investigated, X-ray photoelectron spectroscopy (XPS) was performed on silicon rich silicon nitride samples with different doping levels and surface terminations. The results could not be used in the way that was intended when designing the experiments, i.e. obtaining a quantitative measure for the reflection secondary electron yield. However, the results pointed out that hydrogen termination does increase the secondary electron yield of silicon rich silicon nitride as expected. The simulation package was also used in an attempt to reproduce the experimental XPS spectra, although it was not specifically designed for this. The initial results had many differences with the exper-

imental spectra. Taking the detector resolution and opening angle of the experimental detector into account in the simulation results bridged some of the differences, but not all. This pointed out that although it is possible to simulate a photon as primary particle in the simulation package, the models are not optimised for this kind of simulation.

Finally, the simulation package was used for the purpose it was designed for: the transmission secondary electron yield curves for magnesium oxide membranes with different thicknesses were simulated in order to determine the optimum membrane thickness. Since magnesium oxide is known to suffer from charging effects, two different cases were investigated; uncoated magnesium oxide and chromium coated magnesium oxide. For uncoated magnesium oxide, the optimum thickness is 17 nm, the optimum primary energy was 1300 eV. The chromium coated magnesium oxide had a 1 nm chromium coating on the top (reflection) side of the membranes. In this case, the optimum thickness was 19 nm (+ 1 nm chromium), and the optimum primary energy was 1550 eV.

Overall the goal of developing an all-round simulation package to aid in the design of the prototype tynodes was reached. The simulation package can be used to optimise the membrane thickness for prototype tynodes and it gives an indication of the primary energy necessary to obtain the maximum secondary electron yield. However, more work is needed if one is interested in a simulation package that can predict the exact secondary electron yield of a material quantitatively.

Contents

Introduction

Photomultiplier tubes are in use since their invention in the 1930s due to their efficiency, time resolution and low noise characteristics. The one application where they cannot be used is in a (dynamic) magnetic field. The **Ti**med **P**hoton **C**ounter (TiPC) proposed in [2–4] is a single photon detector with high spatial and temporal resolution that does have the ability to work in dynamic magnetic fields. A more detailed description will be given in Chapter 1. For now it suffices to know that a crucial part of the TiPC are its tynodes; thin membranes that act as transmission dynodes instead of reflection dynodes as in a photomultiplier tube.

For multiple materials such as silicon nitride and alumina, there exist methods to fabricate MEMS membranes [5,6]. However, when the fabrication of tynodes of a different material is required, it is not sufficient to simply use the exact same fabrication process as for silicon nitride, for example, and substitute the material of interest. Instead, a specific fabrication process needs to be developed for each material. Since this can be a very complicated process, it is preferred to simulate the yield curves of thin membranes for different materials in order to choose a few promising candidate materials for the tynodes. The purpose of this thesis research is to develop a simulation package that is able to simulate the transmission secondary electron yields of tynode prototypes to be used for TiPC.

In order to simulate the (transmission) secondary electron yield of a membrane, we need to track all primary electrons and the secondary electrons created by the primary electrons inside the membrane until they are either absorbed or emitted. The simulation package needs to be able to do this for

different kinds of materials, such as metals, insulators and semiconductors, so we can predict the (transmission) secondary electron yield for different material candidates. Monte Carlo methods are ideally suited in this case as the effect of different material parameters on the yield can be simulated without the need for fabrication of a wide variety of samples. In order to accurately simulate the electron transport and the production of secondary electrons, models of the electron interactions with the solid state are needed down to a few eV. In this project we started with the Monte Carlo simulation package developed by Kieft and Bosch [1], based upon GEANT4 [7]. The models in the original simulation package as well as the improved models we developed are discussed in Chapter 2 and the effects of the model improvements are discussed in Chapter 3.

Once the simulation package is introduced, we will use it to simulate the transmission secondary electron yield of alumina membranes (Chapter 4). We will also use the simulation package in combination with density functional theory to simulate the reflection yield curves for silicon rich silicon nitride (SRN) for different doping levels and dopant distributions and including hydrogen contamination in the bulk of some of the samples (Chapter 5).

We have attempted to determine the secondary electron yield of SRN by the use of X-ray photoelectron spectroscopy (XPS). These experiments did not give the result we were expecting, and are discussed in Chapter 6. In Chapter 6 we also discuss simulations of XPS spectra of SRN. The simulation package is able to simulate photons as primary particles to some extent, however, it is not designed for this purpose. So we would like to warn the reader beforehand that these simulations will not give accurate results.

Finally we use the simulation package for the purpose it was designed for: we use it to design prototype tynodes of magnesium oxide in Chapter 7.

Chapter 1

The Timed Photon Counter

The **Ti**med **P**hoton **C**ounter (TiPC) proposed in [2–4] is a single photon detector with high spatial and temporal resolution as mentioned previously. The TiPC consists of a stack of thin transmission dynodes (tynodes) on top of a pixel chip, the whole is capped by a photocathode, see Figure 1.1 for a schematic representation of the TiPC. When the photocathode collects a photon, the emitted photoelectron is accelerated towards the first tynode. This tynode is a thin membrane such that a high energy incoming electron from the top results in multiple low energy electrons emitted at the bottom. Now the low energy emitted electrons are accelerated to the second tynode and the multiplication process repeats. After the last tynode, the electrons hit a pixel input pad on the pixel chip and the signal is detected.

The pixel input pads of a Timepix chip can detect signals starting from 1000 electrons [8]. A feasible amount of tynodes to stack on top of the pixel chip would be five tynodes. In order to have a signal of 1000 electrons, the multiplication per tynode should be at least 4. The device could work with a smaller multiplication per tynode, but this will result in the need for more tynodes stacked on top of each other, complicating the fabrication of the device. The emitted electrons are accelerated towards the next tynode by putting a voltage between the tynodes. Ideally this voltage would be as low as possible. This voltage can be increased if necessary, up to some point. Increasing the voltage too far may lead to electrical breakdown, which
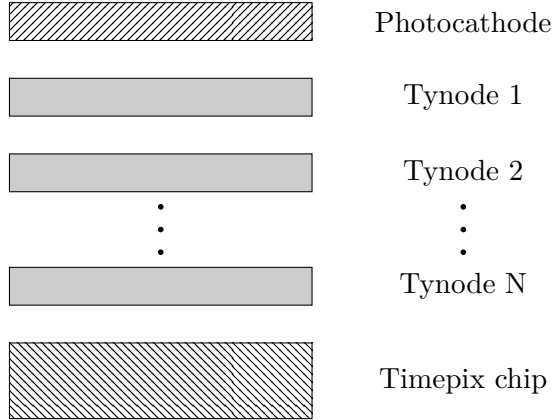
Figure 1.1: Schematic of the **Ti**med **P**hoton **C**ounter.

could destroy the device altogether. The distance between the tynodes will preferably be in the order of 20 to 200 µm. Giere *et al* determined that breakdown occurs in high vacuum for field strengths of 20 to 40 kV/mm depending on the shape of the electrodes [9]. If breakdown would happen at a field strength of 20 kV/mm, we would need a 25 µm spacing between the tynodes for a 500 V voltage between the tynodes. If the voltage needs to be larger, the spacing between the tynodes can of course be increased, however, this would decrease the time resolution of the TiPC.

The TiPC will be able to work in dynamic magnetic fields as opposed to the traditional photomultiplier tubes, for two reasons: (1) the spacing between the tynodes will be in the order of 50 µm, which results in an electric field of $1 \cdot 10^7$ V/m at a voltage of 500 V. Now the magnetic field can be up to 0.75 Tesla and the Lorentz force on a 500 eV electron (with its velocity perpendicular to the magnetic field) would still only be equal to the electric force on the electron. (2) the tynodes are slightly curved, resulting in a focussing effect of electrons towards the next tynode. A micro channel plate (MCP) will also work in a magnetic field and can have a spatial resolution comparable to the TiPC. However, during the multiplication of the electron signal, the high energy electrons can release ions from the MCP walls. Especially near the end of the MCP, when the electron signal becomes

larger, more ions will be created. These ions will be accelerated towards the photocathode by the electric field necessary for the electron multiplication. This ion feedback will cause the photocathode to degrade quickly. While in the TiPC, only ions created by the first tynode can reach the photocathode. Ions created by the other tynodes will be captured by the tynode above it. Since the signal that hits the first tynode is very small the amount of ions created will be even smaller and the photocathode will not degrade as quickly as with a MCP.

In the next Chapter we will address the theory of electrons interacting with the tynode materials, resulting in the emission of secondary electrons.

Chapter 2

Theory

In chapter 1 the design of the **Ti**med **P**hoton **C**ounter was discussed. The secondary electron yield of the transmission dynodes is essential to this design. Simulations can be used to determine which materials are possible candidates to use as transmission dynode material and which materials will not be useful for this purpose. Mainly Monte Carlo simulations are useful here, where a simulated sample is irradiated with an electron beam and the primary and secondary electrons are tracked inside the sample until they are either emitted through a surface or absorbed inside the sample. In order to perform such simulations, first models to determine the interactions of electrons inside a material need to be developed. The Monte Carlo simulator developed by Kieft and Bosch [1], based on GEANT4 [7], was the starting point of this work. In the first part of this chapter, the models used by Kieft and Bosch as well as the final models we used, will be discussed. A large part of the final models is already discussed in the thesis of Thomas Verduin [10], here we repeat parts of this derivation to highlight the differences between the original models as developed by Kieft and Bosch [1] and the models as used for the calculations in this thesis. In chapter 3 we will discuss the effects the model changes have on the simulated yields.

Part of this work includes experimental results and simulations of X-ray photoelectron spectroscopy, in this case the primary particles are photons. These photons will be absorbed by atoms in the material. An electron will

be emitted in the process and the atom may be left in an excited state. If the atom is left in an excited state, the atom will de-excite, possibly emitting an X-ray photon or an electron in the process. The models used for absorbing photons and de-excitation of the excited atoms will be discussed in the second part of this chapter.

2.1   Electron models

An electron travelling in vacuum will travel in a straight line if there are no electric or magnetic fields present. However, inside a material, the electron will feel the electric potential of the nuclei and electrons that make up the material. The electron can then undergo two types of scattering events inside the material. It can scatter on an atom without losing any energy, an elastic scattering event, or it can scatter on an atom and lose energy, an inelastic scattering event. In the case of an inelastic scattering event, the energy the electron loses has to go somewhere, of course. The energy transfer to the nucleus will be negligible, because the nucleus is so much heavier than the electron. So in practice, the energy will be transferred to one of the electrons around the nucleus. This will result in a secondary particle being created, which in turn will also be able to travel through the material, leaving the atom in an excited state. The vast majority of these secondary particles will be electrons, however, with a significantly smaller probability, an X-ray photon can also be created if the energy loss of the primary electron is high enough. This X-ray photon will in turn be absorbed in the material, as will be discussed in 2.2.1.

The probabilities for an elastic and inelastic scattering event to happen are governed by the cross sections for the specific material the electron travels through. The models used to calculate the elastic scattering cross sections are discussed in 2.1.1, the models for inelastic scattering cross sections in 2.1.2. When the electron encounters a barrier between two materials, one of which could be vacuum, there is a third process that can happen; the electron can traverse the boundary, or it can reflect on the boundary, this is discussed in 2.1.3. The electron cannot travel through the material infinitely, because

it gradually loses its energy due to the inelastic scattering events. At some point the energy of the electron becomes so low that it will be absorbed in the material.

The elastic and inelastic processes both have their energy dependent mean free paths to determine the distance an electron can travel on average before this process occurs. The probability that nothing happens when an electron travels a certain distance decreases exponentially with the travelled distance r

$$P(E,r) = \lambda_T^{-1}(E)e^{-r/\lambda_T(E)}, \tag{2.1}$$

where $\lambda_T(E)$ is the total mean free path

$$\lambda_T^{-1}(E) = \sum_i \lambda_i^{-1}(E), \tag{2.2}$$

where $\lambda_i(E)$ are the separate mean free paths of all possible interactions an electron can undergo in the material. In order to sample the distance an electron travels before it undergoes any interaction, we need the cumulative probability depending on distance travelled

$$P(E,r' \leq r) = \int_0^r \lambda_T^{-1}(E)e^{-r'/\lambda_T(E)}\,dr' = 1 - e^{-r/\lambda_T(E)}. \tag{2.3}$$

The actual sampling of the distance is done by drawing a random number U from a uniform distribution between 0 and 1 and finding the distance r that corresponds to this probability given by equation 2.3

$$U = 1 - e^{-r/\lambda_T(E)}. \tag{2.4}$$

Rewriting this, using the fact that $1 - U = U$ for a uniform distribution, gives

$$r = -\lambda_T(E)\ln U \tag{2.5}$$

Now we know the distance an electron will travel before it undergoes any interaction. The next step is to determine which interaction the electron undergoes. This is done with the respective mean free paths for all possible interactions. Suppose there are three different types of interactions, a, b and

c. To determine which interaction the electron undergoes, we can use the following

$$
\begin{cases}
U \leq \frac{\lambda_a^{-1}}{\lambda_T^{-1}}, & \text{perform } a \\
\frac{\lambda_a^{-1}}{\lambda_T^{-1}} \leq U \leq \frac{\lambda_a^{-1} + \lambda_b^{-1}}{\lambda_T^{-1}}, & \text{perform } b \\
\frac{\lambda_a^{-1} + \lambda_b^{-1}}{\lambda_T^{-1}} \leq U \leq \frac{\lambda_a^{-1} + \lambda_b^{-1} + \lambda_c^{-1}}{\lambda_T^{-1}} = 1, & \text{perform } c.
\end{cases}
\tag{2.6}
$$

In this case, we have two different interactions the electron can undergo after travelling distance r, elastic and inelastic scattering, with mean free paths $\lambda_e(E)$ and $\lambda_i(E)$, respectively. In 2.1.1 and 2.1.2 we will discuss how to determine $\lambda_e(E)$ and $\lambda_i(E)$.

2.1.1   Elastic scattering

During an elastic scattering event, the electron will scatter on the potential of a nucleus in the material. The direction of the electron will change in this scattering event. There will also be an energy loss for the electron, due to atomic recoil. However, this energy loss will be very small and will be ignored for now, so that the scattering event can be considered elastic. The elastic mean free path $\lambda_e(E)$ can be calculated from the cross section $\sigma_e(E)$ by

$$
\lambda_e^{-1}(E) = \int_0^{2\pi} \int_0^{\pi} \frac{\partial \sigma_e(E)}{\partial \Omega} \sin\theta \, d\theta \, d\phi.
\tag{2.7}
$$

To determine the angular differential cross section $\frac{\partial \sigma_e(E)}{\partial \Omega}$ we use the Mott cross sections [11,12]. The Mott cross sections are derived by using the Dirac equation for an electron moving in an external electric field. Typically the electrons we are interested in have low energies and can be considered non-relativistic. However, the Dirac equation is a relativistic equation, so why not use the Schrödinger equation, which is non-relativistic? This can be answered by reasoning that an electron scattering on an atom will be accelerated towards the atom before the interaction takes place. Especially in the case of heavier elements, this acceleration leads to speeds of the electron where relativistic effects need to be taken into account [11]. The Dirac equation for a particle in a spherical potential $V(r)$ in natural units ($\hbar = c = m_e = 1$) is

given by

$$[W - \boldsymbol{\alpha} \cdot \mathbf{p} - \beta - V(r)]\, \phi(\mathbf{r}) = 0, \tag{2.8}$$

where W is the total energy of the particle in units of mc^2 and the length r is in units of $\hbar/m_e c$. $\boldsymbol{\alpha}$ and β are given by the standard representation

$$\boldsymbol{\alpha} = \begin{bmatrix} 0 & \boldsymbol{\sigma} \\ \boldsymbol{\sigma} & 0 \end{bmatrix},$$
$$\beta = \begin{pmatrix} I & 0 \\ 0 & -I \end{pmatrix}, \tag{2.9}$$

where $\boldsymbol{\sigma}$ are the Pauli matrices and I is the identity matrix. This leads to two sets of two coupled first-order differential equations [11]

$$[W - V(r) + 1]\, F_n^{\pm}(r) + \frac{dG_n^{\pm}(r)}{dr} + \frac{1+k}{r} G_n^{\pm}(r) = 0,$$
$$- [W - V(r) - 1]\, G_n^{\pm}(r) + \frac{dF_n^{\pm}(r)}{dr} + \frac{1-k}{r} F_n^{\pm}(r) = 0. \tag{2.10}$$

Here the plus and minus signs denote the spin up and spin down case. In the case where $V(r) \approx 0$ for large r, the solution for $G_n^{\pm}(r)$ is given by

$$G_n^{\pm}(r) = J_n(Kr)\cos\eta_n^{\pm} - T_n(Kr)\sin\eta_n^{\pm}, \tag{2.11}$$

where $J_n(Kr)$ and $T_n(Kr)$ are Bessel and Neumann functions, $K^2 = W^2 - 1$ and η_n are the Dirac phase shifts. This leads to the scattering factors

$$f(\theta) = \frac{1}{2iK} \sum_{n=0}^{\infty} \{(n+1)[\exp(2i\eta_n^+) - 1] + n[\exp(2i\eta_n^-) - 1]\} P_n(\cos\theta),$$
$$g(\theta) = \frac{1}{2iK} \sum_{n=1}^{\infty} \left[\exp(2i\eta_n^-) - \exp(2i\eta_n^+)\right] P_n'(\cos\theta),$$
$$\tag{2.12}$$

where P_n and P_n' are the ordinary and associated Legendre polynomials. The angular differential cross sections for an unpolarised beam are now calculated as follows

$$\frac{\partial\sigma}{\partial\Omega} = |f(\theta)|^2 + |g(\theta)|^2 \tag{2.13}$$

The exact potential $V(r)$ that is used in this derivation will in the end determine the appropriateness of the Mott cross sections calculated. An approximation to the potential in a solid, is the potential due to one single free atom. However, in a solid many atoms are close to one another and the potential will change accordingly, as can be imagined. The first order approximation of the potential in a solid, is the muffin-tin potential [13]. In their Monte Carlo simulator, Kieft and Bosch used the Mott cross sections calculated by Czyżewski [11]. Although Czyżewski mentions the muffin-tin potential, Kieft and Bosch used values for the Mott cross sections calculated without taking solid state effects into account. However, we used Mott cross sections calculated with solid state effects taken into account. The Mott cross sections we used are calculated using ELSEPA [14]. The resulting mean free paths for silicon, calculated with the Mott cross sections used by Kieft and Bosch and calculated with the ELSEPA Mott cross sections, are compared in Figure 2.1. The material parameters used in the calculations of these mean free paths and the other mean free paths in this chapter, are given in appendix A. The new mean free path is slightly higher than the
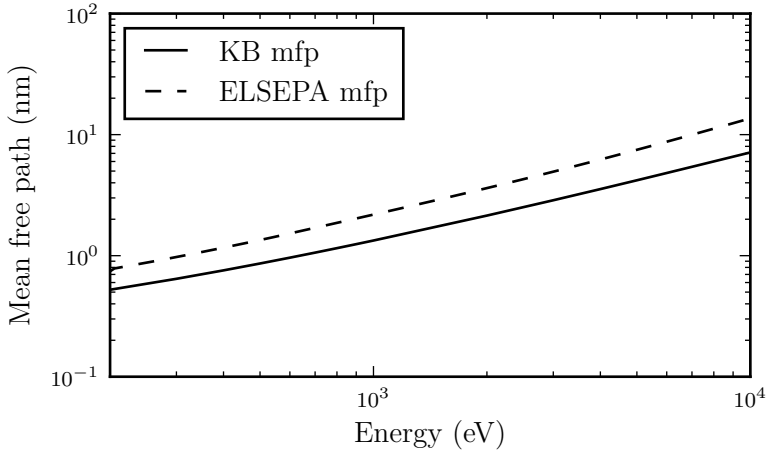
Figure 2.1: The mean free path for silicon calculated with the Mott cross sections used by Kieft and Bosch compared to the mean free path calculated with the ELSEPA Mott cross sections, taking solid state effects into account.

old mean free path as can be seen in the Figure. At very low energies, the calculated values for the Mott cross sections become very dependent on the exact atomic potential $V(r)$ used in de calculation. For a more detailed comparison of different choices for the atomic potential $V(r)$ and the effect on the mean free path, see [10]. This is why for lower energies, different models are necessary to calculate the mean free path. These models will be discussed in 2.1.1.1. For now it suffices to know that for insulators and semiconductors (like silicon), the mean free path is interpolated between the low energy model at 100 eV and the mean free path calculated with the Mott cross sections at 200 eV. For metals, the low energy model of Kieft and Bosch goes only up to the Fermi energy. In between the Fermi energy and 100 eV, the mean free path is interpolated between the low energy model at the Fermi energy and the mean free path calculated with the Mott cross sections at 25, 50, 75 and 100 eV. The new mean free path in this case is also interpolated, however, more data points for the Mott cross sections are used. The resulting mean free paths for gold are shown in Figure 2.2.
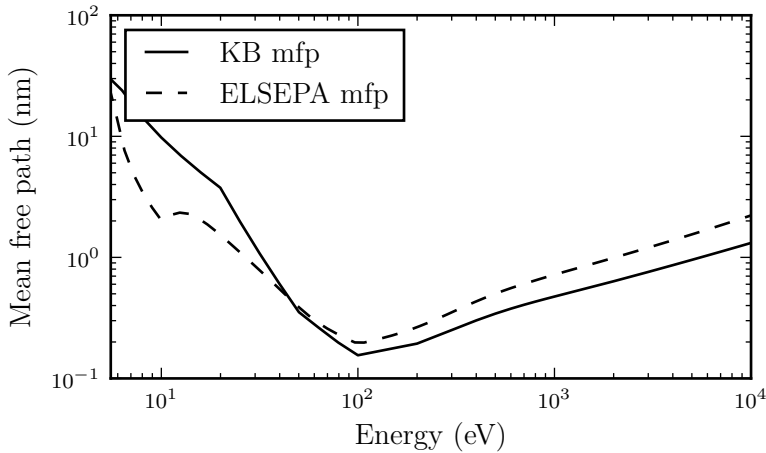
Figure 2.2: The mean free path for gold calculated with the Mott cross sections used by Kieft and Bosch compared to the mean free path calculated with the ELSEPA Mott cross sections, taking solid state effects into account. Between the Fermi energy of 5.53 eV and 100 eV the mean free path is interpolated between the Mott cross sections and the low energy model.

Previously we mentioned an electron loses a small amount of energy during an elastic scattering event. We have ignored this up to now because this energy loss is small and it would be unnoticeable in most applications. However, it would be noticeable as a small energy loss in the backscatter electron peak. So even though the energy loss is small, we still take it into account. The energy loss is the atomic recoil energy loss and is calculated as [1]

$$E_{recoil} = \frac{2m_e}{M} \left(1 - \cos\theta\right) E,\tag{2.14}$$

with initial electron energy E, electron mass m_e, atomic mass M and scattering angle θ.

2.1.1.1 Low energy elastic scattering

At very low energies, Kieft and Bosch used two different models: one model for insulators and semiconductors and one for metals. We will start with discussing the model for insulators and semiconductors: acoustic phonon scattering. At these low energies, electrons will behave more like Bloch waves instead of point particles. These Bloch waves will no longer scatter on a single atom in the solid, but rather on a collective movement of the atoms in the solid [15]. Such a collective movement is a phonon. There are two different phonon modes possible in a lattice, the optical mode and the acoustic mode. Longitudinal optical phonons are taken into account in the inelastic processes simulated, this will be discussed in 2.1.2. However, acoustic phonons can be used to calculate the elastic mean free path for low energy electrons. Kieft and Bosch use the model for acoustic phonons described by Schreiber and Fitting [15, 16]. The model of Schreiber and Fitting is based on the expression of Sparks et al. [17] extended with a Coulomb screening parameter from Bradford and Woolf [18]. The basic picture here is that a low energy electron can create or absorb an acoustic phonon. In this process, the electron will have a small energy change, due to the energy of the phonon and a big change in momentum. The energy change is so small that the interaction can still be considered elastic. Hence the most important effect of the electron absorbing/creating an acoustic phonon is the

momentum change. At low energies, the inelastic mean free path increases significantly, as will be explained in 2.1.2. At these low energies, elastic scattering becomes the more dominant process. Hence to prevent electrons being trapped in the low energy regime without losing any energy, the energy change of an electron during a scattering event with an acoustic phonon needs to be taken into account. Here we used the average energy loss for an electron during a scattering event with an acoustic phonon. In a private mail communication Kieft explained how the average energy loss used to be calculated: The typical energy we are interested in is the maximum phonon energy, which is equal to the acoustic phonon energy at the Brillouin zone boundary

$$E_{ac} = \hbar\omega_{ac},$$ (2.15)

with $\omega = c_s/a$, where a is the lattice constant, and c_s the sound velocity. In general an approximate dispersion relation is used

$$E_{ac}(k) = \hbar\omega_{ac}(k) = 2\hbar\omega\sin\left(\frac{ka}{2}\right),$$ (2.16)

such that the following relation is satisfied

$$\lim_{k\to 0}\frac{\mathrm{d}\omega_{ac}(k)}{\mathrm{d}k} = \lim_{k\to 0}\frac{\mathrm{d}}{\mathrm{d}k}2\omega\sin\left(\frac{ka}{2}\right) = c_s.$$ (2.17)

If we then assume that the Brillouin zone is spherical with radius $k_{BZ} = \pi/a$, and we assume the dispersion relation only has a radial dependence. Then we can calculate the average phonon energy loss at zero temperature as

$$\langle E_{ac}\rangle = 2\hbar\omega\frac{\int_0^{\pi/a}\sin\left(ka/2\right)k^2\mathrm{d}k}{\int_0^{\pi/a}k^2\mathrm{d}k}.$$ (2.18)

At finite temperatures, there will already be a phonon population present and phonon absorption is also a possibility. The phonon population at temperature T is

$$N(k,T) = \frac{1}{\exp\left(\frac{\hbar\omega_{ac}(k)}{k_B T}\right) - 1}.$$ (2.19)

Kieft then makes the approximation

$$N(k,T) \approx \frac{k_B T}{\hbar \omega_{ac}(k)} = \frac{k_B T}{2\hbar \omega \sin(ka/2)}, \qquad (2.20)$$

so that the weighted-average phonon energy becomes

$$\langle E_{ac} \rangle = 2\hbar\omega \frac{\int_0^{\pi/a} \sin(ka/2) \, k^2 \left[\sin(ka/2)\right]^{-1} \mathrm{d}k}{\int_0^{\pi/a} k^2 \left[\sin(ka/2)\right]^{-1} \mathrm{d}k}. \qquad (2.21)$$

Kieft proceeds to explain that in their Monte Carlo code he then used the assumption that during every phonon scattering event, the electron both absorbs one phonon energy according to the phonon population distribution (i.e. the energy as calculated in Equation 2.21) as well as emits one phonon energy according to a flat distribution (i.e. the energy as calculated in Equation 2.18). This is used in the original Monte Carlo code of Kieft and Bosch. However, in the same mail correspondence, Kieft points out that a better model would be to use detailed balancing in every phonon scattering event. In other words, during every phonon scattering event either one phonon is absorbed or one phonon is emitted, the absorption is proportional to $N(k,T)$ and the emission is proportional to $N(k,T) + 1$. Using the same dispersion relation as stated in equation 2.16, this results in

$$\langle E_{ac} \rangle = \frac{4\pi \int_0^{k_{BZ}} \left[N(k,T) + 1 - N(k,T)\right] \hbar\omega_{ac}(k) k^2 \mathrm{d}k}{4\pi \int_0^{k_{BZ}} \left[2N(k,T) + 1\right] k^2 \mathrm{d}k}, \qquad (2.22)$$

where k_{BZ} is k at the Brillouin zone boundary.

In our code we used the detailed balancing method Kieft proposed. However, we also used a different dispersion relation. In fact, we used the dispersion relation as proposed by Verduin [10]

$$\omega_{ac}(k) = c_s k - \alpha k^2, \qquad (2.23)$$

here α relates to the bending of the dispersion relation towards the boundary

of the Brillouin zone. With this dispersion relation, we still have

$$\lim_{k \to 0} \frac{\mathrm{d}\omega_{ac}}{\mathrm{d}k} = c_s. \tag{2.24}$$

The phonon energy at the Brillouin zone boundary is then simply $\hbar\omega_{ac}(k_{BZ})$. Now we can calculate the average energy loss for an electron during a phonon scattering event using equation 2.22, where we did not use the Taylor expansion for the phonon population. We used the exact expression for the phonon population as given in equation 2.19.

In order to calculate the mean free path of the electrons for acoustic phonon scattering, Kieft and Bosch used the models described by Schreiber and Fitting [15, 16]. They give the acoustic phonon scattering rate as

$$P_{ac}(E) = \begin{cases} \dfrac{\pi \epsilon_{ac}^2 k_B T}{\hbar c_s^2 \rho_m} \dfrac{A}{A+E} D(E), & \text{if } E < \dfrac{E_{BZ}}{4} \\[3mm] \dfrac{4\pi \left(2N_{BZ}+1\right) m_D \epsilon_{ac}^2}{\hbar\omega_{BZ}\hbar\rho_m} \dfrac{A^2}{E} \left[\ln \dfrac{A+E}{A} - \dfrac{E}{A+E}\right], & \text{if } E > E_{BZ}, \end{cases} \tag{2.25}$$

where ϵ_{ac} is the acoustic deformation potential, ρ_m the mass density, $\omega_{BZ} = \omega_{ac}(k_{BZ})$, m_D the density of states electron mass, A is a screening factor of $A = 5E_{BZ}$ and N_{BZ} is the acoustic phonon population at the Brillouin zone boundary ($k = k_{BZ}$). The Brillouin zone energy is given by

$$E_{BZ} = \frac{(\hbar k_{BZ})^2}{2m_e}, \tag{2.26}$$

and the density of states is

$$D(E) = \frac{\sqrt{2m_D^3 \left(E - E_{CB}\right)}}{\pi^2 \hbar^3}, \tag{2.27}$$

where E_{CB} is the energy at the conduction band minimum. The inverse mean free path can be calculated from the scattering rate using the electron velocity $v_e(E)$

$$\frac{1}{\lambda_{ac}(E)} = \frac{P_{ac}(E)}{v_e(E)} = \frac{m_e^* P_{ac}(E)}{\sqrt{2m_e^*(E - E_{CB})}}, \tag{2.28}$$

where m_e^* is the effective electron mass. Combining equations 2.25, 2.27 and 2.28 gives

$$
\frac{1}{\lambda_{ac}(E)} =
$$

$$
=
\begin{cases}
\lambda_0^{-1} \dfrac{A}{A+E}, & \text{if } E < \dfrac{E_{BZ}}{4} \\[3mm]
\lambda_0^{-1} \left(N_{BZ} + \dfrac{1}{2} \right) \dfrac{8 m_D c_s^2}{\hbar \omega_{BZ} k_B T} \dfrac{A^2}{E} \left[\ln \dfrac{A+E}{A} - \dfrac{E}{A+E} \right], & \text{if } E > E_{BZ},
\end{cases}
\tag{2.29}
$$

with

$$
\lambda_0^{-1} = \frac{\sqrt{m_e^* m_D^3} \epsilon_{ac}^2 k_B T}{\pi \hbar^4 c_s^2 \rho_m}.
\tag{2.30}
$$

In the region $E_{BZ}/4 < E < E_{BZ}$ the inverse mean free path is interpolated between the two values given by the 'low' and 'high' energy part in equation 2.29. The angular differential inverse mean free path is then given by

$$
\frac{\mathrm{d}}{\mathrm{d}\Omega} \frac{1}{\lambda_{ac}(E,\theta)} =
$$

$$
=
\begin{cases}
\dfrac{\lambda_0^{-1}}{4\pi} \dfrac{1}{\left(1 + \frac{1-\cos\theta}{2} \frac{E}{A}\right)^2}, & \text{if } E < \dfrac{E_{BZ}}{4} \\[3mm]
\dfrac{\lambda_0^{-1}}{4\pi} \left(N_{BZ} + \dfrac{1}{2} \right) \dfrac{8 m_D c_s^2 A}{\hbar \omega_{BZ} k_B T} \dfrac{\frac{1-\cos\theta}{2} \frac{E}{A}}{\left(1 + \frac{1-\cos\theta}{2} \frac{E}{A}\right)^2}, & \text{if } E > E_{BZ}.
\end{cases}
\tag{2.31}
$$

In the Monte Carlo code of the simulator developed by Kieft and Bosch, equation 2.29 and 2.31 both have an overall extra factor of π. We think this overall factor of π might be the result of fitting the calculated inverse mean free path to the values given by Fitting et al. [16]. We think the overall factor of π has to do with the fact that Kieft and Bosch only took longitudinal acoustic phonon scattering into account. When transversal acoustic phonon scattering is taken into account, a first rough estimation would be to just multiply the longitudinal acoustic phonon cross section by a factor 3. We used the equations as stated in 2.29 and 2.31 and calculated the longitudinal λ_{ac_L} and transversal acoustic phonon mean free path λ_{ac_T} using the longit-

udinal and transversal sound velocity and acoustic deformation potentials. The total acoustic phonon mean free path then becomes

$$\frac{1}{\lambda_{ac_{tot}}(E,\theta)} = \frac{1}{\lambda_{ac_L}(E,\theta)} + \frac{2}{\lambda_{ac_T}(E,\theta)}.$$
(2.32)

A second approximation Kieft and Bosch made in the calculation of the acoustic phonon scattering mean free path is that again an approximation to the phonon population is used, which is the Taylor expansion of the exact equation. We used the exact equation to calculate the phonon population. Lastly, in the 'high' energy ($E > E_{BZ}$) part of equations 2.29 and 2.31 a factor of π is missing in the Monte Carlo code of Kieft and Bosch. This error 'corrects' the previously mentioned erroneous overall factor of π for the 'high' energy part. However, since we have removed the overall factor of π, now a factor of π is missing. We have corrected this error in our calculation.

The mean free path of silicon calculated using the above mentioned model refinements of using the Mott cross sections from ELSEPA, taking solid state effects into account, and using the dual branch phonon model where the longitudinal as well as the two transversal acoustic phonon branches are taken into account, is shown in Figure 2.3. For reference, the original elastic mean free path as calculated by Kieft and Bosch is also shown in Figure 2.3. The material parameters used in the calculations of the elastic mean free paths are detailed in appendix A. In the Figure, five regions are denoted. Region A is the region where $E < E_{BZ}/4$, in this region, the 'low' energy phonon model is valid. Region B is the region where $E_{BZ} < E < 100$ eV, the 'high' energy phonon model is used here. In between region A and B, we have region I. Here the mean free path is interpolated between the 'low' and 'high' energy mean free paths. This interpolation is a linear interpolation of the inverse mean free paths in the original Kieft and Bosch models. In our new models, we decided to use a different interpolation method in order to obtain a more smooth transition. We used a logarithmic interpolation of the cross sections with the weight function [19]

$$w(E) = (3 - 2E) \cdot E^2.$$
(2.33)

The fourth region we have, is region C where $E > 200$ eV, here the Mott cross sections are used to calculate the elastic mean free path. In region II, in between 100 eV and 200 eV, again a linear interpolation of the inverse mean free paths is used in the original Kieft and Bosch models. In our models, a logarithmic interpolation of the cross sections (without the weight function) is used. Kieft and Bosch decided to set the bounds of interpolation region II to 100 eV and 200 eV. Below 100 eV, the Mott cross sections calculated become very dependent on the exact atomic potential used in the calculation. This is why Kieft and Bosch decided to use the acoustic phonon models below 100 eV. We speculate they used the interpolation region between 100 eV and 200 eV to get a transition region between the two models instead of just jumping from one model to the next. At last we would like to point out that the transition between the 'high' energy phonon models and the Mott cross section is very smooth when we use our new models. However, this is most likely the effect of the material parameters used. A small change in, for example, the acoustic deformation potential would lead to a less smooth transition. Since the acoustic deformation potential is a very difficult parameter to obtain, the fact that we have a smooth transition in region II is more likely to be a coincidence than to be the result of our new models. In fact, for the other materials we will discuss, this transition is not as smooth as it is for silicon, as can be seen in the next paragraphs.

In the case of metals, Kieft and Bosch used a different model. In metals, the scattering rate τ_m^{-1} of electrons at the Fermi energy is directly dependent on the mobility μ or the resistivity ρ_R

$$\mu = \frac{-1}{\rho_R n e} = \frac{-e}{m_e \tau_m^{-1}(E_F)}, \tag{2.34}$$

where n is the density of free electrons. This gives the scattering rate

$$\tau_m^{-1}(E_F) = \frac{\rho_R n e^2}{m_e}. \tag{2.35}$$
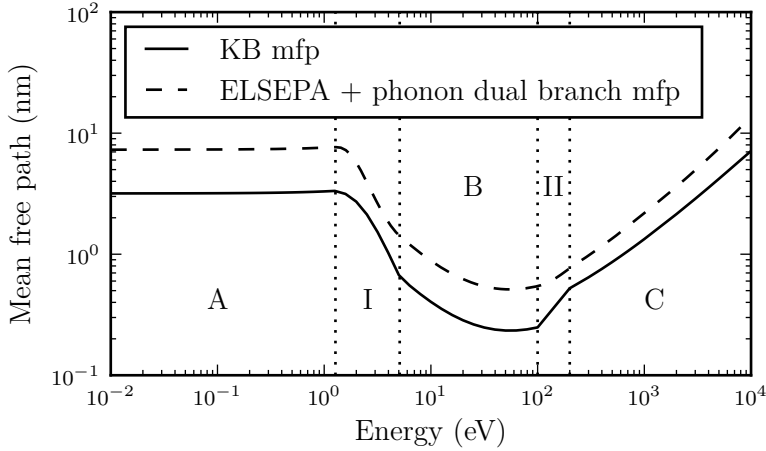
Figure 2.3: The mean free path for silicon calculated using the cross sections from ELSEPA and the dual branch phonon model (dashed line) compared to the mean free path calculated and used by Kieft and Bosch (solid line). In region A ($E < E_{BZ}/4$), the 'low' energy phonon model is used, in region B ($E_{BZ} < E < 100$ eV) the 'high' energy phonon model is used, and in region C ($E > 200$ eV) the Mott cross sections are used to calculate the elastic mean free path. In region I the mean free path is interpolated between the 'low' and 'high' energy phonon models, and in region II the mean free path is interpolated between the 'high' energy phonon model and the Mott cross section model.

The inverse mean free path is then given by

$$\frac{1}{\lambda_{metal}(E_F)} = \frac{\tau_m^{-1}(E_F)}{v_{Fermi}} = \frac{\rho_R n e^2}{m_e v_{Fermi}}, \tag{2.36}$$

with v_{Fermi} the electron velocity at the Fermi energy. The density of free electrons can be calculated from the density of states, assuming a parabolic band structure and an effective electron mass equal to the free electron mass

$$n = \int_0^{E_F} D(E)\mathrm{d}E = \frac{2\sqrt{2}}{3\pi^2\hbar^3} (m_e E_F)^{\frac{3}{2}}. \tag{2.37}$$

Which gives at last

$$\frac{1}{\lambda_{metal}(E_F)} = \frac{2m_e e^2}{3\pi^2 \hbar^3} \rho_R E_F. \tag{2.38}$$

This does not give any angular distribution. Kieft and Bosch used the same angular distribution as for the 'low' energy part of the acoustic phonon inverse mean free path as given in equation 2.31. Above 100 eV the Mott cross sections are used for metals and in between the Fermi energy and 100 eV, the inverse mean free path is obtained by linearly interpolating the value at the Fermi energy from equation 2.38 and the Mott cross section at 100 eV.

We did not use this method in our simulator. As Verduin pointed out [10], the calculated value of the inverse mean free path in equation 2.38 is equal to the acoustic phonon inverse mean free path at zero energy if we assume equation 2.38 is independent of energy below the Fermi energy.

$$\frac{1}{\lambda_{metal}(E_F)} = \frac{1}{\lambda_{ac}(E=0)} = \lambda_0^{-1}. \tag{2.39}$$

Now we can calculate the acoustic deformation potential for a metal [10]

$$\epsilon_{ac}^2 = \frac{2\hbar e^2 c_s^2}{3\pi m_e k_B T} \rho_R \rho_m E_F. \tag{2.40}$$

We used this as input in the calculation of the acoustic phonon inverse mean free path for metals, so we can use acoustic phonon scattering for metals as well as for insulators and semiconductors.

The effects of using the Mott cross sections from ELSEPA and using the dual branch phonon model on the elastic mean free path of gold are shown in Figure 2.4. Again, the material parameters used in the calculations of the elastic mean free paths are detailed in appendix A. The first model improvement is the use of the Mott cross sections calculated with ELSEPA. This affects the elastic mean free path down to the Fermi energy of 9.11 eV (as used by Kieft and Bosch), since they used the Mott cross sections down to the Fermi energy. When we include the second model improvement and use the dual branch phonon model, the result is a smaller elastic mean free path below 20 eV compared to the elastic mean free path calculated by Kieft
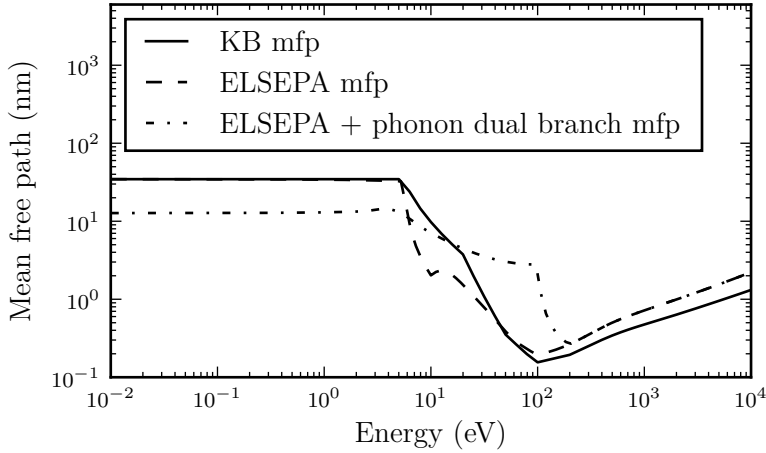
Figure 2.4: The elastic mean free path for gold calculated using only the cross sections from ELSEPA and the acoustic phonon scattering model of Kieft and Bosch (dashed line), the mean free path calculated using the ELSEPA cross sections and the dual branch phonon model (dash-dotted line), both compared to the mean free path calculated and used by Kieft and Bosch (solid line).

and Bosch. Note however that we used different values for the Fermi energy and the resistivity than Kieft and Bosch did, so we do expect to obtain a different value for the elastic mean free path below and at the Fermi energy.

For alumina, we were not able to find the branch dependent acoustic deformation potentials. For materials where the branch dependent parameters are not known, we cannot use equation 2.32. However, if we are able to find one value for the acoustic deformation potential and the sound velocity, we can use an approximation to calculate the elastic mean free path due to acoustic phonon scattering

$$\frac{1}{\lambda_{ac_{tot}}(E, \theta)} \approx \frac{3}{\lambda_{ac}(E, \theta)}, \tag{2.41}$$

where $\lambda_{ac}(E, \theta)$ is the mean free path as calculated with equation 2.31. This will not give the exact elastic mean free path, since the cross section for the transversal acoustic phonon modes is not the same as the cross section for

the longitudinal acoustic phonon mode. In order to use the approximation
for silicon, we needed the 'effective' sound velocity and acoustic deformation
potential. We calculated these by taking the weighted average between the
longitudinal and transversal values

$$c_{s_{eff}} = \frac{c_{s_L} + 2c_{s_T}}{3},$$
$$\epsilon_{ac_{eff}} = \frac{\epsilon_{ac_L} + 2\epsilon_{ac_T}}{3}.$$

(2.42)

The difference between the elastic mean free path of silicon calculated with
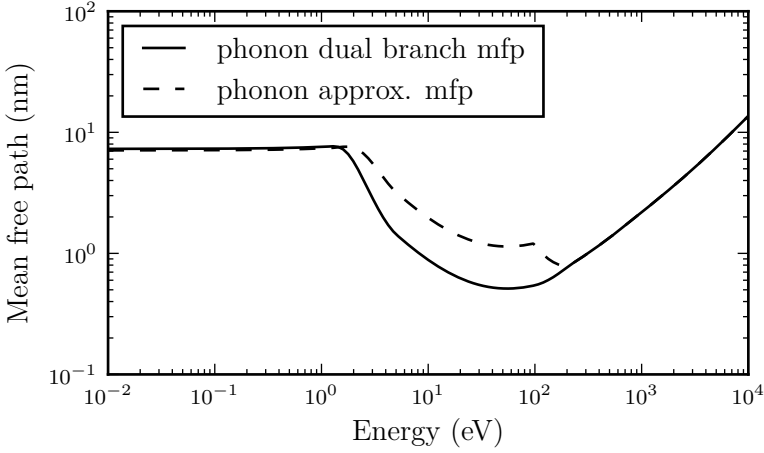
Figure 2.5: The elastic mean free path for silicon as calculated with the
approximation to the dual branch phonon model compared to the mean free
path calculated with the dual branch phonon model.

the dual branch acoustic phonon model and this approximation is shown in
Figure 2.5. We see a clear difference between the mean free paths in the
'high' energy regime of the phonon model. In the 'low' energy regime we
do not see a difference, however, this is not necessarily the case for different
materials. For silicon, the sound velocity and acoustic deformation potential
are just such that the approximation in the 'low' energy regimes gives almost
the same mean free path as the exact calculation. Since we were not able
to find branch dependent values of the acoustic deformation potential and

the sound velocity, we used the values we could find as effective values and we used the approximate model to calculate the elastic mean free path for alumina. The new elastic mean free path for alumina with the ELSEPA cross
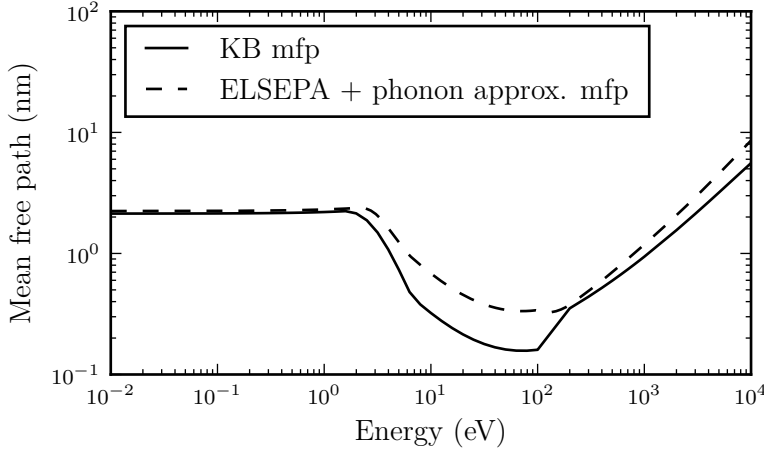
Figure 2.6: The elastic mean free path for alumina calculated using the cross section from ELSEPA and the approximation to the dual branch phonon model, compared to the mean free path as calculated by Kieft and Bosch.

sections, and the approximation to the phonon dual branch model we used, are shown in Figure 2.6.

2.1.2 Inelastic scattering

During an inelastic scattering event, an electron loses some of its energy to an electron in the material, creating a secondary electron in the process. The direction of the electron will also change in this scattering event. There are different kinds of inelastic processes that the electron can lose energy to, such as creating a longitudinal optical phonon, exciting a bulk plasmon, or exciting an inner shell electron around one of the atoms in the material. These processes could all be accounted for in separate models, however, it is also possible to use dielectric function theory, where all these processes are included. Kieft and Bosch have made model refinements to the model by Ashley [20], based on the dielectric function theory. Ashley's model relates

to the single-pole approximation of the Penn model [21], which is based
on the Lindhard dielectric function ϵ_L. When an electron travels through a
(dielectric) material, it will disrupt the equilibrium charge distribution of the
material. As a result, the charge distribution of the material will change. The
Lindhard dielectric function relates the dielectric response of the material to
the electron to the energy loss processes the electron can undergo. In the
dielectric function theory, the inverse inelastic mean free path of an electron
is

$$\frac{1}{\lambda_i(E)} = \frac{1}{\pi E} \int \int_{-q}^{+q} \frac{dq}{q} \text{Im} \left[\frac{-1}{\epsilon(q, \omega)} \right] d\omega, \tag{2.43}$$

where ω is the total energy loss for the primary electron and q the momentum
transfer between the primary and secondary electron. The expanded dielec-
tric function $\epsilon(q, \omega)$ can be calculated from optical data $\epsilon(0, \omega)$

$$\text{Im} \left[\frac{-1}{\epsilon(q, \omega)} \right] = \frac{\omega'}{\omega} \text{Im} \left[\frac{-1}{\epsilon(0, \omega')} \right], \tag{2.44}$$

where we define the zero-momentum energy transfer ω' as

$$\omega' = \omega - \frac{q^2}{2}. \tag{2.45}$$

We can use this relation to change variables in equation 2.43

$$\frac{1}{\lambda_i(E)} = \frac{1}{2\pi E} \int \int_0^\infty \omega' \text{Im} \left[\frac{-1}{\epsilon(0, \omega')} \right] F(E, \omega', \omega) d\omega' d\omega, \tag{2.46}$$

where $F(E, \omega', \omega)$ is defined as

$$F(E, \omega', \omega) = \begin{cases} \dfrac{1}{\omega(\omega - \omega')}, & \text{for } \omega' + \dfrac{q_-^2}{2} < \omega < \omega' + \dfrac{q_+^2}{2} \\ 0, & \text{otherwise.} \end{cases} \tag{2.47}$$

Where $q_\pm \equiv \sqrt{2} \left(\sqrt{E} \pm \sqrt{E - \omega} \right)$. Now we can simplify to

$$\frac{1}{\lambda_i(E)} = \frac{1}{2\pi E} \int_0^{E/2} \text{Im} \left[\frac{-1}{\epsilon(0, \omega')} \right] L(\omega', E) d\omega', \tag{2.48}$$

where $L(\omega', E)$ is defined as

$$L(\omega', E) = \int_{\omega_-}^{\omega_+} \omega' F(E, \omega', \omega)\mathrm{d}\omega. \qquad (2.49)$$

Where the integration limits ω_- and ω_+ are defined as

$$\omega_- = \frac{1}{2}\left(E + \omega' - E\sqrt{1 - \frac{2\omega'}{E}}\right), \qquad (2.50\mathrm{a})$$

$$\omega_+ = \frac{1}{2}\left(E + \omega'\right). \qquad (2.50\mathrm{b})$$

Kieft and Bosch now made model refinements to the above explained model. First they start with making a distinction between interactions with inner shell electrons on the one hand and interactions with outer shell electrons and plasmons on the other hand. They set the limit between the two cases at $\omega' = 50\mathrm{eV}$, reasoning that this energy is above the bulk plasmon peak for most materials, and below the energy thresholds of relevant inner shell ionisation processes. In the case where $\omega' > 50\mathrm{eV}$ the model refinements of Kieft and Bosch did not use momentum conservation. They reason that momentum conservation between the interacting electrons does not apply to inner shell ionisations generally. Experimental results show that it is possible to ionise inner shell electrons when their binding energy is more than half the kinetic energy of the primary electron, the data in [22] supports this for example. This is why Kieft and Bosch used a phenomenological description for L in the case of $\omega' > 50\mathrm{eV}$

$$L = -\ln\left(\frac{\omega'}{E}\right). \qquad (2.51)$$

Note that in this case, the upper integration limit in equation 2.48 is E instead of $E/2$. The upper limit $E/2$ follows from momentum conservation, which is ignored in this case.

In the case where $\omega' < 50\mathrm{eV}$ Kieft and Bosch introduced several model refinements. We will list them here shortly.

1. Most interactions where $\omega' < 50\text{eV}$ are interactions where the primary electron excites a plasmon in the material. This plasmon will decay and create a secondary electron. In this case, it is possible to distinguish between the primary electron and the secondary electron, so the exchange correction proposed by Ashley [20] is not used. This means that the $F(E, \omega', \omega)$ function as defined in equation 2.47 is used.

2. Kieft and Bosch point out that the energy loss can never be so high that the primary electron ends up below the Fermi energy E_{Fermi}. This is why they redefine ω_+ to be $\omega_+ = \frac{1}{2}(E - E_{Fermi} + \omega')$.

3. Kieft and Bosch compared the calculated inverse mean free path, taking the two previous points into account, to other experimental and theoretical sources, such as [22, 23]. They found that the calculated values underestimated the inverse mean free path. As a solution they introduced an extra factor of 1.5 for the $L(\omega', E, E_{Fermi})$ function.

The above refinements result in a new definition of the $L(\omega', E, E_{Fermi})$ function, which now explicitly depends on ω' and E_{Fermi}

$$
\begin{aligned}
L(\omega', E, E_{Fermi}) &= 1.5 \int_{\omega_-}^{\omega_+} \omega' F(E, \omega', \omega)\, \mathrm{d}\omega = \left[\ln \frac{\omega - \omega'}{\omega}\right]_{\omega=\omega_-}^{\omega_+} \\
&= 1.5 \left[\ln\left(\frac{2}{a}(1 + \sqrt{1 - 2a}) - 1\right) + \ln\left(\frac{E - E_{Fermi} - \omega'}{E - E_{Fermi} + \omega'}\right)\right],
\end{aligned}
\tag{2.52}
$$

where $a = \omega'/E < 1/2$. When $a > 1/2$, $L(\omega', E, E_{Fermi})$ is defined to be zero.

We went back to the original paper of Ashley, to investigate the effect of these model refinements. We agree with Kieft and Bosch that in the case of plasmon excitations, the exchange correction is not necessary. However, we do not completely agree with the implementation. We disagree with the values used for ω_+. Ashley indeed states the equations for ω_- and ω_+ as defined in equation 2.50. To define the allowed region of integration, Ashley gives a Figure similar to Figure 2.7. Although it is not stated explicitly in the paper, this integration region is correct for the exchange corrected

model. From Figure 2.7 we can indeed derive ω_- and ω_+ as given in equation

Figure 2.7: The grey shaded region is the allowed region of integration for equation 2.49 in the case of the exchange corrected Ashley model.

2.50 for the exchange corrected model. Ashley does not directly give the integration bounds for the non-exchange corrected model, so we understand the confusion. However, Ashley does give the $L(a)$ function for the non-exchange corrected model as

$$L(a) = \ln\left[\frac{1 - a/2 + \sqrt{1 - 2a}}{1 - a/2 - \sqrt{1 - 2a}}\right]. \qquad (2.53)$$

In order to arrive at this result, we found the allowed integration region in the non-exchange corrected model is not given by Figure 2.7, but rather by Figure 2.8. The bounds for the integration over ω in equation 2.49 for the non-exchange corrected model are

$$\omega_- = \frac{1}{2}\left(E + \omega' - E\sqrt{1 - \frac{2\omega'}{E}}\right), \qquad (2.54a)$$

$$\omega_+ = \frac{1}{2}\left(E + \omega' + E\sqrt{1 - \frac{2\omega'}{E}}\right). \qquad (2.54b)$$

We found that using these integration bounds for equation 2.49 makes it unnecessary to include the factor 1.5 as discussed in refinement 3.

Figure 2.8: The grey shaded region is the allowed region of integration for equation 2.49 in the case of the non-exchange corrected Ashley model.

We would also like to point out that refinement 2 does not give the desired effect. This refinement shifts the integration bound ω_+ down with half the Fermi energy. This is illustrated in Figure 2.9. This Fermi correction looks very complicated and it does not prevent a primary electron from ending up below the Fermi energy, only a check if $E - \omega > E_{Fermi}$ does this. Note that we did find this check in the Monte Carlo code of Kieft and Bosch. However, we propose a much simpler Fermi correction. We propose to define ω_+ as

$$\omega_+ = \min\left(\frac{1}{2}\left(E + \omega' + E\sqrt{1 - \frac{2\omega'}{E}}\right), E - E_{Fermi}\right). \qquad (2.55)$$

The effect of this on the allowed integration region in equation 2.49 is illustrated in Figure 2.10. The new inelastic mean free path for silicon is shown in Figure 2.11, the mean free path as calculated by Kieft and Bosch is shown for comparison. The effect of our model refinements is not very big, however, we do no longer need the phenomenological factor of 1.5 from refinement 3
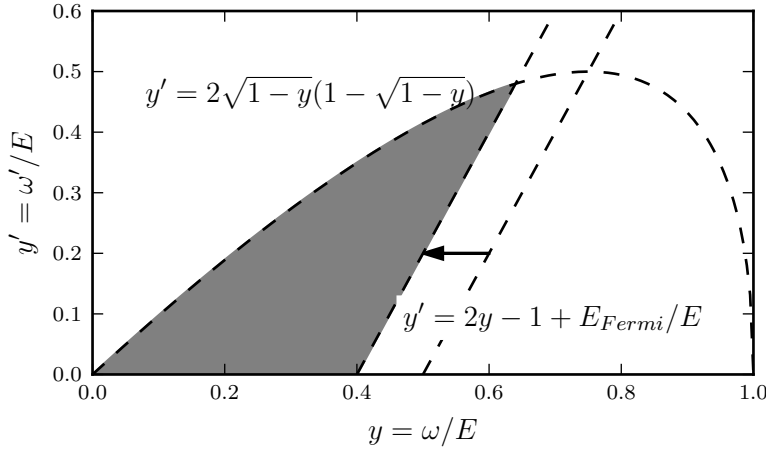
Figure 2.9: The grey shaded region is the allowed region of integration for equation 2.49 for the model used by Kieft and Bosch, including the Fermi correction from refinement 2. In this example, the Fermi energy is $E_{Fermi} = 0.2E$.

of Kieft and Bosch. We are also using a simpler Fermi correction, which has the desired effect of preventing the primary electron from ending up below the Fermi energy. For gold and alumina, the effect on the mean free path is in the same order as for silicon. For completeness, the inelastic mean free paths for gold and alumina are shown in Figure 2.12.

Now all we need to determine the inelastic mean free path for a new material is the dielectric function $\epsilon(0, \omega) = \epsilon_r(\omega) + i\epsilon_i(\omega)$ of the material. The dielectric function of a material can be calculated from optical data by

$$\epsilon_r(0, \omega) = n(\omega)^2 - \kappa(\omega)^2, \tag{2.56a}$$

$$\epsilon_i(0, \omega) = 2n(\omega)\kappa(\omega), \tag{2.56b}$$

where $n(\omega)$ is the energy dependent index of refraction and $\kappa(\omega)$ the energy dependent absorption coefficient. In the models, the energy loss function is
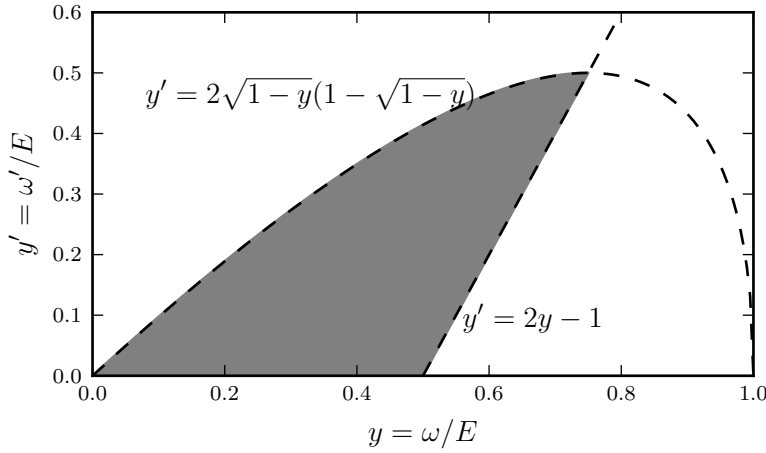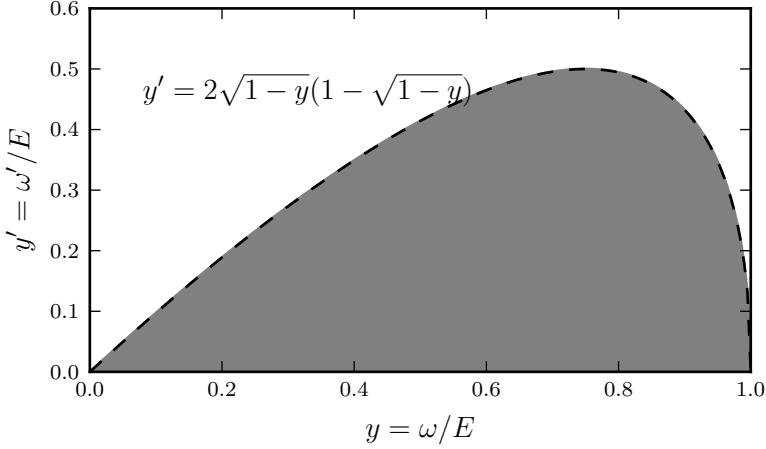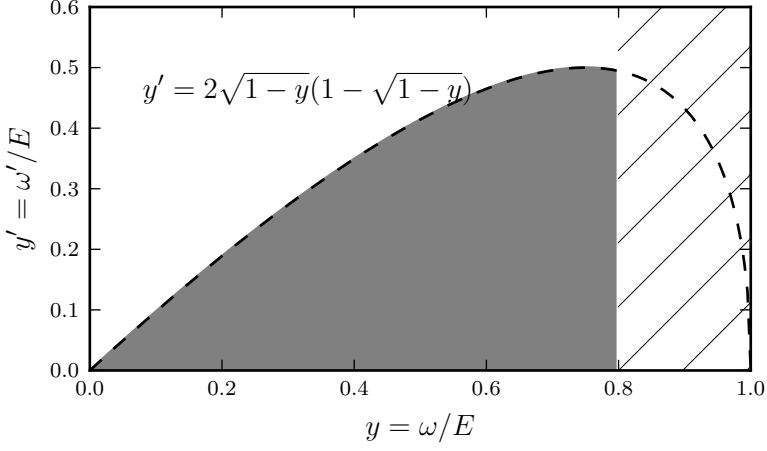
Figure 2.10: The grey shaded region is the allowed region of integration for equation 2.49 for the non-exchange corrected Ashley model including our proposed Fermi correction. The striped region is the region we propose to exclude with our Fermi correction. In this example, the Fermi energy is $E_{Fermi} = 0.2E$.
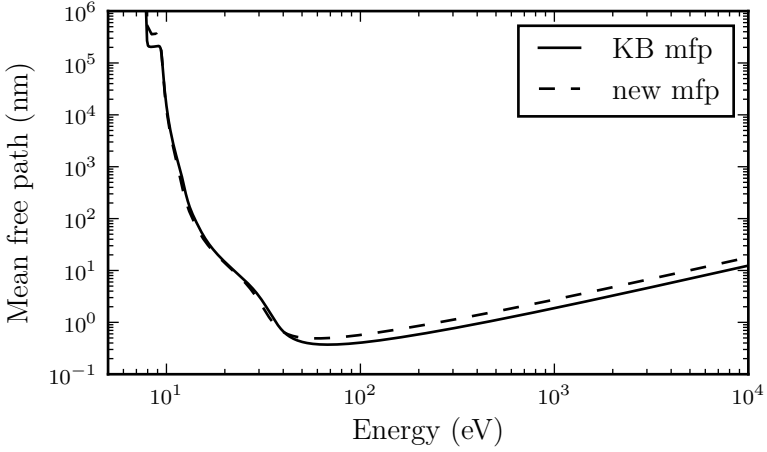
Figure 2.11: The inelastic mean free path for silicon as calculated by Kieft and Bosch compared to the mean free path calculated with our models.
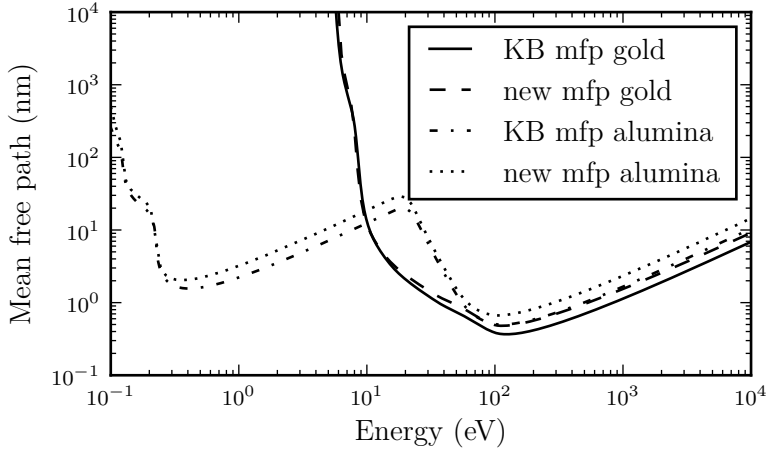
Figure 2.12: The inelastic mean free path for gold and alumina as calculated by Kieft and Bosch compared to the mean free path calculated with our models.

used, where the energy loss function $ELF(\omega)$ is defined as

$$ELF(\omega) = \mathrm{Im}\left[\frac{-1}{\epsilon(0, \omega)}\right]. \tag{2.57}$$

Kieft and Bosch have compiled a whole database of energy loss functions for different materials. The energy loss function for silicon is shown in Figure 2.13. In this energy loss function, we can distinguish four regions. Starting at around 100 eV energy loss, we indeed see the inner shell excitations for silicon as jumps in the energy loss function. Around 16 eV we see the bulk plasmon loss peak. The energy distinction of 50 eV Kieft and Bosch use to distinguish between the inner shell excitations and the plasmon and outer shell excitations is indeed correct for silicon. Below the bulk plasmon loss peak, the energy loss function has a minimum, which is due to the band gap of silicon, a primary electron cannot excite a secondary electron by losing an energy smaller than the band gap. This would result in the secondary electron being inside the band gap, which of course is not possible. However, we do distinguish a fourth region in the energy loss function: very small
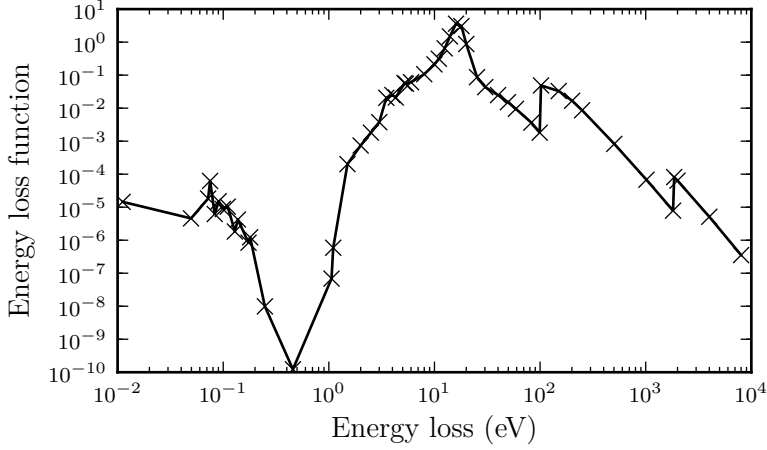
Figure 2.13: The energy loss function for silicon.

energy losses are still possible. In this case, the primary electron does not lose energy to a secondary electron, but to a longitudinal optical phonon [16,24].

Now we know how to determine the inelastic mean free path, but when an electron scatters inelastically, we still need to determine the energy loss of this electron and the scattering angle, and we need to create a secondary electron. For the creation of the secondary electron, we need to determine its binding energy and the momentum direction. The scattering angle of the primary electron and the secondary electron are of course related due to momentum conservation. As Verduin [10] discusses, in order to sample the energy loss of the primary electron, first the zero-momentum energy loss ω' is sampled using the cumulative probability derived from equation 2.48

$$p\left(E, \omega'\right) = \frac{\lambda_i(E)}{2\pi E} \int_0^{\omega'} d\omega' \text{Im}\left[\frac{-1}{\epsilon(0, \omega')} L(E, \omega')\right]. \qquad (2.58)$$

ω' is then sampled by setting equation 2.58 equal to a random number U from a uniform distribution between 0 and 1 and solving for ω'. Now we still need to sample the energy loss ω. For this we go back to equation 2.46, noticing that the integrand of the integral over ω in this equation is the probability density function for ω, given an ω'. In other words, the $L(\omega', E)$

function as defined in equation 2.49 is the probability density function for ω. Then the cumulative probability becomes

$$p\left(E,\omega,\omega'\right) = \frac{\int_{\omega_-}^{\omega} \omega' F(E,\omega',\omega)\mathrm{d}\omega}{\int_{\omega_-}^{\omega_+} \omega' F(E,\omega',\omega)\mathrm{d}\omega} = \frac{\log\left(1 - \frac{\omega'}{\omega}\right) - \log\left(1 - \frac{\omega'}{\omega_-}\right)}{\log\left(1 - \frac{\omega'}{\omega_+}\right) - \log\left(1 - \frac{\omega'}{\omega_-}\right)}. \quad (2.59)$$

Again we draw a random number U, set this equal to equation 2.59 and solve for ω to sample ω and we can calculate the energy of the primary electron after the inelastic scattering event as $E - \omega$. To determine the energy of the secondary electron we need the binding energy of this secondary electron. The binding energy E_b of the secondary electron is sampled by using the sub-shell cross sections from the evaluated photon data library (EPDL97) [25,26]. We know the energy loss ω will go to this secondary electron, but part of this energy loss is purely the momentum transfer q. Hence, the binding energy of the secondary electron can at maximum be equal to ω'. The energy of the secondary electron E_{se} becomes

$$E_{se} = \omega - E_b + E_F. \quad (2.60)$$

This energy is defined with respect to the bottom of the band by including the Fermi energy. The derivation of the scattering angles is described in detail by Verduin [10] and we will not repeat this. However, Verduin used a non-relativistic approximation to the scattering angles. As a result, Verduin derives the following for the momentum of the secondary electron after the scattering event

$$\hat{\boldsymbol{p_s''}} \sim \hat{\boldsymbol{p_s'}} + \frac{E_b}{\omega + E_b}\hat{\boldsymbol{r}}, \quad (2.61)$$

where $\hat{\boldsymbol{p_s'}}$ is the scatter direction of the secondary electron without taking its instantaneous momentum into account as derived by Verduin and $\hat{\boldsymbol{r}}$ is defined as

$$\hat{\boldsymbol{r}} = \sin\theta\cos(2\pi U_1)\hat{\boldsymbol{x}} + \sin\theta\sin(2\pi U_1)\hat{\boldsymbol{y}} + \cos\theta\hat{\boldsymbol{z}}, \quad (2.62)$$

where $\cos\theta = 2U_2 - 1$ and U_1 and U_2 are both random numbers from the

uniform distribution between 0 and 1. Kieft and Bosch did have the option to
use this non-relativistic approximation, but as default behaviour, they used
the full relativistic expression. We decided to keep the relativistic expression,
and equation 2.61 becomes

$$\hat{\boldsymbol{p}}_s'' = \hat{\boldsymbol{p}}_s' + \frac{E_b\left(E_b + 2mc^2\right)}{\left(\omega + E_b\right)\left(\omega + E_b + 2mc^2\right)}\hat{\boldsymbol{r}}. \tag{2.63}$$

Now we can of course still use conservation of momentum to calculate the
momentum of the primary electron after the scattering event

$$\hat{\boldsymbol{p}}_p' = \hat{\boldsymbol{p}}_p - \hat{\boldsymbol{p}}_s''. \tag{2.64}$$

2.1.3   Boundary crossing

When an electron approaches the interface between vacuum and a material,
it has to cross a potential barrier to either go from vacuum into the material
or to escape the material. The height of this potential barrier is the difference
between the minimum energy in the material and the vacuum level. This
potential barrier is calculated differently in metals and in insulators. In
Figure 2.14 the band structures of metals and insulators are shown. In a
metal the height of the potential barrier U is

$$U = E_F + W_f, \tag{2.65}$$

where E_F is the Fermi energy and W_f the work function. This can also be
seen in Figure 2.14a. Kieft and Bosch calculate the height of the potential
barrier U in an insulator or semiconductor by using the same equation, but
substituting the electron affinity EA for the work function W_f: $U = E_F +
EA$. However, as can be seen in Figure 2.14b, the height of the barrier
also includes part of the band gap. We assume that the Fermi energy lies
midway the band gap E_G, the potential barrier height in an insulator or
semiconductor is then

$$U = E_F + EA + \frac{1}{2}E_G. \tag{2.66}$$

For some materials, we do not know the Fermi energy. However, we know
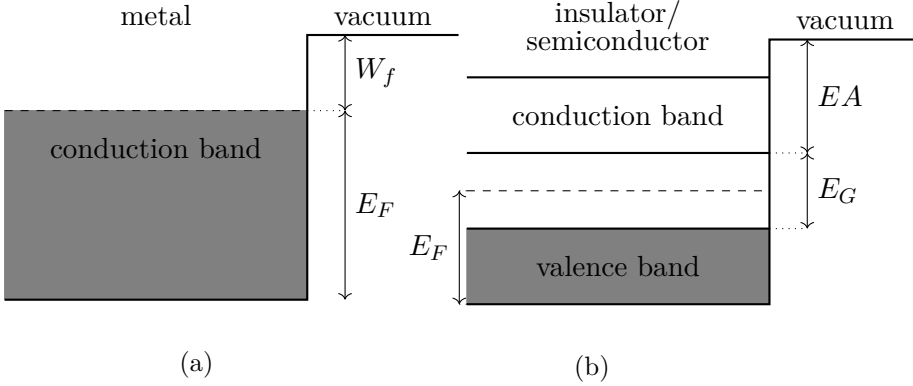
Figure 2.14: **(a)** The band structure at a boundary between a metal and vacuum. **(b)** The band structure at a boundary between a semiconductor or an insulator and vacuum.

that '0' energy has to be below the valence band maximum, hence the barrier is at least the electron affinity plus the band gap. So in the case where we do not know the Fermi energy, we assume the potential barrier height is

$$U = EA + E_G. \tag{2.67}$$

We used this improved model to calculate the potential barrier height for insulators and semiconductors. To determine whether the electron is transmitted or reflected at the boundary, a quantum mechanical expression for transmission and reflection at a potential step is used [27]. The probability to transmit is

$$T(E, \theta) = \begin{cases} \dfrac{4\sqrt{1 - \frac{\Delta U}{E \cos^2 \theta}}}{\left(1 + \sqrt{1 - \frac{\Delta U}{E \cos^2 \theta}}\right)^2}, & \text{if } E \cos^2 \theta > \Delta U \\ 0, & \text{otherwise.} \end{cases} \tag{2.68}$$

Where θ is the angle between the momentum of the electron and the boundary surface normal and ΔU is defined as U in the case of an electron in a material approaching the surface boundary with vacuum. An electron travelling in vacuum and approaching a material will see a potential barrier of

$\Delta U = -U$. When an electron is internally reflected in a material (it does not escape into vacuum), there is a possibility that the electron is absorbed in the models of Kieft and Bosch. The probability for absorption P_a is calculated with

$$P_a = e^{1 - \frac{E}{2U}}.$$ (2.69)

However, there is no theoretical model to explain why the electron would be absorbed, it could still scatter elastically and approach the surface boundary again. If the energy of the electron is higher than the potential barrier, it could still escape. We have removed this surface absorption process in our simulator.

2.1.4 Trapping

For insulators like alumina, we know charging may play a big role. To include charging in a Monte Carlo simulation is a big challenge. In the Monte Carlo simulation all primary electrons are dealt with as separate non-interacting particles. However, to take charging into account, we need to realise that every new primary and secondary electron changes the charge distribution of the sample. In other words, the electric field changes with every new primary or secondary electron, and needs to be updated accordingly. The Monte Carlo simulation is now extended with a multi-body problem. Current simulators are not able yet to deal with this kind of problem. One solution would be to simulate a certain amount of primary electrons, say 100 primaries and their secondary electrons, determine the resulting electric field due to the emission and/or absorption of all these electrons and then again simulate 100 primary electrons that hit the sample. We have decided to not use this method, because it would significantly slow down the simulation, and still be an approximation to the real solution. However, we have included a trapping model, where electrons are trapped with a probability depending on their energy. This model in effect also decreases the secondary electron yield and it does not slow down the simulation. The trapping model we used

is proposed by Ganachaud et al. [28].

$$\frac{1}{\lambda_{trap}(E)} = S_{trap} \exp\left(-\gamma_{trap}E\right), \tag{2.70}$$

where S_{trap} and γ_{trap} are used as fitting parameters to fit simulated to experimental yield curves.

2.2   Photon related models

When a photon beam irradiates a material, depending on the material and the energy of the photon, the photon can be absorbed in the material, it can travel through the material, or it can be reflected. The respective probabilities for these processes depend on the photon energy. The photon energies considered in this work are in the order of a few 100 eV. At these energies, the materials considered are opaque for the irradiating photons, which means the photons will be absorbed in the material, or reflected. When the photon is absorbed, a secondary electron will be created. This secondary electron can of course be simulated using the electron models discussed in the first part of this chapter. After absorption and creation of the secondary electron, an excited atom is left in the material. This atom will de-excite and return to the lowest energy state. Both these processes are discussed here.

2.2.1   Absorption

When a photon is absorbed in a material, it gives its energy to an electron in a shell around one of the atoms in the material. This electron will then be able to escape the potential binding it to the atom. This is illustrated in Figure 2.15. This whole process can only happen when the photon energy is higher than the binding energy of that specific shell. If the binding energy is higher than the photon energy, the electron cannot absorb the photon to become a photoelectron. However, if the photon energy is higher than the binding energy, the electron can escape the atom and become a photoelectron. The resulting photoelectron will then travel through the material, possibly creating secondary electrons as well, as described in the first part

of this chapter. Whether the photoelectron will be able to escape, depends
on the depth where the photon was absorbed and the photoelectron was cre-
ated. If the photon absorption occurred close to the surface, it is possible
that the photoelectron directly escapes without losing any energy. If the
absorption occurred further away from the surface, the photoelectron might
still be able to escape, but it will probably lose some of its energy before
reaching the surface, possibly creating a secondary electron in the process.
Hence the electron energy spectrum measured for a sample under photon ir-
radiation, directly depends on the photon absorption length. GEANT4 has
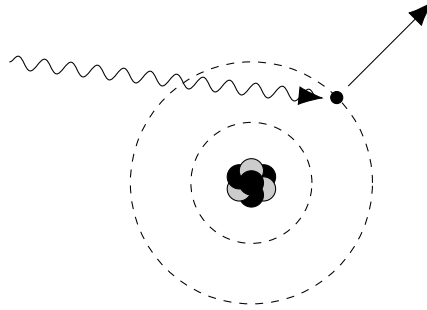
Figure 2.15: Model of the absorption of a photon by an atom. The electron
gains the photon energy and escapes from the atomic potential, leaving a
hole around the atom.

multiple models to simulate photon absorption and the creation of photo-
electrons. Most of these models are valid at high energies in the order of
GeV's. For the low energies we are interested in, we used the PENELOPE
model [29]. The PENELOPE model of photon absorption in GEANT4 uses
the Beer-Lambert law to calculate the photon absorption length

$$I(z, \nu) = I_0 e^{-z/\lambda(\nu)}, \tag{2.71}$$

where λ is the energy dependent absorption length of the photons and I_0 is
the intensity of the photon beam at $z = 0$. The absorption length can be
calculated from the photon absorption cross section

$$\lambda(\nu)^{-1} = \sigma(\nu)n, \tag{2.72}$$

with n the atomic density of the material in question. In the case of a compound, the inverse photon absorption length is the sum of the atomic inverse photon absorption lengths

$$\lambda(\nu)^{-1} = \sum_i \sigma_i(\nu) n_i. \tag{2.73}$$

The cross sections used in the PENELOPE model to calculate the absorption length are taken from the evaluated photon data library (EPDL97) [25, 26]. At the energies we are interested in, the uncertainty of the cross sections in the EPDL can be quite large. We have compared the absorption length for silicon nitride calculated using the EPDL cross sections to the absorption length obtained from the Center for X-Ray Optics (CXRO) [30]. In Figure 2.16 both these absorption lengths are shown for silicon nitride. We can see the absorption length increases with the photon energy, photons with a higher energy will be able to travel through the sample longer before being absorbed. At 410 eV we see a jump in the absorption length. At this energy, a new electron shell around nitrogen becomes available to be excited. This new absorption mode decreases the absorption length, since now there are more electrons available to absorb the photon. There is a small difference between the EPDL and the CXRO absorption lengths, but the general trends correspond. We conclude we can use the absorption lengths from GEANT4 in our simulations.

In order to create a photoelectron, it is still necessary to determine the angle with which the photoelectron is emitted with respect to the direction of the photon before absorption. The angular distribution in which the photoelectron is emitted in GEANT4 is determined by using the Sauter distribution [31]. In the implementation of this model in PENELOPE [29], Salvat assumed that the incoming photons are not polarised and the distribution in ϕ_e is isotropic. The angular distribution for the polar angle θ_e, apart from a normalisation constant, is

$$p(\nu) = (2 - \nu) \left[\frac{1}{A + \nu} + \frac{1}{2} \beta\gamma(\gamma - 1)(\gamma - 2) \right] \frac{\nu}{(A + \nu)^3}, \tag{2.74}$$
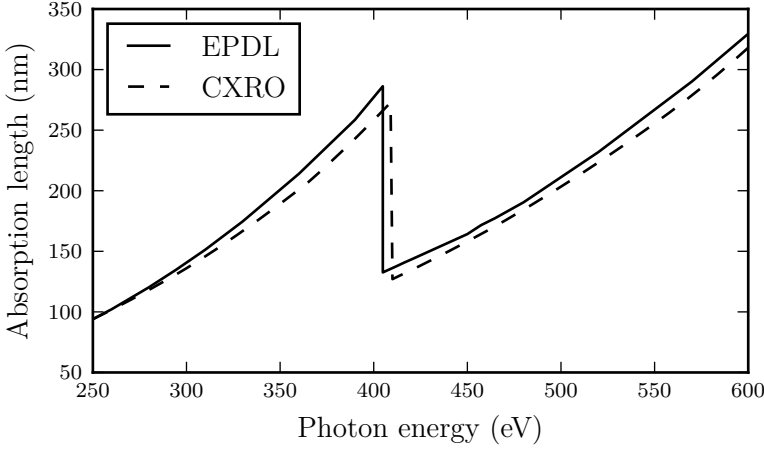
Figure 2.16: The calculated absorption length using the EPDL cross sections compared to the absorption length from the CXRO database for Si_3N_4 as a function of photon energy.

with

$$\gamma = 1 + \frac{E_e}{m_e c^2}, \qquad\qquad \beta = \frac{\sqrt{E_e\left(E_e + 2m_e c^2\right)}}{E_e + m_e c^2}, \qquad (2.75)$$

$$A = \frac{1}{\beta} - 1, \qquad\qquad \nu = 1 - \cos\theta_e. \qquad (2.76)$$

This angular distribution is derived using K-shell electron wave functions for hydrogen. Salvat points out that this angular distribution is only adequate for ionisation of the K-shell by high-energy photons. Salvat continues to reason that for most practical applications this approximation is accurate enough, since the mean free path of the (photo)electrons is much shorter than that of the photons. Most photoelectrons have lost all information about their initial direction long before they reach the surface. In Figure 2.17 we have plotted the Sauter angular distribution for different electron energies. We can see that for low electron energies, the photoelectron is mostly emitted perpendicular to the direction of the photon. For high energies, the photoelectron is emitted in the same direction as the incoming photon.
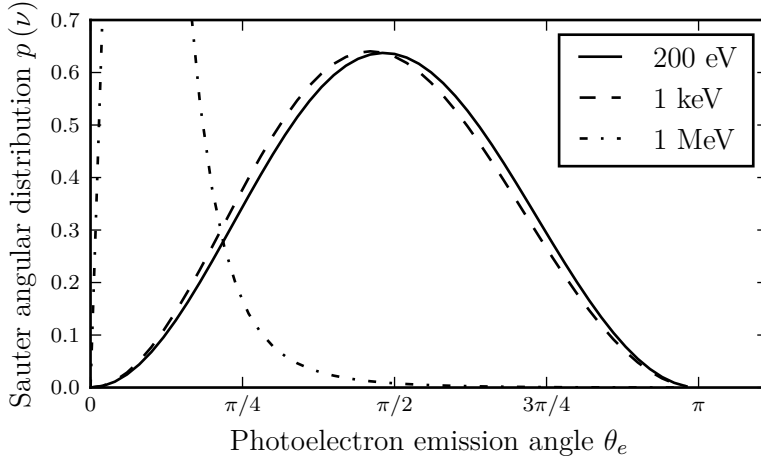
Figure 2.17: The Sauter distribution for different electron energies. For high energies, the photoelectrons are mostly emitted in the same direction as the incoming photon. For lower energies, the photoelectrons are mostly emitted perpendicular to the direction of the incoming photon.

2.2.2 De-excitation

After the absorption of a photon and the emission of a photoelectron, a hole is left in the material. In Figure 2.15 the emitted photoelectron originates from the most outer shell of the atom. Now this atom is in the lowest possible energy state. However, if the photon energy was high enough such that the photoelectron originated from a shell with a higher binding energy, the atom is left in an excited state and it has to de-excite. There are two de-excitation processes possible. First, an electron from a higher shell can fall back to the hole, and the excess energy of this electron can leave in the form of an X-ray photon. This process is called fluorescence. The other process by which the atom can de-excite is Auger emission. In this case the excess energy of the electron falling back is given to an electron from an even higher shell, which then is able to escape the atom. The photon energy necessary to create the first Auger electron is called the Auger edge. Both these processes are illustrated in Figure 2.18. These two processes are also used in GEANT4 to de-excite an atom in excited state. The combined cross section for these
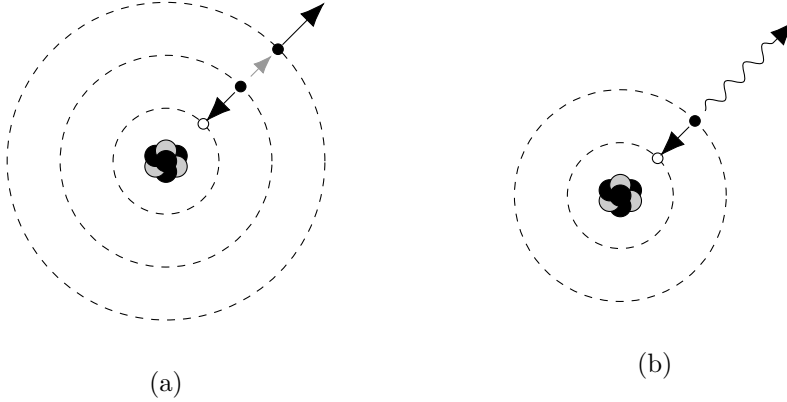
Figure 2.18: Model of the de-excitation processes of an atom. **a)** The emission of an Auger electron and **b)** fluorescence, the emission of an X-ray.

two processes is normalised to one. In other words, when an atom is left in an excited state, it has to de-excite. The cross sections for both de-excitation processes used in GEANT4 are from the evaluated atomic data library (EADL) [32]. To get an idea of how this works, the transition data for nitrogen are shown in Table 2.1. The total probability to emit an Auger electron when there is a hole in the K shell is 99.7%, the probability to emit an X-ray is only 0.3%. Later in this work we will discuss experiments where silicon nitride is irradiated with photons. For silicon, the probability to emit an X-ray is smaller than 5% when there is a hole in the K shell and smaller than 1% when there is a hole in the L1, L2 or L3 shell. We are interested in photon energies for which the K shell of silicon is not accessible. This means that, in our simulations, when an atom in silicon nitride is left in an excited state after the absorption of a photon and the emission of a photoelectron, in more than 99% of the cases the atom de-excites by emitting an Auger electron.

2.3 Summary

In the first part of this chapter we have discussed the electron models we used in our simulations. The electron models are based on the models developed

Auger		
shell of 'new' hole	**shell of emitted Auger electron**	**probability**
L1	L1	0.265
L1	L2	0.130
L1	L3	0.258
L2	L2	0.008
L2	L3	0.213
L3	L3	0.122
total probability Auger		0.997

Fluorescence	
shell of 'new' hole	**probability**
L2	0.001
L3	0.002
total probability fluorescence	0.003

total probability	1

Table 2.1: The probability for emitting an Auger electron or an X-ray when there is a hole in the K shell of a nitrogen atom. In both cases an electron falls back and leaves a 'new' hole.

by Kieft and Bosch. We have discussed these original models and the changes we made. Here we will shortly list the electron models and the changes we made with respect to the original models of Kieft and Bosch.

To calculate the elastic mean free path, Kieft and Bosch used two different models for different energy regimes. Up to 200 eV they used acoustic phonon scattering taking only longitudinal acoustic phonons into account. Above 200 eV, they used Mott cross sections. Kieft and Bosch used Mott cross sections calculated without taking solid state effects into account. We recalculated the Mott cross sections with ELSEPA, taking solid state effects into account. For the lower energies, where the acoustic phonon scattering model is used, we extended the model to a dual branch phonon model. The acoustic phonon scattering model now includes the two transversal modes as well as the longitudinal acoustic phonon modes.

The inelastic mean free path is calculated by Kieft and Bosch using the

dielectric function theory. We went back to the paper by Ashley where Kieft and Bosch based there model on. We found an error in the integration bounds for the L-function, which we corrected. We also improved the Fermi correction from Kieft and Bosch and we were able to remove the phenomenological factor of 1.5 introduced by Kieft and Bosch.

When an electron encounters a material boundary, the probability to transmit or reflect the electron is determined using the quantum mechanical transmission probability at a potential step. We corrected the calculation of the height of the potential step for insulators and semiconductors. Kieft and Bosch also introduced an absorption process for electrons that are internally reflected at the surface of a material. We could not find any physical reason to explain this absorption process, so we decided to remove this absorption process.

In the Kieft and Bosch models, there is no model present to account for charging. We propose to use a model to trap electrons inside the material in order to take some charging effects into account.

In the beginning of this Chapter it was mentioned that a large part of the final electron models was already discussed by Verduin [10]. Let us shortly summarise the similarities and differences between our models and those used by Verduin. Both our models and Verduin's are based on the models of Kieft and Bosch. The changes we made to the elastic models were also made by Verduin. The corrections done to the inelastic scattering model and to the boundary model were not done by Verduin. However, he did remove the absorption process at the surface. Verduin also included surface plasmons, which we have decided not to include. The surface plasmon model proposed by Verduin is very dependent on the chosen thickness of the surface layer and our goal was to develop a simulator without any fitting parameters. We do have included a trapping process which does have fitting parameters, however, in the next Chapter the reader will find we decided not to use this process.

In the second part of this chapter we have discussed the phonon models we used in our simulations. The photon models we used are the PENELOPE models in GEANT4. In these models, the photon absorption length in matter

is determined by using the evaluated photon data library [26]. The angular distribution of the emitted photoelectrons is the Sauter distribution. After the emission of a photoelectron, an atom is left in an excited state. The atom can now de-excite through emitting an Auger electron or an X-ray. In GEANT4, the relative probabilities of these two processes are determined by using the transition probabilities from the evaluated atomic data library [32].

Now remains the question what the effect is of all these model changes to the electron models. In the next chapter we will discuss the effect of the model changes separately.

Chapter 3

Effects of model refinements

In this chapter we will discuss the effects of the model refinements we proposed in the previous chapter. We will implement the model refinements incrementally. In other words, every next section in this chapter will make use of the model refinements from the previous sections. The effects of all model refinements will be shown for silicon, gold and alumina. In this way we can see the effects for a semiconductor, a metal and an insulator. The material parameters used for these materials are given in appendix A.

3.1   Correction of the boundary process

The first model refinement we will discuss is the correction of the boundary crossing process for electrons crossing the potential barrier between a material and vacuum. As discussed in 2.1.3, the boundary crossing model refinements consist of removing the surface absorption process for internally reflected electrons, because there was no theoretical model to explain the presence of this absorption process, and correcting the calculation of the potential barrier height for insulators and semiconductors.

For semiconductors, like silicon, the correction to the potential barrier height is a small correction. When the Fermi energy level is known, the correction is half the band gap. In the case where the Fermi energy level is unknown, the correction to the potential barrier height is equal to the

Figure 3.1: The secondary electron yield of silicon as calculated with the original Kieft and Bosch models (solid line) and the refined boundary process (dashed line).

whole band gap. Since the band gap for silicon is only 1.12 eV, and the Fermi energy is known, the potential barrier height is increased by only 0.56 eV. This increase of the potential barrier height is expected to decrease the secondary electron yield. However, removing the surface absorption for an internally reflected electron is expected to increase the secondary electron yield, since this absorption process in the Kieft and Bosch models removes electrons that could still have escaped the material. For semiconductors, we expect the secondary electron yield to increase when we apply both these refinements to the boundary process, because the increase of the potential barrier height is very small. This can indeed be seen in Figure 3.1, where we see an increase in secondary electron yield when we go from the original Kieft and Bosch models (solid line) to the refined boundary process (dashed line).

In metals, like gold, the calculation of the height of the potential barrier was correct in the Kieft and Bosch models. This means, in the case of metals, the refinements to the boundary process are effectively only a removal of the surface absorption process for internally reflected electrons. Hence for gold

Figure 3.2: The secondary electron yield of gold as calculated with the original Kieft and Bosch models (solid line) and the refined boundary process (dashed line).

we expect the secondary electron yield to increase, as can be seen in Figure 3.2, where the yield increases when we go from the original Kieft and Bosch models (solid line) to the refined boundary process (dashed line).

For insulators, like alumina, the band gap is bigger and the correction to the calculation of the potential barrier is more important. In the case of alumina, the band gap is 7.0 eV and the Fermi energy level is unknown. This means the potential barrier in the refined boundary process is 7.0 eV higher than in the original models of Kieft and Bosch. In this case, we expect the effect of the barrier correction, decreasing the secondary electron yield, to be stronger than the increase of the secondary electron yield due to the removal of the surface absorption model. Hence we expect the secondary electron yield for alumina to decrease with the implementation of the boundary process refinements. Figure 3.3 illustrates this effect, where the secondary electron yield decreases when we go from the original Kieft and Bosch models (solid line) to the refined boundary process (dashed line).

We do not expect the boundary process refinements to affect the backscatter yield. The correction of the barrier height calculation, will only effect
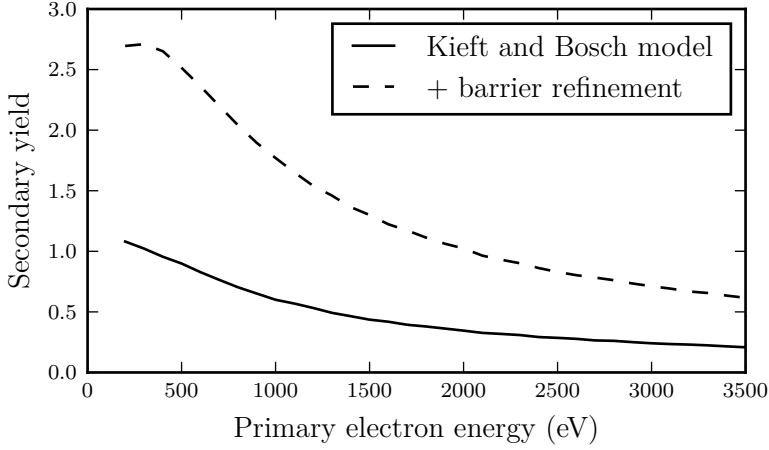
Figure 3.3: The secondary electron yield of alumina as calculated with the original Kieft and Bosch models (solid line) and the refined boundary process (dashed line).
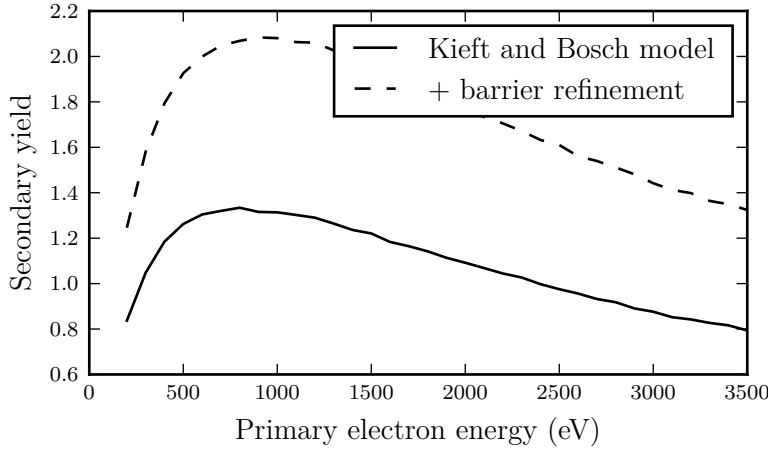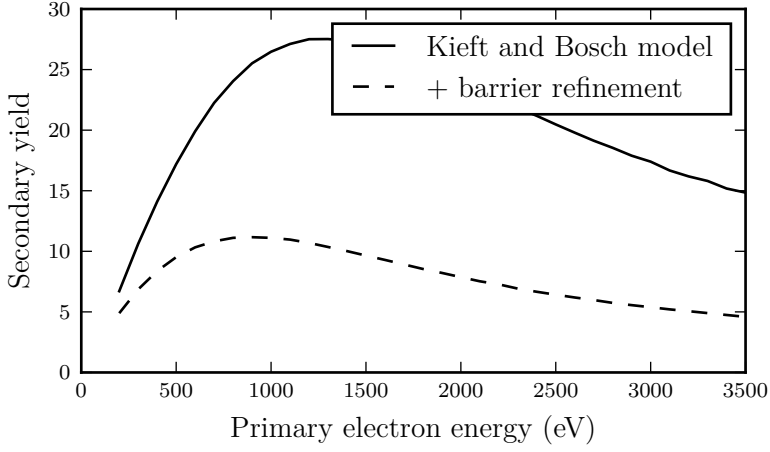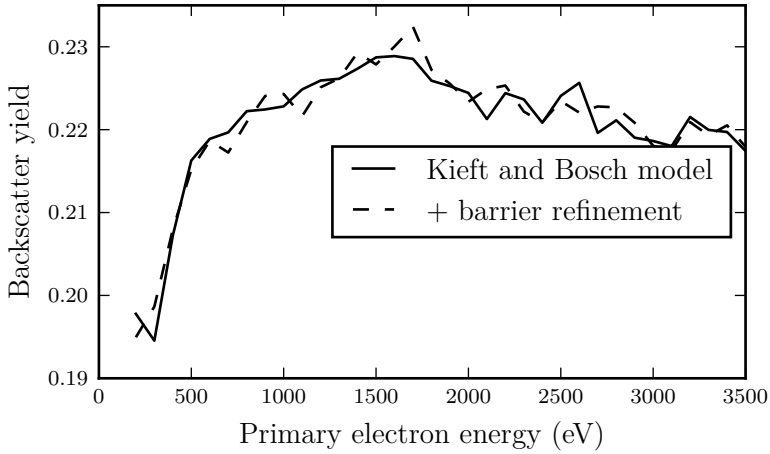

Figure 3.4: The backscatter yield of silicon as calculated with the original Kieft and Bosch models (solid line) and the refined boundary process (dashed line).

electrons that have an energy close to the barrier height. Backscatter electrons have an energy more than 50 eV by definition, so we do not expect the

correction of the barrier height to affect the backscatter yield significantly. The same holds for the surface absorption process. The probability for an internally reflected electron of 100 eV to be absorbed in gold in the Kieft and Bosch model is less than 3% and this probability decreases with increasing energy. Because this absorption probability was already so small, we do not expect the backscatter yield is affected significantly by removing the absorption process. In Figure 3.4 we see the backscatter yield of silicon for the Kieft and Bosch models (solid line) and the refined barrier process (dashed line), where both curves are the same within statistical fluctuations. The effect of the refinements to the boundary process on the backscatter yields of gold and alumina was similar as for silicon.

3.2   Elastic scattering model refinements

The elastic scattering models are divided into a model for high energies; Mott cross sections, and a model for low energies; acoustic phonon scattering. In both these two energy regimes, we have introduced model refinements.

For energies above 200 eV, Kieft and Bosch used atomic Mott cross sections for free atoms, from now on, we will refer to these as the 'old Mott cross sections'. We used Mott cross sections calculated with ELSEPA, where the atomic potential used is corrected for solid state effects which are present in a material, from now on, we will refer to these as the 'new Mott cross sections'.

Elastic scattering at low energies is modelled by acoustic phonon scattering as detailed in 2.1.1.1. We have introduced several model refinements to the acoustic phonon scattering models. From now on, we will refer to the acoustic phonon scattering model as used by Kieft and Bosch as the 'old phonon model'. The acoustic phonon scattering model with our refinements will be referred to as the 'dual branch phonon model'.

The effects of the new Mott cross sections and the dual branch phonon model on the secondary electron and backscatter yields of silicon, gold and alumina will be discussed per material, since these effects not only depend on the models themselves, but also on the ratio of elastic and inelastic scattering.

3.2.1   Silicon

In the previous chapter we saw that the elastic mean free path of silicon increases above 200 eV when using the new Mott cross sections. The elastic and inelastic mean free paths above 200 eV are very close to each other as can be seen by comparing the mean free paths for silicon from Figure 2.1 and 2.11. In fact, the elastic mean free path of silicon in the range of 200 eV to 3 keV as calculated with the old Mott cross sections is slightly lower than the inelastic mean free path as calculated by Kieft and Bosch. In the same energy range, the elastic mean free path calculated with the new Mott cross sections is always higher than the inelastic mean free path as calculated by Kieft and Bosch. This means the probability for a primary electron to backscatter immediately becomes smaller (for primary energies above 200 eV) than the probability to scatter inelastically and lose energy, when we introduce the new Mott cross sections. As a result, we expect the backscatter yield of silicon to decrease when we use the new Mott cross sections. This effect can indeed be seen in Figure 3.5, where the backscatter yield for primary energies higher than 1 keV decreases when we go from the old Mott cross sections (solid line) to the new Mott cross sections (dashed line).

The dual branch phonon model will only affect the elastic mean free path below 200 eV. This is not expected to affect the backscatter yield, because most backscatter electrons are in the Mott cross section regime. This can be seen in Figure 3.5. The difference between the backscatter yield with only the new Mott cross sections (dashed line) and the backscatter yield with the dual branch phonon model (dash-dotted line) is smaller than the statistical fluctuations.

The increase in elastic mean free path, causes the primary electrons to travel further into the material before their first scatter event. This will lead to a small decrease in the secondary electron yield, because the secondary electrons now have to travel further to be able to escape from the material. These secondary electrons have less than 50 eV by definition and have the same elastic mean free path with the new Mott cross sections as before, so they will have the same range as before. At the same time, we expect the secondary electron yield maximum to shift to a lower optimum primary

Figure 3.5: The backscatter yield of silicon for the different elastic scattering models. The original elastic models of Kieft and Bosch (including the boundary process refinements) give the solid line, the new Mott cross sections give the dashed line, and also including the dual branch phonon model gives the dash-dotted line.

energy, where the optimum primary energy is defined as the primary energy for which the secondary electron yield reaches its maximum. At this lower energy, the primary electrons will have their first interaction in the material closer to the surface. As a result, the whole electron cloud in the material shifts closer to the surface and it is easier for the secondary electrons to escape than at the old optimum primary energy. In Figure 3.6, we can see both these effects on the secondary electron yield. For the old Mott cross sections, the maximum secondary electron yield is 2.7 at 300 eV. The use of the new Mott cross sections decreases the maximum secondary electron yield to 2.4 and shifts the optimum primary energy to 200 eV.

When we then also introduce the dual branch phonon model, the elastic mean free path below 200 eV increases. This longer mean free path is expected to shift the maximum secondary electron yield to a higher optimum primary energy again. This can be explained by the fact that at a higher primary energy, more secondary electrons will be created, albeit slightly
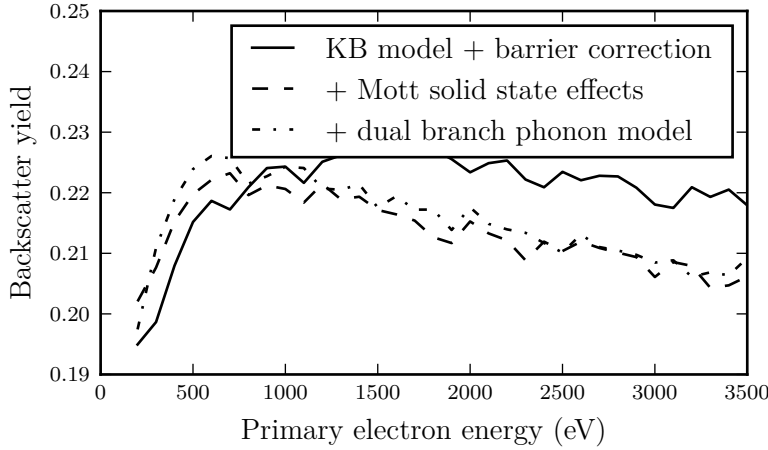
Figure 3.6: The secondary electron yield of silicon for the different elastic scattering models. The original elastic models of Kieft and Bosch (including the boundary process refinements) give the solid line, the new Mott cross sections give the dashed line, and also including the dual branch phonon model gives the dash-dotted line.

deeper into the material. Before, these electrons had a small probability to escape, since the elastic mean free path was smaller. Now the elastic mean free path of these secondary electrons is increased and they have a bigger probability to escape and contribute to the secondary electron yield. The balance of more secondary electrons created at a larger depth, but with a longer range, leads to a shift of the optimum primary energy to a higher energy. In Figure 3.6 we can see that indeed the secondary electron yield maximum shifts from 200 eV (dashed line) to 400 eV (dash-dotted line) when including the dual branch phonon model. We also see that the maximum of the secondary electron yield is decreased from 2.44 (dashed line) to 2.39 (dash-dotted line) in Figure 3.6. Due to the increase in elastic mean free path at low energies, the inelastic mean free path is lower than the elastic mean free path in between 40 eV and 100 eV. In other words, in this energy range, inelastic scattering becomes the dominant process and electrons in this regime will lose their energy faster. This explains the decrease in the

secondary electron yield.

3.2.2 Gold

Similar as for silicon, the use of the new Mott cross sections increases the elastic mean free path above 200 eV for gold. This increase causes the primary electrons to travel slightly further into the sample before the first scattering event. However, for gold, the elastic mean free path is still lower than the inelastic mean free path in the energy range between 200 eV and 3 keV. This is why we do not expect a big effect on the backscatter yield, which is confirmed in Figure 3.7, where there is only a very small change in the backscatter yield when we go from the old Mott cross sections (solid line) to the new Mott cross sections (dashed line).
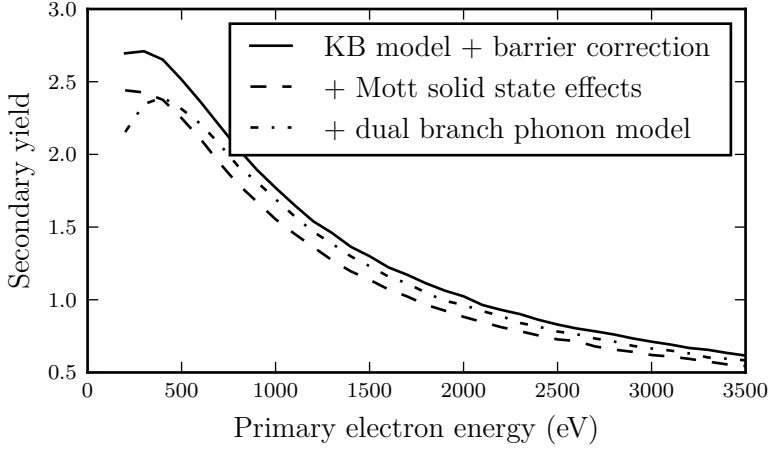

Figure 3.7: The backscatter yield of gold for the different elastic scattering models. The original elastic models of Kieft and Bosch (including the boundary process refinements) give the solid line, the new Mott cross sections give the dashed line, and also including the dual branch phonon model gives the dash-dotted line.

Again, we do not expect the phonon dual branch model to affect the back scatter yield, since the backscatter electrons are in the Mott cross section regime. We can see this in Figure 3.7, where there is no difference between

the backscatter yield with the new Mott cross sections (dashed line) and the backscatter yield also including the dual branch phonon model (dash-dotted line).

The use of the new Mott cross section decreases the elastic mean free path in between the Fermi energy (5.53 eV) and 40 eV. This decrease means the secondary electrons will scatter more elastically and their track will fold more into itself. This will decrease the range of the secondary electrons. As a result, the optimum primary energy will decrease, because at the old optimum primary energy, more of the secondary electrons created are created too deep into the material and will not be able to escape. In Figure 3.8 we indeed see that the secondary electron yield maximum shifts from ~ 900 eV to 800 eV, when we go from the old Mott cross sections (solid line) to the new Mott cross sections (dashed line). In this Figure, we also see that the maximum of the secondary electron yield increases when we use the new Mott cross sections. Now we have to realise we are still using the model for acoustic phonon scattering of Kieft and Bosch, which means the Mott cross sections will affect the mean free path down to the Fermi energy. When we use the old Mott cross sections, the inelastic mean free path between 10 eV and 30 eV is smaller than the elastic mean free path. With the new Mott cross sections, the elastic mean free path is always smaller than the inelastic mean free path. In other words, we lose the region where the inelastic process is the dominant process and for secondary electrons with energies between 10 eV and 30 eV, the relative probability to lose energy and end up below the surface barrier decreases. This leads to an increase in the secondary electron yield.

When we then introduce the phonon dual branch model, the elastic mean free path increases again between the Fermi energy and 200 eV, increasing the secondary electron range. Using the same reasoning as before, this will shift the maximum secondary electron yield to a higher primary energy. In fact, in Figure 3.8 we see the secondary electron yield maximum shift from 800 eV to 1000 eV.
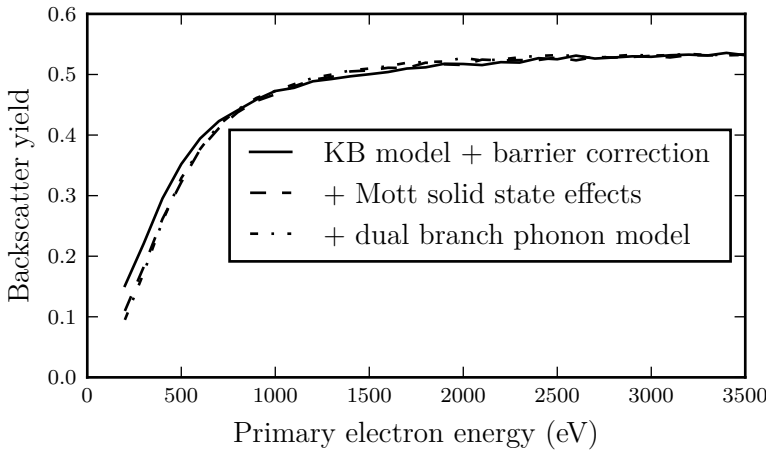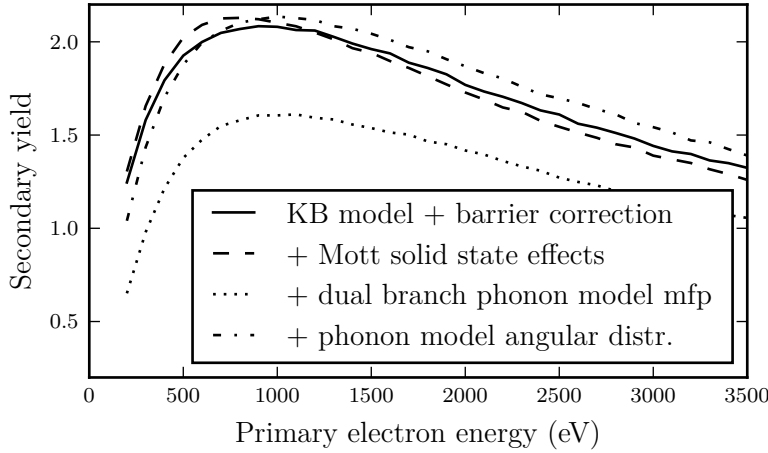
Figure 3.8: The secondary electron yield of gold for the different elastic scattering models. The original elastic models of Kieft and Bosch (including the boundary process refinements) give the solid line, the new Mott cross sections give the dashed line, and also including the dual branch phonon model gives the dash-dotted line. The dotted line is the result of only including the mean free path of the dual branch phonon model while still using the angular distribution of Kieft and Bosch.

3.2.2.1   Angular distribution

With the new elastic mean free path, the inelastic mean free path is smaller than the elastic mean free path in between ~ 10 eV to ~ 130 eV. Which means we would expect the electrons in this energy regime to lose their energy more quickly and we would expect the yield to decrease. However, the maximum value for the yield does not change when using the full dual branch phonon model. We have to realise that for metals, including the full dual phonon model brings in two refinements. The first refinement is the new mean free path. The second is the angular distribution between the Fermi energy and 200 eV. In the model of Kieft and Bosch, the angular distribution in the whole phonon regime is the angular distribution for $E < E_{BZ}/4$ as given in equation 2.31. This angular distribution is almost an isotropic angular distribution. In between the Fermi energy and 100 eV, the elastic mean free

path as well as the angular distribution is interpolated between the acoustic phonon model and the Mott cross sections. In between 100 eV and 200 eV the Mott cross sections are used. The angular distribution of the Mott cross sections is mostly forward directed at high energies and becomes more and more isotropic for lower energies. The combination of this gives an angular distribution which is isotropic at low energies and becomes forward directed for higher energies in the original model of Kieft and Bosch for elastic scattering in metals.

However, when we use the dual branch phonon model for metals, we introduce the angular distribution of the 'high energy' phonon scattering for $E > E_{BZ}$ in the energy regime $E_{BZ} < E < 100$ eV and in between 100 eV and 200 eV, the angular distribution is interpolated between the 'high energy' phonon and the Mott cross section angular distributions. The angular distribution of the 'high energy' phonon model is more forward scattered for higher energies, like the Mott cross sections, but for lower energies, it is backward directed. Which means the trajectory of electrons becomes more folded into itself at these lower energies.

If we use the elastic mean free path calculated with the dual branch phonon model in combination with the angular distribution of the original Kieft and Bosch model, we indeed see that the secondary electron yield decreases, as we expected from comparing the elastic mean free paths. This is shown by the dotted line in Figure 3.8, which has a decreased yield compared to the secondary electron yield when we only use the new Mott cross sections (dashed line).

If we now also use the angular distribution from the dual branch phonon model, the elastic mean free path becomes more folded into itself. Roughly speaking, we could say that before, if a low energy electron was moving away from the surface, it would 'almost' never scatter back towards the surface. Using the new angular distribution introduces a regime where elastic scattering is mostly directed backward. So during an elastic scattering event, an electron in this regime moving away from the surface has a bigger probability to scatter back and still escape from the sample. This effect leads to an increase in the yield. We can see this in Figure 3.8, where the secondary elec-

tron yield increases from only using the mean free path as calculated with the dual branch phonon model (dotted line) to also including the angular distribution (dash-dotted line).

3.2.3   Alumina

The effect of the new Mott cross sections on the elastic mean free path of alumina is similar to silicon and gold; the elastic mean free path above 200 eV is increased slightly. At 200 eV, the new mean free path is still very close to the old mean free path. At 10 keV, the new mean free path is only a factor of ~ 1.8 higher than the old mean free path. The new elastic mean free path is still lower than the inelastic mean free path in the energy range 200 eV to 10 keV. The increase in elastic mean free path is again expected to decrease the backscatter yield. Figure 3.9 shows a decrease in yield when we go from the Mott cross sections as used by Kieft and Bosch (solid line) to the new Mott cross sections (dashed line), as expected.
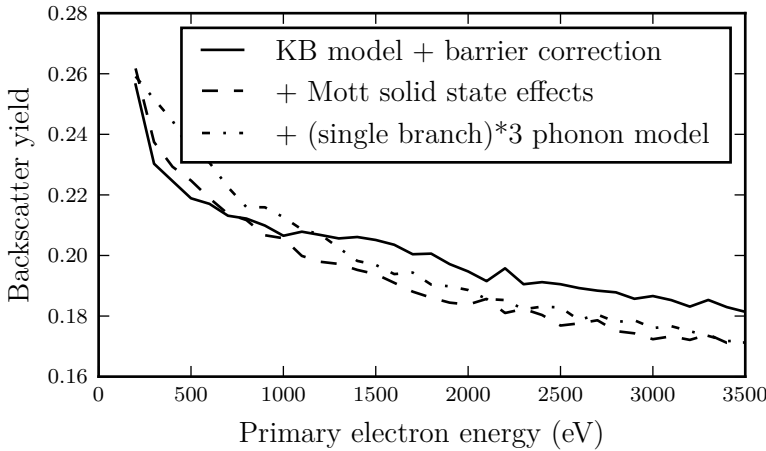
Figure 3.9: The backscatter yield of alumina for the different elastic scattering models. The original elastic models of Kieft and Bosch (including the boundary process refinements) give the solid line, the new Mott cross sections give the dashed line, and also including the approximation to the dual branch phonon model gives the dash-dotted line.

Again, we do not expect a significant effect of the new phonon model on the backscatter yield. Figure 3.9 confirms this where the backscatter yield of the original Kieft and Bosch phonon model (dashed line) and the new phonon model (dash-dotted line) are comparable.

Similarly as before, we expect the increase in elastic mean free path to decrease the secondary electron yield. Figure 3.10 indeed shows a decrease in yield when we go from the Mott cross sections as used by Kieft and Bosch (solid line) to the new Mott cross sections (dashed line).
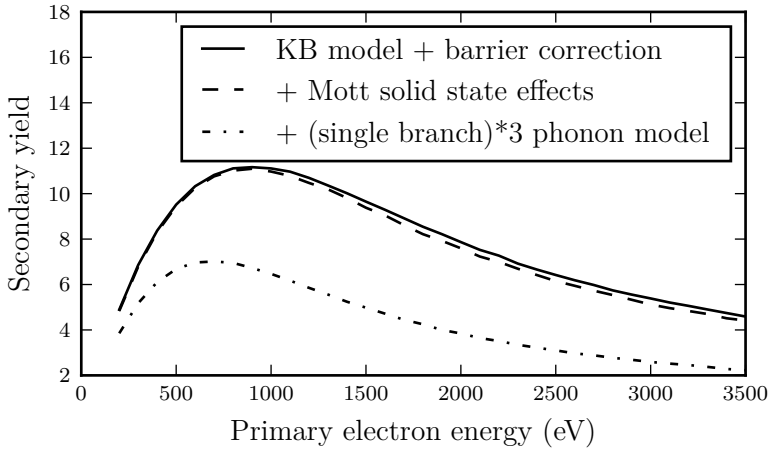
Figure 3.10: The secondary electron yield of alumina for the different elastic scattering models. The original elastic models of Kieft and Bosch (including the boundary process refinements) give the solid line, the new Mott cross sections give the dashed line, and also including the approximation to the dual branch phonon model gives the dash-dotted line.

The effect of using the approximation to the dual branch phonon model is that the elastic mean free path in the very low energy regime $E < E_{BZ}/4$ does not change significantly. In the 'high energy' phonon regime $E_{BZ} < E < 100$ eV, the elastic mean free path increases. Elastic scattering is still the dominant process in this energy regime, but it becomes less dominant. This means that of all scatter events there will relatively be more inelastic scatter events with the dual branch approximation compared to the original

Kieft and Bosch phonon model. In other words, electrons will lose energy in relatively more events. This is expected to decrease the secondary electron yield. The secondary electron yield indeed decreases when we go from the original Kieft and Bosch phonon model (dashed line) to the dual branch approximation (dash-dotted line) in Figure 3.10.

3.3 Inelastic scattering model refinements

Figure 3.11: The secondary electrons yields of silicon and gold with the original Kieft and Bosch inelastic models (solid and dash-dotted line) and the refinements to the inelastic scattering models (dashed and dotted lines).

The inelastic scattering model refinements do not have a big effect on the inelastic mean free paths of silicon, gold and alumina. The increase in inelastic mean free path leads to an increased relative probability for the primary electrons to scatter back, hence the backscatter yields for all three materials increases. The extra backscattered electrons are now no longer able to create secondary electrons in the material and, as a result, the secondary electron yield for all three materials decreases. Because the effects for all three materials are so similar, only the results for the secondary electron yield and the backscatter yield for silicon and gold are shown in Figures
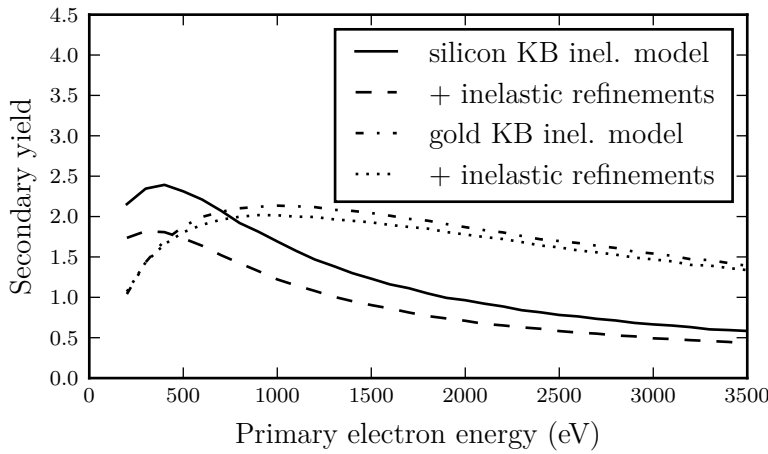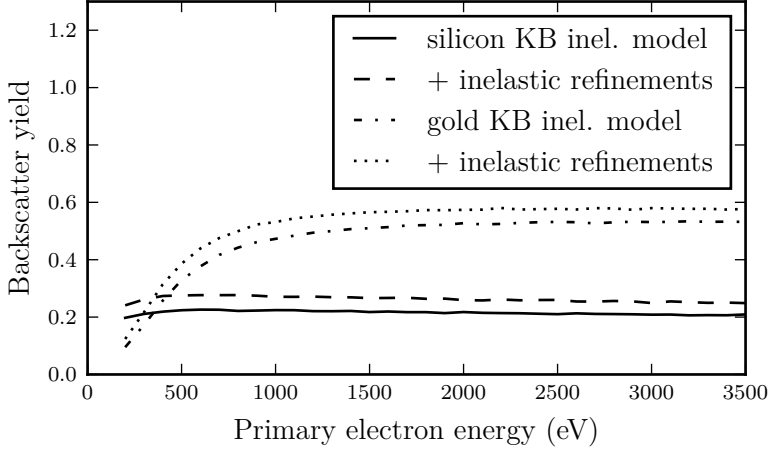
Figure 3.12: The backscatter yields of silicon and gold with the original Kieft and Bosch inelastic models (solid and dash-dotted line) and the refinements to the inelastic scattering models (dashed and dotted lines).

3.11 and 3.12, where the solid and dash-dotted lines are the yields including the barrier correction and the elastic scattering model refinements, but with the Kieft and Bosch inelastic models for silicon and gold respectively. And the dashed and dotted lines are the results including the inelastic model refinements for silicon and gold respectively.

3.4 Trapping

The trapping model we used is a very simple model. Depending on the energy of the electron, there is a probability the electron will be trapped inside the material. The smaller the electron energy, the bigger the probability to trap the electron. Once an electron is trapped, it will stay trapped, and it is removed from the simulation. The backscatter yield of insulators is not affected by this trapping process, since most backscatter electrons are electrons that have only undergone one elastic scattering event. The probability for these primary electrons to be trapped immediately after entering the material is negligible, due to their high energy. The secondary electron yield

however, will be greatly affected by the trapping process, since secondary
electrons have a low energy. For example, in alumina, a primary electron
with energy 100 eV has a trapping mean free path of ~ 72 km. A secondary
electron with energy 10 eV has a trapping mean free path of 12 nm, which
is in the order of the inelastic mean free path at this energy. The trapping
parameters used here are $S_{trap} = 1$ nm^{-1} and $\gamma_{trap} = 0.25$ eV^{-1}, as used by
Ganachaud as 'reference values' [28], the same values were used in [33]. We
expect the trapping process to decrease the secondary electron yield of alu-
mina significantly. In Figure 3.13, we indeed see that the secondary electron
yield is decreased. When the trapping process is not used, the maximum
secondary electron yield is 6.0, trapping decreases the maximum secondary
electron yield to 3.2.
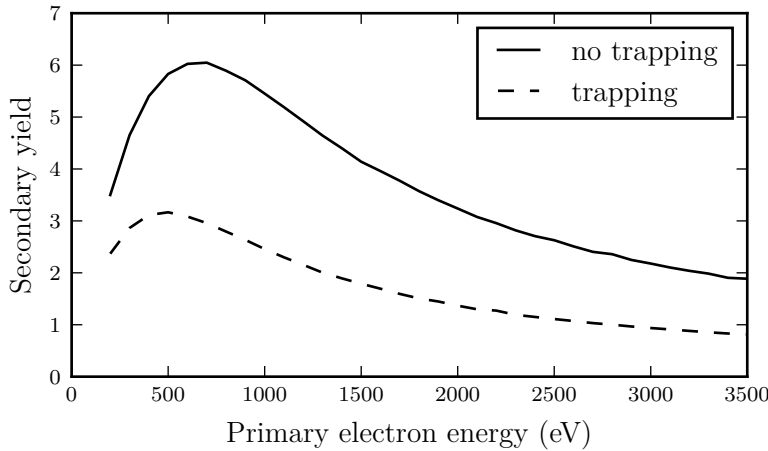
Figure 3.13: The secondary electron yield of alumina with (solid line) and
without (dashed line) the trapping process.

However, there is no theoretical explanation for determining the values of
the trapping parameters. Trapping can mostly be used as a fitting parameter
in order to reproduce experimental yield values, see for example [34]. Our
aim is to develop a simulator with first principle models, without using any
fitting parameters. This is why we have decided not to use the trapping
process in the rest of this research.

3.5   Energy distribution

Figure 3.14: The energy distribution of the emitted secondary electrons from a silicon sample for a primary electron energy of 1 keV. The solid line is the energy distribution obtained with the original Kieft and Bosch models, the dashed line is obtained including only the boundary process refinement, and the dash-dotted line also includes our model refinements to the elastic and inelastic models.

Up to now only the effect of our model refinements on the secondary electron and backscatter yields is examined. Another simulation result that can change with our model refinements, is the energy distribution of the emitted electrons. In Figure 3.14 and 3.15 the probability densities of the energy distribution for secondary electrons and backscatter electrons are shown respectively. The energy distribution of the secondary electrons is shifted slightly to lower energies with our model refinements to the boundary process and elastic and inelastic scattering (dash-dotted line) compared to the original Kieft and Bosch models (solid line). The implementation of the correction to the boundary crossing process (dashed line), causes the peak of the energy distribution of the secondary electrons to shift down from ~ 3.5 eV to ~ 1.5 eV. For lower energies (but still above the surface potential barrier) the probability to reflect becomes larger, but also the probability to be absorbed

after an internal reflection event. The combination of these two facts, leads to an increasing probability to prevent low energy electrons from escaping the material. Hence we expect the removal of the surface absorption process is the cause of the shift of this peak down to ~ 1.5 eV. The combined effect of all other model refinements shifts the peak back up to ~ 2.5 eV.

The energy distribution of the backscatter electrons is almost the same for our model refinements as for the original Kieft and Bosch models. The only difference is the direct backscatter peak at 1 keV, which is slightly higher than with the original models.
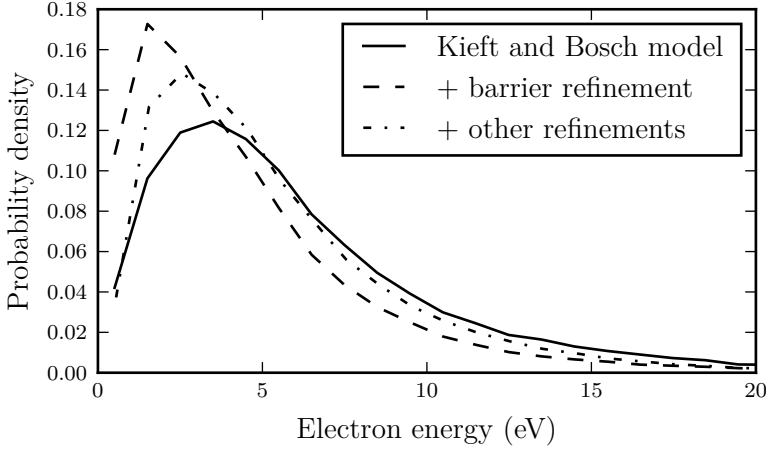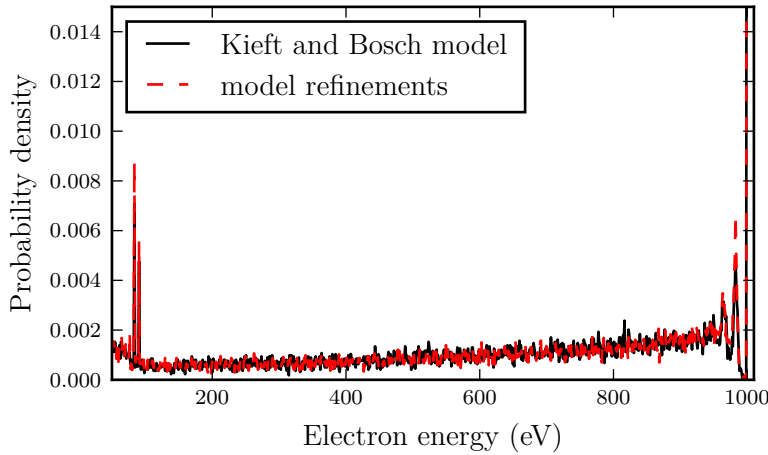

Figure 3.15: The energy distribution of the emitted backscatter electrons from a silicon sample at a primary electron energy of 1 keV. The solid black line is the energy distribution obtained with the original Kieft and Bosch models, the dashed red line is obtained with our refined models.

3.6 Comparison to experimental results

In order to determine how well the simulator predicts experimental results, we compare the yield curves obtained with our refined models for silicon, gold and alumina to yield curves collected by Joy [35]. In Figures 3.16 and 3.17 the comparison between simulated and experimental values for silicon

and gold are shown respectively. The solid lines are simulated values with our refined models, the dots are data points as found in [35]. For reference, the simulated yield curves with the original models of Kieft and Bosch are shown (dashed lines). Note that Joy collected these data points from different experimental sources. The yield curves for silicon are a collection of the yield curves found in [36–43] and those for gold can be found in [39–49].

Figure 3.16: Secondary electron and backscatter yields for silicon as simulated with our refined models (solid lines) compared to the yields as reported by Joy [35] (data points). For reference, the yield simulated with the original Kieft and Bosch models are shown (dashed lines).

From Figures 3.16 and 3.17, we see that the simulated yields overestimate the experimental values. The original models as used by Kieft and Bosch did better in predicting the experimental values. However, if we look at the experimental methods used to collect the yield curves, we see that for example in [39, 44, 45, 47] the yields were measured in a scanning electron microscope (SEM) in high vacuum. We know that the environment in a SEM can be called a 'dirty' environment. In this case, there will be contamination present on the samples when the yield curves are measured. This contamination can have a big effect on the yield. This makes it very difficult to evaluate which simulation gives the best results.
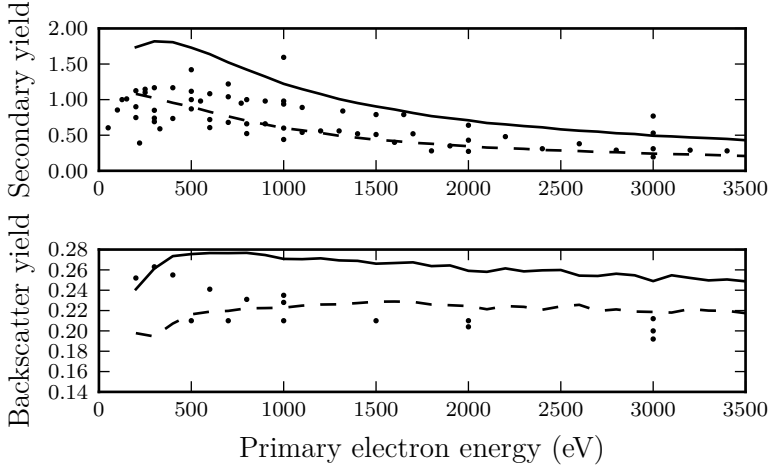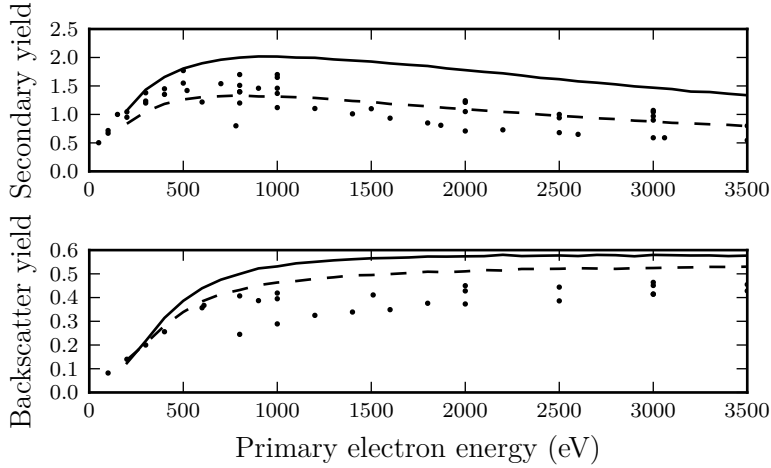
Figure 3.17: Secondary electron and backscatter yields for gold as simulated with our refined models (solid lines) compared to the yields as reported by Joy [35] (data points). For reference, the yield simulated with the original Kieft and Bosch models are shown (dashed lines).

For alumina, Joy only reports experimental data of the secondary electron yield of sintered alumina, polished sapphire, and unpolished sapphire. The experimental data were taken by Dawson [50]. Special care was taken to prevent charging by using single pulse methods [51] and the surfaces of the samples were treated to remove surface contaminations. The pressure was around 2×10^{-9} Torr during the experiments, so we do not have to worry about contamination of the sample surface. The comparison to these experimental data is shown in Figure 3.18. From this Figure it is already clear that the exact surface condition of the sample has a big effect on the secondary electron yield of said sample; the polished sapphire has a maximum secondary electron yield $\sim 25\%$ higher than the sintered alumina and the unpolished sapphire. The simulated values correspond very well with the experimental values for the sintered alumina and the unpolished sapphire. In comparison to the original models of Kieft and Bosch, our model refinements are a big improvement. When we look at the sintered alumina and the unpolished sapphire, the original models overestimated the secondary elec-

tron yield of alumina by a factor of ~ 4.3. For the exact secondary electron yield curve with the original Kieft and Bosch models, we refer to Figure 3.3. With our model refinements, the error is only 4 to 6%. The main reason our models do significantly better in predicting the secondary electron yield of alumina is the correction of the calculation of the surface potential barrier for insulators (and semiconductors).
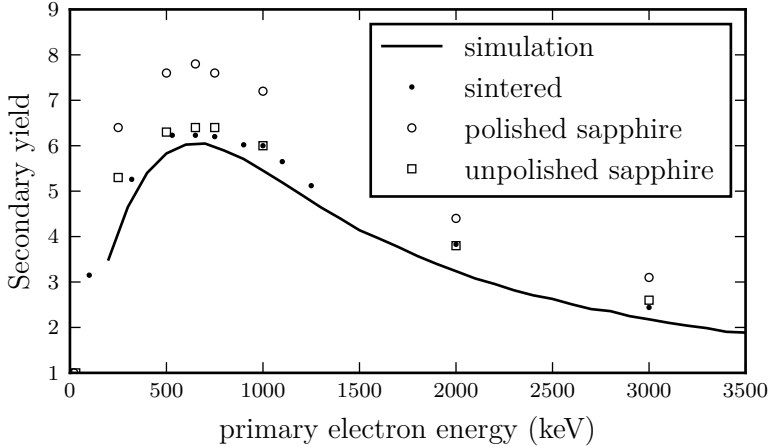
Figure 3.18: Secondary electron yield for alumina as simulated with our refined models (solid line) compared to the secondary electron yield as reported by Joy [35] (data points). Note that the trapping model was not used.

3.7   Surface contamination

In the previous section we have seen that it is not always clear what the state of the surface of a sample is during yield measurements. To investigate the effect of surface contamination, we have simulated the secondary electron yield curves of silicon and gold with surface contamination. For silicon we have looked at silicon dioxide and carbon as contamination. In air a silicon dioxide layer will form on top of a silicon sample, so we can safely assume a silicon dioxide layer will be present on an untreated silicon sample. In an SEM, the vacuum is such that there will still be enough carbohydrates present

that carbon contamination can grow on top of samples under irradiation of the electron beam. This is seen for example in [52–54]. The effect of carbon contamination on silicon is investigated by simulating a 1 nm layer of graphite on top of a silicon substrate. The resulting secondary electron yield curve is shown in Figure 3.19. Here we see that the secondary electron yield of the sample is decreased as a result of the graphite layer. The second form of contamination which could be present on a silicon sample is a natural silicon dioxide layer. If the sample is not cleaned well enough, this will affect the measured secondary electron yield. For silicon dioxide we have simulated the effect on the secondary electron yield of a 1 nm layer on top of a silicon sample. In Figure 3.19 we see an increase in the secondary electron yield. This was also seen in [55] for thin silicon dioxide layers on top of silicon.
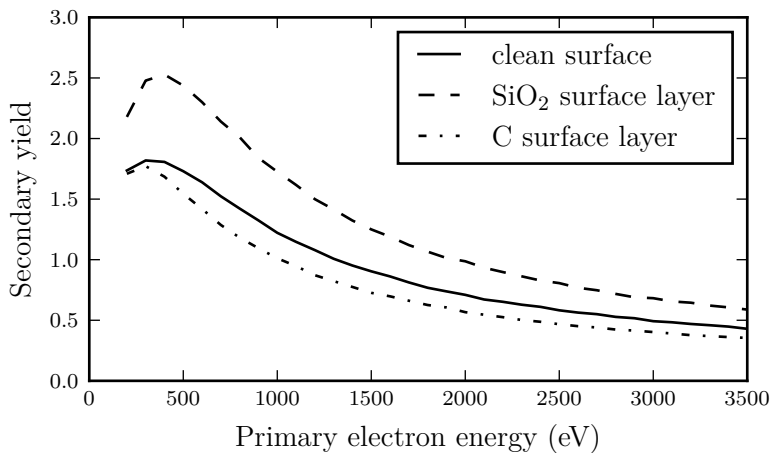
Figure 3.19: The effect of contamination on the secondary electron yield of silicon. The yield of a clean sample (solid line) is compared to a silicon dioxide contaminated sample (dashed line) and a graphite contaminated sample (dash-dotted line). In both cases the contamination is a 1 nm layer on top of the surface.

For gold we have simulated the effect of a 1 nm graphite contamination layer as well. The expected effect of this contamination layer is a decrease in the secondary electron yield. In Figure 3.20 we indeed see a decrease in

the secondary electron yield of about 25%.
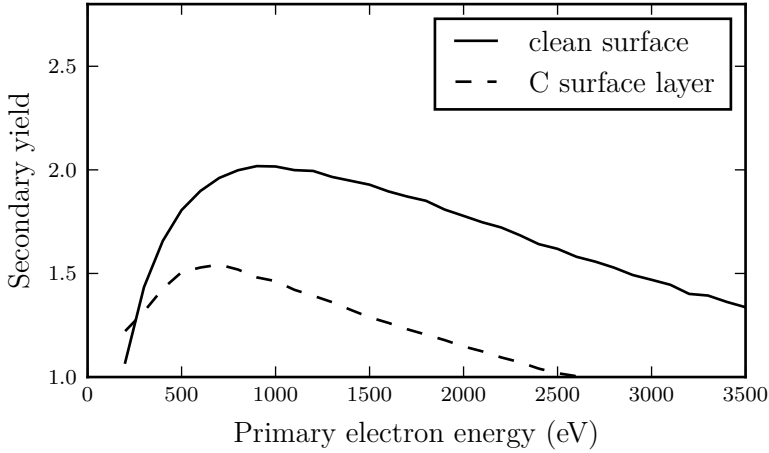
Figure 3.20: The effect of contamination on the secondary electron yield of gold. The yield of a clean sample (solid line) is compared to a graphite contaminated sample (dashed line). The contamination is modelled as a 1 nm layer on top of the surface.

The effect of a graphite contamination layer is much bigger for gold than for silicon, although the layer thickness is the same in both cases. If you only take the stopping power of the graphite contamination layer into account, you would expect the relative effect of the graphite contamination layer to be the same for silicon and gold. However, the graphite contamination layer also introduces a new boundary; the boundary between the substrate (silicon or gold) and graphite. To understand why this makes a difference, we will look at the potential barrier between silicon and graphite and that between gold and graphite. We will first calculate the potential barriers for the three materials with vacuum using Equations 2.65 and 2.66 and the material parameters as given in Appendix A. The resulting barriers are 10.91 eV for gold, 12.44 eV for silicon and 13.24 eV for graphite. For an electron going from silicon to graphite, this gives a barrier of $12.44 - 13.24 = -0.8$ eV. Using Equation 2.68, we get a probability to reflect internally of 0.01 % for an electron approaching the barrier between silicon and graphite along the

boundary normal with an energy of 10 eV above the vacuum level. An electron going from gold to graphite sees a barrier of $10.91 - 13.24 = -2.33$ eV. Again using Equation 2.68, we find that an electron approaching the barrier between gold and graphite along the boundary normal with an energy of 10 eV above the vacuum level has a probability of 0.11 % to be reflected internally. The probability to reflect internally is more than 10 times higher for a 10 eV electron in gold than it is in silicon. This explains why the graphite contamination layer has a much bigger effect on the secondary electron yield of gold than on that of silicon.

3.8   Conclusion

When we combine the effects of all the model refinements for silicon and gold, we see that the secondary electron yields increase when we go from the original Kieft and Bosch models to our models. For silicon, the maximum secondary electron yield increases from 1.1 to 1.8. For gold the maximum secondary electron yield increases from 1.3 to 2.0. For alumina, the combined effect of our model refinements is a decrease of the maximum secondary electron yield from 27.5 to 6.0 when we do not use the trapping process.

The removal of the surface absorption process and the correction of the calculation of the potential barrier height at the interface between the material and vacuum have the biggest effect on the secondary electron yield. For silicon and gold, the secondary electron yield is increased to unrealistic values by applying the refinements to the boundary crossing process. The combined effect of the other refinements is to decrease the secondary electron yields of silicon and gold again to more realistic values.

For alumina, the secondary electron yield as calculated with the original Kieft and Bosch models overestimated the experimental values by a factor of ~ 4.3. The effect of the boundary crossing refinements is to decrease the secondary electron yield maximum from 27.5 to 11.2. The combined effect of the elastic and inelastic scattering model refinements decreases the secondary electron yield for alumina even further to the more realistic value of 6.0. Note that charging is not taken into account in our models. When the

simulated secondary electron yield for insulators is compared to experimental values, one has to take care that there was no charging present during the experiment. If the experiments suffered from charging, the simulated yield values will overestimate the secondary electron yield for insulators when the yield is larger than 1. A trapping process could be used to simulate the effect of charging. We have seen that the trapping process indeed decreases the secondary electron yield. However, we will not use the trapping process in the rest of this research, because the trapping process is basically a fitting parameter and our goal is to develop a simulator without fitting parameters.

Compared to the original models, our refined models do slightly worse in reproducing experimental values for silicon and gold and better in reproducing experimental values for alumina. However, comparing to experimental values can be tricky because it is not always clear what the state of the sample surface was. In some cases, there could have been contamination present, which would affect the measured secondary electron yield. Overall we have removed some errors in the derivation of the models and their implementation and we were able to remove some phenomenological parameters.

Chapter 4

Transmission secondary electron yield of insulators

To realise the **Ti**med **P**hoton **C**ounter (TiPC), transmission dynodes, or tynodes, with a large enough transmission secondary electron yield are necessary. Preferably, the transmission secondary electron yield is larger than four. Similar as for the reflection secondary electron yield, we expect the transmission secondary electron yield to depend on the energy of the primary electrons hitting the top of the membrane. For very low energies, all primary electrons will be absorbed before reaching the bottom side of the membrane. Hence for very low energies, the total transmission electron yield will be zero. When the primary energy is increased, the range of the primary electrons will also increase. Eventually, the first 'primary' electrons will escape from the bottom side of the membrane. Note that these electrons will be measured as secondary electrons, because their energy will be smaller than 50 eV, probably in the 0 to 10 eV energy range. Increasing the energy further, will lead to more primary electrons being able to reach the bottom surface and more secondary electrons will be created near the bottom surface such that they can escape from the bottom side of the membrane. The transmission secondary electron yield will increase with the primary energy at first. However, at some point, the primary electrons will start to shoot through the membrane with still a considerable amount of energy left. This electron can then no

longer create secondary electrons and its excess energy is lost. Most secondary electrons are created at the end of a primary track, so the amount of secondary electrons created will start to decrease. Hence the transmission secondary electron yield will start to decrease with the primary energy. The primary energy where the transmission secondary electron yield reaches its maximum is the optimum primary energy for that specific membrane. The optimum primary energy depends on the material the membrane is made of. More specifically, materials with a higher stopping power will have a higher optimum primary energy. The optimum primary energy also depends on the membrane thickness; for a thicker membrane, the energy necessary to penetrate the membrane will shift to a higher energy. The optimum primary energy will equally shift to a higher energy with increasing membrane thickness.

The value of the transmission secondary electron yield depends on the energy as discussed above. However, it also depends on the membrane thickness. For very thin membranes, there is simply not enough material for the primary electrons to create many secondary electrons. This is the case when the membrane thickness is smaller than the escape length of the secondary electrons. Increasing the membrane thickness will increase the maximum transmission secondary electron yield[1] for these very thin membranes, because more secondary electrons will be created within the escape length. However, if the membrane thickness is increased after a certain optimum membrane thickness, the maximum transmission secondary electron yield will decrease again. In this case, the primary electrons lose too much energy in the top part of the membrane and most secondary electrons are created further away from the bottom surface than their escape length. These secondary electrons are not able to reach the bottom surface of the membrane in order to escape in transmission mode. Note that these electrons might still be able to escape through the top surface to contribute to the reflection secondary electron yield. To gain insight in the dependences of the trans-

---

[1]In literature 'maximum yield' is quite often denoted simply as 'yield'. We will not use this shorthand, as here the word 'yield' should be read as the whole yield curve and not only its maximum.

mission secondary electron yield, we will discuss Monte Carlo simulations of alumina membranes, where the dependence on primary energy and the membrane thickness is investigated.

4.1 Simulation geometry

In the simulations, the top of a membrane is irradiated with primary electrons. All electrons emitted from the top of the membrane are detected by an ideal reflection detector, positioned just above the membrane and all electrons emitted from the bottom of the membrane are detected by an ideal transmission detector, positioned just below the membrane. The geometry of the membrane and detector setup used in the simulation is shown in Figure 4.1. In the simulation all primary and secondary electrons are tracked
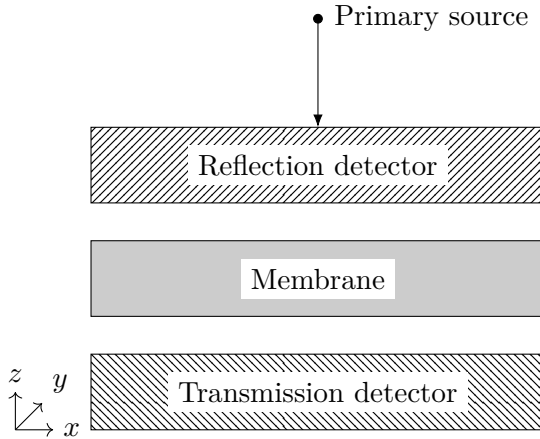
Figure 4.1: The geometry setup of the membranes and detectors in the Monte Carlo simulations. The reflection detector is completely transparent for the primary electrons, but all backscattered and secondary electrons that hit the reflection detector are detected with a 100% efficiency. The transmission detector also has a 100% efficiency

to their final state. There are three different final states: the electron is emitted on the reflection side (the top) of the membrane and detected by the reflection detector (1), the electron is emitted on the transmission side

(the bottom) of the membrane and detected by the transmission detector
(2), or the electron loses all its energy in the membrane and is absorbed
(3). The primary electron beam hits the membrane on the top exactly in the
centre with respect to the x- and y-directions as indicated in Figure 4.1. The
simulated membrane has a radius of 1 mm and can be regarded as infinite
in the x- and y-directions for electrons with energies at least up to 10 keV
hitting the exact centre of the membrane. Hence, no electrons will escape
the membrane from the side and all emitted electrons are detected by either
the reflection or the transmission detector. All simulation results below are
obtained with 100,000 primary electrons, unless stated otherwise.

4.2   Secondary electron creation points

The escape probability of a secondary electron depends on the position where
the secondary electron is created. The further the electron is created from
a surface, the lower the probability of escape through this surface. The
decrease of the escape probability with distance to the surface is expected
to be exponential. A simulation was run where the creation points of all
electrons were saved. In Figure 4.2 b) the simulated distribution of creation
points of secondary electrons in a 25 nm membrane is shown for 30 primary
electrons of 2200 eV hitting the alumina membrane. Every electron was
tracked until it was either emitted by the top or bottom surface or until it
was absorbed in the membrane. Note that the electrons could still undergo
elastic and inelastic scattering events before being emitted (or absorbed).
Figure 4.2 shows that electrons emitted by the reflection surface are mostly
created in the top part of the membrane and that electrons emitted by the
transmission surface are mostly created in the bottom part of the membrane.
Figures 4.2 a) and c) show the depth distribution of the creation points for
the cases (1) and (2) respectively. Most of the escaped electrons originate
from the ~ 10 nm surface layer. Fitting an exponential function in the form
of

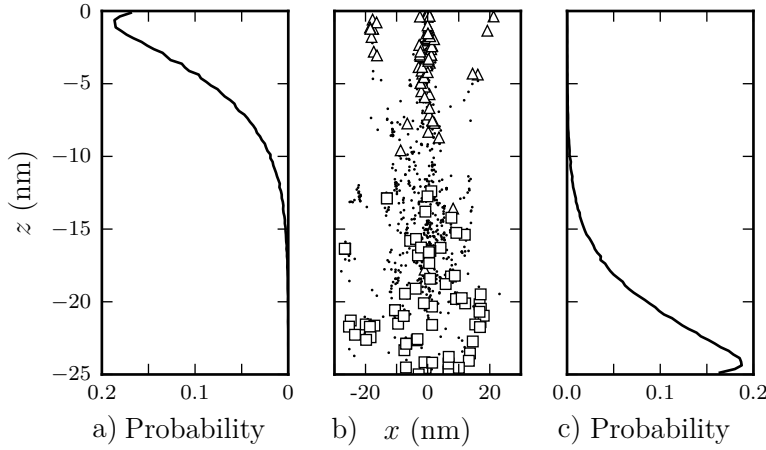$$P = A \cdot e^{-z/\lambda_{esc}} \tag{4.1}$$

Figure 4.2: Simulation of a 25 nm alumina membrane, bombarded with 2200 eV electrons. The probability density function of the creation depth for electrons that leave the membrane on the top side (resp. bottom side) is shown in **a)** (resp. **c)**). Note that the probability density function is normalised with a bin width of 0.25 nm. **b)** All points where electrons are created during a simulation with 30 primary electrons are shown. The triangles and squares denote creation points of electrons that were able to escape on the reflection and transmission side respectively. The dots denote creation points of absorbed electrons. z is defined as the depth with respect to the irradiated surface. x is the distance to the beam position projected on the x-axis. Both axes are as defined in Figure 4.1.

will give the creation escape length λ_{esc}, defined as the shortest distance between the surface an electron escapes from and the creation point of this electron. Note that this is not the same as the traditional escape length, which is usually defined as the depth from which electrons can escape without undergoing any interaction with the material. The fit for the creation escape length in reflection gives $\lambda_{esc} = 3.96$ nm and in transmission $\lambda_{esc} = 3.93$ nm. By integrating this fit it can be determined that in reflection mode as well as in transmission mode 90% of the emitted electrons originates from the 8 nm surface layer closest to the emitting surface of the membrane.

4.3   Simulated yield curves

The transmission and reflection yield of a membrane depend on the energy
of the primary electrons hitting the membrane, as previously discussed. In
Figure 4.3 the simulated yield curves for a 10 nm alumina membrane are
shown. When we compare the backscatter yields, we see that the reflection
backscatter electrons are present for very low energies. In fact, we expect
the reflection backscatter yield to be non-zero for energies higher than 50 eV,
since some primary electrons will always be reflected immediately. However,
the transmission backscatter yield only emerges for energies higher than 600
eV. For lower energies, the primary electrons do not have enough energy to
travel through the membrane and escape on the other side with more than 50
eV. First, the primary electrons have to have enough energy to travel through
the membrane and escape the bottom side. Second, these primary electrons
also need more than 50 eV when they escape to be counted as backscatter
electrons. So it makes sense that there are no transmission backscatter elec-
trons at lower primary energies. From Figure 4.3, it is clear that the optimum
primary energy for the transmission secondary electron yield is higher than
the optimum energy for the reflection secondary electron yield. This can be
explained by the fact that a primary electron hitting the membrane will im-
mediately start to generate secondary electrons. These secondary electrons
can easily contribute to the reflection yield, because they are created close
to the top surface and will have a high probability to escape through the top
surface. However, for most membrane thicknesses, these electrons have a low
probability to contribute to the transmission yield, because they first have
to travel through the membrane in order to reach the bottom surface. If the
energy is increased, the primary electrons travel deeper into the membrane
and the probability to escape through the top surface decreases. However,
at the same time, the probability to escape through the bottom surface in-
creases. This results in a higher energy necessary to reach the maximum
transmission secondary electron yield with respect to the energy necessary
to obtain the maximum reflection secondary electron yield.

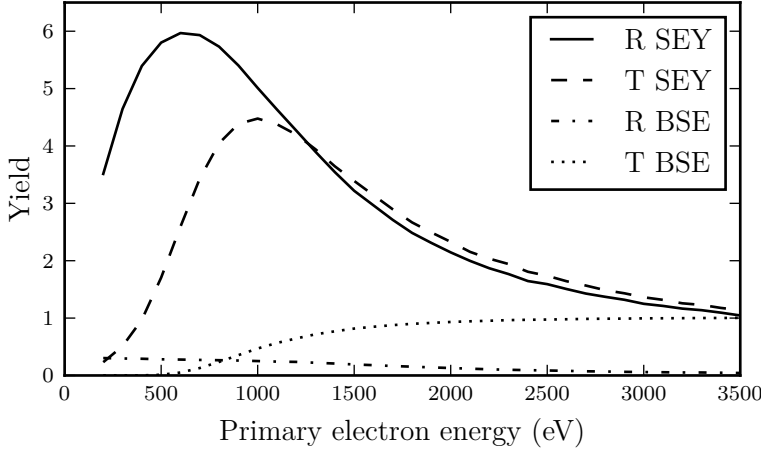We also see in Figure 4.3 that the maximum transmission secondary

Figure 4.3: The simulated yield curves for a 10 nm alumina membrane. The maximum reflection secondary electron yield (R SEY, solid line) is higher than the maximum transmission secondary electron yield (T SEY, dashed line) and has a lower optimum energy. The reflection backscatter electrons (R BSE, dash-dotted line) are already present at very low energies. The transmission backscatter electrons (T BSE, dotted line) only start to escape from the membrane at a primary energy of 600 eV.

electron yield is lower than the maximum reflection secondary electron yield. This holds for all simulated membrane thicknesses as can be seen in Table 4.1. To understand why this is the case, we look at the distribution of the creation points of secondary electrons in a 25 nm membrane at the primary energies where the reflection and the transmission secondary electron yield are at their respective maxima. At 700 eV, the reflection secondary electron yield reaches its maximum for a 25 nm membrane. In Figure 4.4 the distribution of the secondary electron creation points at 700 eV is shown. Figure 4.2 is made at 2200 eV, the optimum energy for the transmission secondary electron yield for a 25 nm membrane. In Figure 4.4 b), we see that the electron cloud is positioned very close to the top surface when the reflection secondary electron yield reaches its maximum. Almost all energy of the primary electron is transferred to secondary electrons that can contribute to the reflection yield. However, in Figure 4.2 b) when the transmission sec-

thickness (nm)	max. reflection yield	max. transmission yield
8	5.78	4.55
10	5.97	4.48
25	6.02	2.96
50	6.02	1.98

Table 4.1: The maximum reflection and transmission secondary electron yield for alumina membranes of different thicknesses. The maximum reflection secondary electron yield is always higher than the maximum transmission secondary electron yield.

ondary electron yield reaches its maximum, we see that a lot of energy of the primary electrons is already lost to secondary electrons that contribute to the reflection yield. We also see that at 700 eV, the probability distribution of creation points of electrons that contribute to the reflection yield is shifted more towards the top surface than at 2200 eV. In other words, at 700 eV the energy is so low that 90% of the reflection secondary electrons are created within the ~ 5 nm surface layer instead of the 8 nm surface layer at 2200 eV. The secondary electrons created in the 5 nm surface layer have of course a larger probability to escape than the electrons created in between 5 and 8 nm from the surface. Hence the efficiency of creating secondary electrons to add to the reflection yield is higher at 700 eV than at 2200 eV. In transmission mode, we simply never reach the case where 90% of the transmission secondary electrons originate from the ~ 5 nm bottom layer of the membrane. When we increase the primary energy from 2200 eV to higher energies, the effect is that we start to lose potential energy to create secondary electrons, because primary electrons start to shoot through the membrane instead of converting all their energy to secondary electrons that might contribute to the transmission secondary electron yield.

The maximum reflection secondary electron yield depends on the membrane thickness for very thin membranes, as can be seen in Table 4.1, where the maximum reflection secondary electron yield for an 8 nm membrane is lower than the maximum reflection secondary electron yield for bulk. For very thin membranes, there is not enough material to create many second-
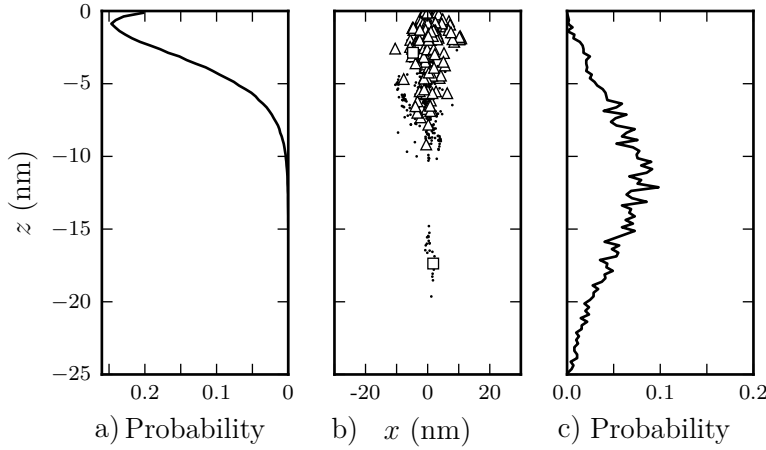
Figure 4.4: Simulation of a 25 nm alumina membrane, bombarded with 700 eV electrons. 700 eV is the optimum primary energy for the reflection secondary electron yield. The probability density function of the creation depth for electrons that leave the membrane on the top side (resp. bottom side) is shown in **a)** (resp. **c)**). Note that the probability density function is normalised with a bin width of 0.25 nm. **b)** All points where electrons are created during a simulation with 30 primary electrons are shown. The triangles and squares denote creation points of electrons that were able to escape on the reflection and transmission side respectively. The dots denote creation points of absorbed electrons. z is defined as the depth with respect to the irradiated surface. x is the distance to the beam position projected on the x-axis. Both axes are as defined in Figure 4.1.

ary electrons. If we bombard these thin membranes with electrons with the same primary energy that gives the maximum reflection secondary electron yield for a bulk sample, some secondary (and primary) electrons will already be emitted on the transmission side and will not contribute to the reflection yield. Thus the maximum bulk reflection secondary electron yield will never be obtained with these very thin membranes. Increasing the membrane thickness, will result in less secondary electrons 'lost' to transmission at the energy necessary to obtain the maximum reflection secondary electron yield. The maximum reflection secondary electron yield for thin membranes keeps increasing with thickness, until the maximum is equal to the maximum re-

flection secondary electron yield of bulk. This happens at a thickness where no electrons are emitted in transmission mode when the primary energy is the optimum primary energy for the reflection secondary electron yield of bulk samples.

The maximum transmission secondary electron yield will also depend on membrane thickness. For very thin membranes (not included in Table 4.1), the maximum transmission secondary electron yield will increase with increasing membrane thickness. In these thin membranes, there is simply not enough material for the primary electrons to generate many secondary electrons, similarly as for the reflection yield. However, if we keep increasing the membrane thickness, at some point we expect that the maximum transmission secondary electron yield will start to decrease with increasing membrane thickness. For these thicker membranes, the primary electrons and the created secondary electrons have to travel through more material before they can contribute to the transmission yield and more electrons are absorbed in the material. In between these two extreme cases, the maximum transmission secondary electron yield will reach a maximum for the optimum membrane thickness. In Figure 4.5 the maximum transmission secondary electron yield dependence on the membrane thickness is shown. For alumina, the optimum membrane thickness is found to be 8 nm.

4.4   Angle of incidence

From experimental results we know the maximum reflection secondary electron yield can be increased by tilting the sample such that the primary electron beam hits the surface at an angle [56]. For a 25 nm alumina membrane, we expect the same result for the maximum reflection yield as for bulk, the maximum secondary electron yield should increase with the angle of incidence. In Figure 4.6 we indeed see the maximum reflection secondary electron yield increases with the angle of incidence. Here the angle of incidence is defined as the angle between the surface normal and the primary electron beam.

We can understand this, because by increasing the angle of incidence,
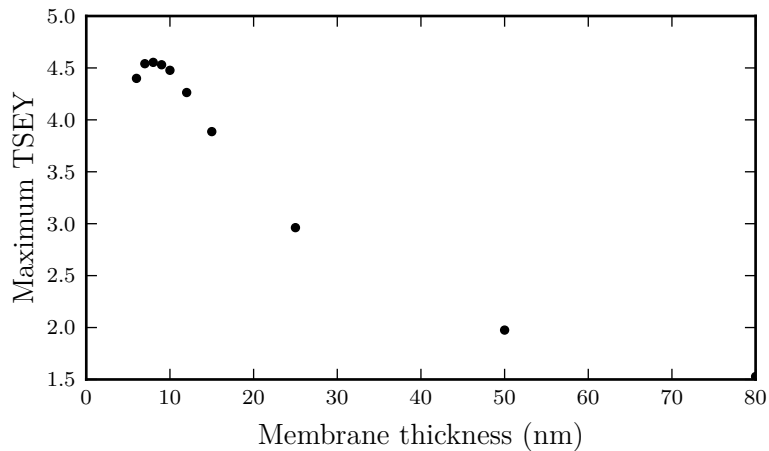
Figure 4.5: The maximum transmission secondary electron yield (TSEY) for alumina membranes depending on the membrane thickness. The maximum transmission secondary electron yield reaches its maximum value for an 8 nm membrane.
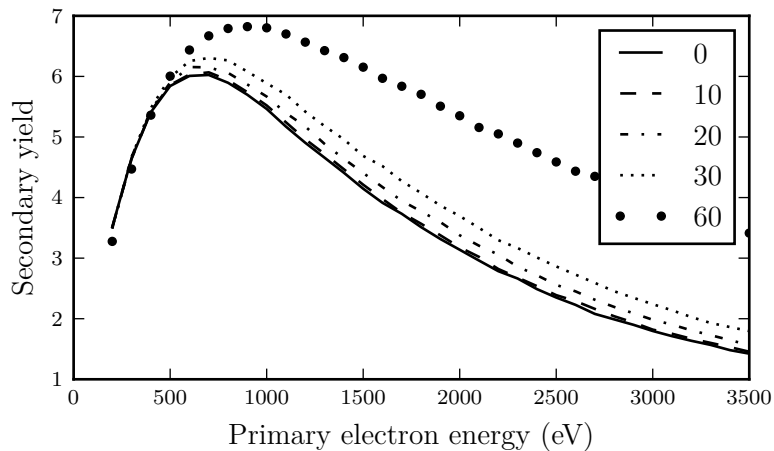

Figure 4.6: The reflection secondary electron yield for a 25 nm alumina membrane depending on the angle of the incident beam with the surface normal.

we increase the part of the track of the primary electrons that is close to the surface. This means more secondary electrons are created close enough to the surface to escape and contribute to the reflection secondary electron yield. However, for the maximum transmission secondary electron yield, we would expect a different dependence on the angle of incidence. In this case, by tilting the sample, we effectively make the membrane thicker. This means that for a 25 nm membrane, we expect the maximum transmission secondary electron yield to decrease with the angle of incidence. In Figure 4.7 we indeed see the maximum transmission secondary electron yield decreases with the angle of incidence.
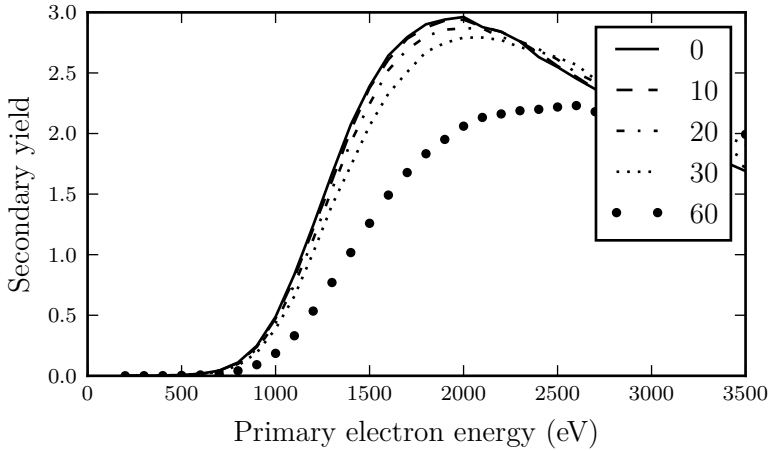
Figure 4.7: The transmission secondary electron yield for a 25 nm alumina membrane depending on the angle of the incident beam with the surface normal.

In both cases, we expect the optimum primary energy to shift to higher energies. In the case of the reflection secondary electron yield, a slightly higher primary energy creates more secondary electrons. At 0° degrees, this higher primary energy also leads to more secondary electrons created, but they are created too far from the surface to escape. By increasing the angle, at least some of these electrons are now close enough to the surface to escape. In the case of the transmission secondary electron yield, the shift can simply

be explained by the fact that an increase in the angle of incidence effectively makes the membrane thicker. For thicker membranes the optimum primary energy is higher, so increasing the angle of incidence increases the optimum primary energy. Indeed, in both Figures 4.6 and 4.7 we see the optimum primary energy increases with the angle of incidence.

4.5   Experimental yield curves

In order to compare the simulations to experimental values, alumina membranes were fabricated and their transmission yields were measured in a SEM by Prodanović and Chan [6]. In Figure 4.8 the transmission yields for 5 nm, 10 nm, 25 nm and 50 nm alumina membranes are shown. The maximum total transmission electron yield shows the same trends as predicted by Figure 4.5, the maximum total transmission electron yield increases for very thin membranes until a maximum is reached. Increasing the thickness even further leads to a decrease in the maximum total transmission electron yield. We also see that the optimum primary energy increases when the membrane thickness is increased. In the experimental results, the total transmission yield exceeds 0.1 at 950 eV for a 25 nm membrane and at 1550 eV for a 50 nm membrane. For a 25 nm membrane, the simulation predicted that the total transmission yield first exceeds 0.1 at a primary energy of around 800 eV, we see now that this energy is a slight underestimation. For a 50 nm membrane the simulation predicted the total transmission yield would first exceed 0.1 between 1500 eV and 1600 eV, which corresponds to the experimental value.

The absolute value of the total transmission yield is overestimated by the simulations. However, in the simulations, charging is not taken into account. Alumina as an insulator is expected to suffer from charging during experiments where it is subjected to electron irradiation. To overcome charging effects, the prototype tynodes are coated with a 2-5 nm conducting layer. In the experiments, the samples were coated with a 5 nm titanium nitride layer. However, we do not have the necessary material parameters of titanium nitride to run a simulation. The final tynodes will probably have a chromium
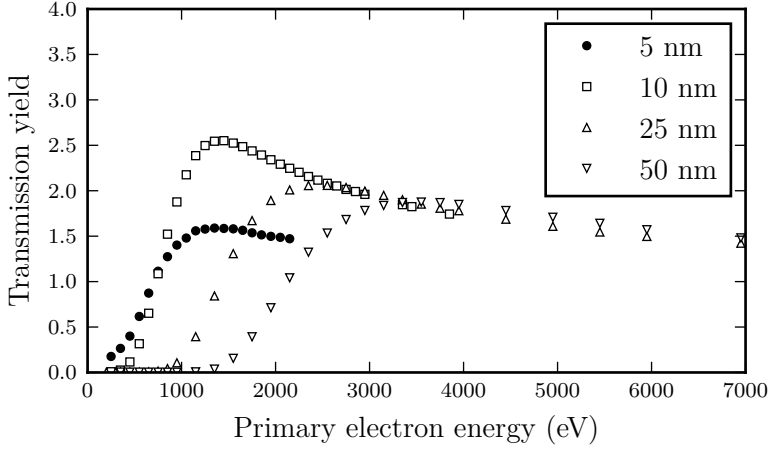
Figure 4.8: The experimental total transmission electron yield curves for alumina membranes of varying thickness.

coating, so here we have investigated the effect of a chromium coating. The simulation results for 25 nm alumina membranes, with and without a 5 nm chromium coating are compared to the experimental results for an alumina membrane with a 5 nm titanium nitride coating in Figure 4.9. Note that the simulation of the clean alumina membrane is for a 25 nm alumina membrane. The total thickness of the coated alumina membranes was 30 nm (25 nm alumina + 5 nm coating) in both the simulations and the experiments and in both cases the coating was put on the top (reflection side) of the sample. The simulated maximum total transmission yield for a chromium coated sample decreases with respect to the simulated maximum total transmission yield for a clean surface. In reflection mode, it was already known that this decrease is quite significant, the simulated maximum total reflection yield decreases from 6.3 to 2.2 for a 2.5 nm chromium coating and to 2.1 for a 5 nm coating. Increasing the layer thickness, will at some point lead to a reflection yield equal to that of bulk chromium. However, in transmission mode the metal coating has a smaller effect on the yield. The maximum total transmission yield does decrease, but it only decreases from 3.5 for a clean sample to 3.2 for a 2.5 nm chromium coating and to 3.0 for a 5 nm chromium coating. We

expect a 5 nm chromium coating (on the reflection side) to have a smaller effect on the transmission yield of a 50 nm membrane. In fact the simulated maximum transmission yield for a 50 nm membrane decreases from 2.6 for a clean surface to 2.4 for a 5 nm chromium coating.

The energy for the maximum total transmission electron yield increases for increasing coating thickness, this would result in a higher voltage between the tynodes. Before we saw that the energy where the transmission yield first exceeds 0.1 was somewhat underestimated for a 25 nm membrane, which makes sense, because we were comparing a non-coated sample (simulation) with a coated sample (experiment). For the 50 nm membrane, the prediction was more accurate. We can understand this by realising that 5 nm of extra material for a 25 nm membrane is an increase in thickness of 20%, while for a 50 nm membrane, 5 nm extra is an increase of 10%.
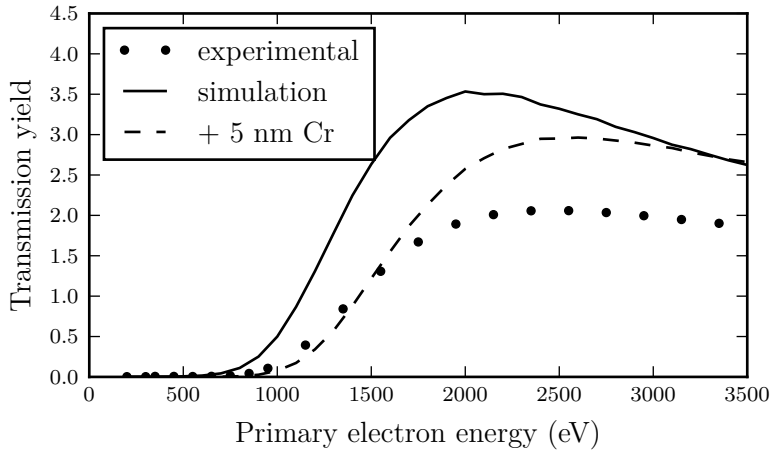

Figure 4.9: The total transmission yield for an alumina membrane. The solid line is a simulation of a 25 nm membrane with a clean surface, the dashed line is a simulation of a 25 nm membrane with a 5 nm chromium coating (30 nm total) and the dots are experimental results for a 25 nm membrane with a 5 nm titanium nitride coating (30 nm total).

4.6   Conclusion

The simulations of the transmission and reflection yield of thin membranes can help to understand the difference between the reflection and transmission yield. In a simulation, it is possible to keep track of every single electron and obtain information about the shape of the electron cloud and the creation escape length, i.e. the probability to escape for an electron created at a certain distance from the surface.

With the use of simulations, the optimum membrane thickness for a specific material can be determined. For alumina, the optimum membrane thickness was found to be 8 nm.

In order to prevent charging effects, the tynodes should be coated with a thin conducting layer. This conducting layer will increase the voltage necessary to obtain the maximum total transmission electron yield, and it will decrease the maximum total transmission electron yield. This decrease will however be less dramatic than the decrease of the reflection yield for a coated sample.

Chapter 5

Secondary electron emission properties of silicon rich silicon nitride

In the previous chapter we have briefly discussed the possibility of coating an insulator with a thin conducting layer in order to prevent charging effects during electron irradiation and the emission of (secondary) electrons. Another solution to the charging problem would be adding a dopant to the material to make the material slightly conductive. An example of this is boron doping in diamond [57]. However we could not find a supplier of diamond membranes that were thin enough to be used as tynodes. A material of which we can make thin membranes and to which we can add a dopant is silicon nitride [5,6]. In this chapter we discuss the effect of silicon doping in silicon nitride on its secondary electron emission properties. First we will start with the determination of the necessary material parameters.

5.1   Material parameters

We have investigated the effect of two doping levels of silicon in silicon rich silicon nitride: Si_7N_7 and $Si_{13}N_{15}$ and we compared the results to pure silicon nitride, Si_3N_4. For Si_7N_7 we have also investigated the effect of the

distribution of the extra silicon atoms in the material; we have looked at Si_7N_7 where the extra silicon atoms are distributed homogeneously over the material, where the extra silicon atoms are clustered together and we have looked at amorphous Si_7N_7. We have also looked at contaminated silicon rich silicon nitride. Silicon nitride membranes are fabricated with an LP-CVD process using dichlorosilane (SiH_2Cl_2) and ammonia (NH_3) [6]. During this process, it is possible that some of the hydrogen is trapped inside the fabricated membrane, so the contamination we have investigated is hydrogen contamination in the bulk of Si_7N_7. Now there are three different bonding options for the hydrogen atoms that we have investigated. The first is $Si_7N_7H^{Si}$ where there is one hydrogen atom bonded to one silicon atom for every seven silicon atoms, the second is $Si_7N_7H^{N}$ which is the same but now the hydrogen atoms are bonded to nitrogen atoms, and the third option is $Si_7N_7H_2^{Si,N}$ where there is one hydrogen atom bonded to one silicon atom for every seven silicon atoms and one hydrogen bonded to one nitrogen atom for every seven nitrogen atoms, in this case there are twice as many hydrogen atoms present as in option one and two.

In summary, we investigated eight different forms of (silicon rich) silicon nitride: Si_3N_4, $Si_{13}N_{15}$, homogeneous Si_7N_7, clustered Si_7N_7, amorphous Si_7N_7, $Si_7N_7H^{Si}$, $Si_7N_7H^{N}$ and $Si_7N_7H_2^{Si,N}$. What we expect to see is that lattice defects are introduced when we introduce extra silicon atoms in pure silicon nitride to obtain silicon rich silicon nitride. These lattice defects are effectively dangling silicon bonds of the extra silicon atoms. Now it is interesting to see what the effect of the different forms of (silicon rich) silicon nitride is on these dangling bonds and their effect on the secondary electron yield.

However, first we need to find the material parameters. Most material parameters were very straight forward to find and can be found in appendix A. However, some material parameters were more difficult to obtain and deserve a few words of explanation.

5.1.1   Energy loss function

One of the more difficult parameters to obtain is the dielectric function. Typically, optical data from 0 up to the primary electron energy are needed. Then with the use of equations 2.56 and 2.57, the energy loss function can be calculated. Instead of fabricating multiple samples with different doping levels and measuring the optical data in the appropriate energy range, it is possible to calculate the dielectric function. In fact, Tao has calculated the dielectric function of silicon rich silicon nitride with different levels of silicon doping by the use of *ab initio* density functional theory calculations [58]. Here we will use these calculated dielectric functions. Amorphous Si_7N_7 is not discussed in [58]. In this case we received the dielectric function through private communications.

5.1.2   Band gap

Tao did not only calculate the dielectric function for the different doping levels and structures of silicon rich silicon nitride; she also calculated the density of states [58]. From the density of states we can read the approximate band gap for the exact doping levels and structures we are interested in. For amorphous Si_7N_7 the density of states is missing. In this case we read out the band gap from the energy loss function.

5.1.3   Acoustic deformation potential

The last material parameter we want to discuss here is the acoustic deformation potential. This is a very difficult parameter to find and for many materials it is not known. In fact, we were not able to find a value for the acoustic deformation potential of silicon nitride. For materials for which we did find a value, the acoustic deformation potential typically lies between 2 and 15 eV [59]. We could estimate a value for the acoustic deformation potential somewhere in this range. The question now is, how important is it to have an accurate value for the acoustic deformation potential? To answer this question, we have simulated reflection secondary electron yield curves for pure silicon nitride changing the value of the acoustic deformation po-

tential, using the approximation to the dual branch phonon model. Some of
the resulting yield curves are shown in Figure 5.1. For these curves we used
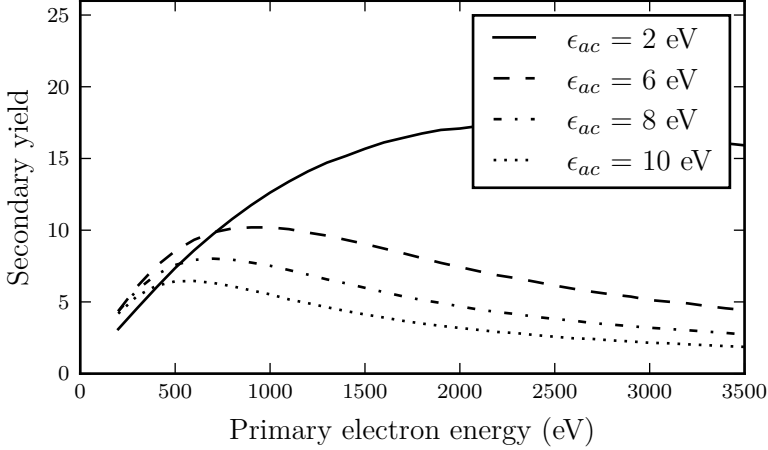the energy loss function calculated from optical data collected by Palik [60].

Figure 5.1: The reflection secondary electron yield of silicon nitride for different values of the acoustic deformation potential ϵ_{ac}.

The acoustic deformation potential has a very big influence on the secondary electron yield. This means we have to know the acoustic deformation potential accurately in order to be able to predict the secondary electron yield quantitatively.

Upon further inspection of the secondary yield curves for different values of the acoustic deformation potential, we see the yield maximum and optimum primary energy decrease with increasing acoustic deformation potential. In Figures 5.2 and 5.3 this dependence is shown in more detail. Both the yield maximum and the optimum primary energy could be used to fit the acoustic deformation potential, if reliable experimental data of the secondary electron yield of, for example, pure, silicon nitride were available.

Now, we could choose a value for the acoustic deformation potential for silicon nitride, for example $\epsilon_{ac} = 12$ eV, and evaluate the data qualitatively. However, the question that then arises is: can we use the same value for the acoustic deformation potential of Si_7N_7 and $Si_{13}N_{15}$? In order to answer
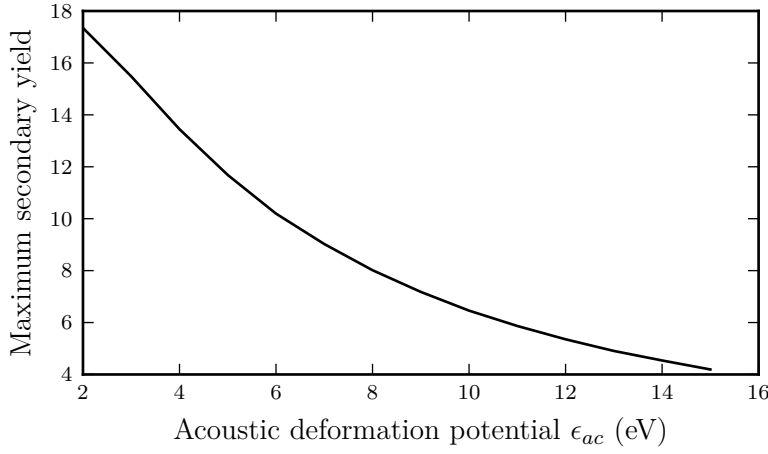
Figure 5.2: The maximum reflection secondary electron yield of silicon nitride for different values of the acoustic deformation potential ϵ_{ac}.

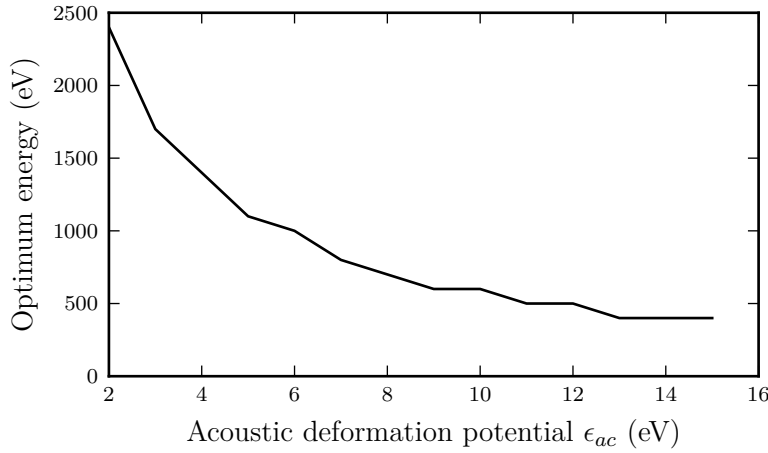

Figure 5.3: The optimum primary electron energy for silicon nitride for different values of the acoustic deformation potential ϵ_{ac}.

this question, let us first look at the definition of the acoustic deformation

potential ϵ_{ac} according to [59, 61]

$$\delta E_c = \epsilon_{ac} \frac{\delta V}{V}, \qquad (5.1)$$

where δE_c is the absolute energy shift of the conduction band minimum for a small uniform expansion δV of the crystal. When we look at the density of states for the different doping levels in [58] we conclude that the effect of the extra silicon atoms on the band structure is to introduce defect states. However, the general shape of the band structure is not affected. Since this is the case, we do not expect δE_c to change significantly when we introduce the extra silicon atoms. Hence we expect we can use the same value for the acoustic deformation potential for the different forms of (silicon rich) silicon nitride. Tekippe [62] investigated the effect of different kinds of dopant in silicon on the acoustic deformation potential and he found that the acoustic deformation potential did indeed not depend on the kind of dopant. We conclude that we can choose a single value for the acoustic deformation potential for the different forms of (silicon rich) silicon nitride and compare the results qualitatively.

5.2   Simulated secondary electron yield

Here we will discuss the simulation results of the secondary electron yield curves for the different forms of (silicon rich) silicon nitride. All the simulated yields are reflection yields of bulk material, where the incident angle is 0° degrees. All material parameters can be found in appendix A.

5.2.1   Pure silicon nitride

Before we can say anything about the secondary electron yield for the different forms of (silicon rich) silicon nitride, we have to investigate the quality of the calculated energy loss function. There exists a dataset with optical data for multiple materials, collected by Palik [60]. Optical data for pure silicon nitride is also present in this dataset, from this optical data we can calculate the 'experimental' energy loss function with equations 2.56 and 2.57. In Fig-
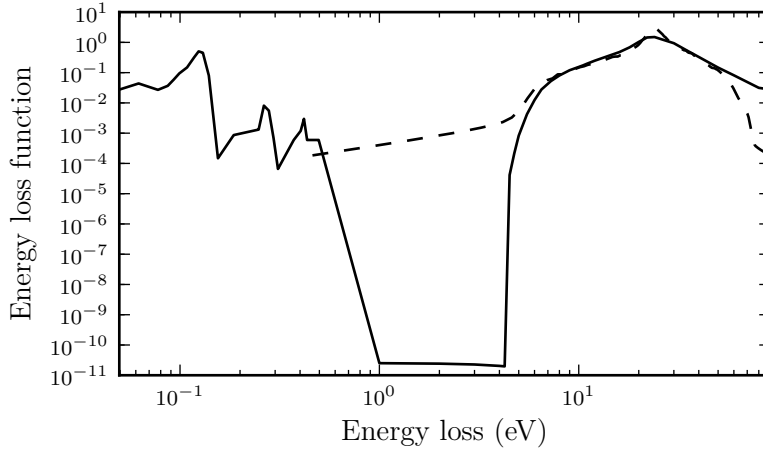
Figure 5.4: The calculated energy loss function for pure silicon nitride (dashed-line). For comparison, the energy loss function calculated with experimental optical data from [60] is shown (solid line).

ure 5.4, we compare the experimental and calculated energy loss function. Both energy loss functions show the bulk energy loss peak around 24 eV and the general shape of the bulk energy loss peak is reproduced well. Below 4.7 eV, the calculated energy loss function deviates from the experimental energy loss function. The experimental energy loss function is very small in between 1 eV and 4.7 eV, due to the band gap in silicon nitride. For very low energies, the experimental energy loss function shows energy loss peaks due to optical phonons. The calculated energy loss function does not include the optical phonons and it does not decrease as much as the experimental energy loss function for energies inside the band gap, although it does decrease to the low $10^{-4} - 10^{-3}$ range.

We have calculated the secondary electron yield curves for pure silicon nitride with both the experimental and the simulated energy loss function. The resulting yield curves are shown in Figure 5.5. The maximum secondary electron yield decreases from 5.4 at 500 eV for the experimental energy loss function to 5.0 at 450 eV for the calculated energy loss function. This is a decrease of 8 %. Typically the spread in experimental secondary electron

yield data is more than 8 % and we do not want to use the results quantit-
atively, but only qualitatively. We conclude that we can use the calculated
energy loss functions to investigate the effect the different forms of silicon
rich silicon nitride have on the secondary electron yield.
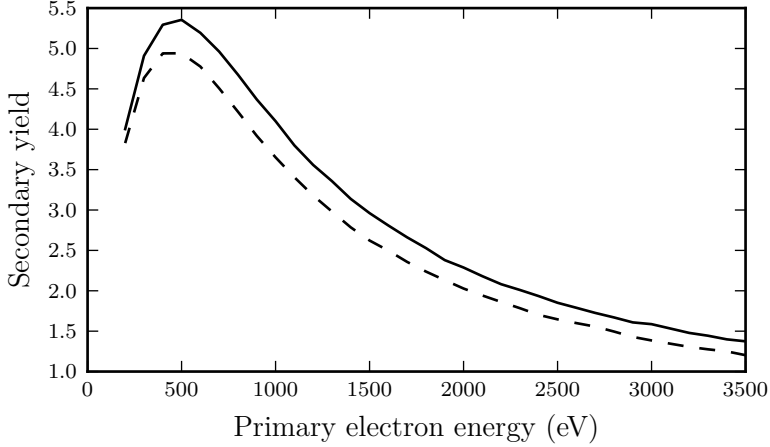

Figure 5.5: The reflection secondary electron yield for pure silicon nitride
with the experimental (solid line) and the calculated (dashed line) energy
loss function.

5.2.2   Doping level

In silicon rich silicon nitride, there are extra silicon atoms present compared
to pure silicon nitride. These extra silicon atoms will introduce lattice defects
in the form of dangling bonds. Electrons travelling in the material can scatter
at these defects and lose energy. We expect to see this in the energy loss
function in the form of extra energy loss peaks. In Figure 5.6 the calculated
energy loss functions for pure silicon nitride (Si_3N_4), $Si_{13}N_{15}$ and Si_7N_7 are
shown. The extra silicon atoms are distributed homogeneously over the
material for both $Si_{13}N_{15}$ and Si_7N_7. We see extra energy loss peaks in the
energy loss function for silicon rich silicon nitride compared to pure silicon
nitride, as we expected. The energy loss function for $Si_{13}N_{15}$ shows extra
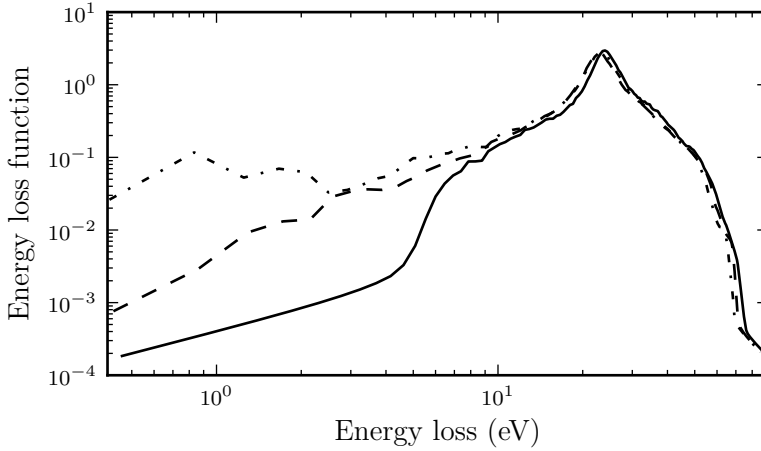peaks around 1.5 eV and 3.0 eV. Introducing even more silicon atoms results

Figure 5.6: The calculated energy loss functions for Si_3N_4 (solid line), $Si_{13}N_{15}$ (dashed line) and Si_7N_7 (dash-dotted line).

in loss peaks around 0.8 eV, 1.7 eV and 5 eV for Si_7N_7. Note that below 10 eV, the energy loss function increases overall for increasing doping level.

Due to the overall increase and the extra energy loss peaks below 10 eV, we expect the secondary electron yield to decrease with increasing doping level. Intuitively, we can understand this by remembering that the extra silicon atoms in the material introduce dangling bonds. These dangling bonds form extra potential inelastic scattering points for (secondary) electrons travelling in the material. Indeed, in Figure 5.7, we see that the secondary electron yield decreases with increasing doping level. When we go from Si_3N_4 to $Si_{13}N_{15}$ the maximum secondary electron yield decreases from 5.0 at 450 eV to 3.3 at 350 eV, a decrease of 34 %. When we increase the doping level even more to get Si_7N_7, the maximum secondary electron yield decreases further to 2.7 at 350 eV, a total decrease of 46 %.

Although the secondary electron yield decreases with increasing doping level, it might still be beneficial to have at least some silicon doping in samples used for experiments. During experiments, special precautions need to be taken to prevent the samples from charging up. The silicon doping in silicon rich silicon nitride makes the material slightly more conductive than pure
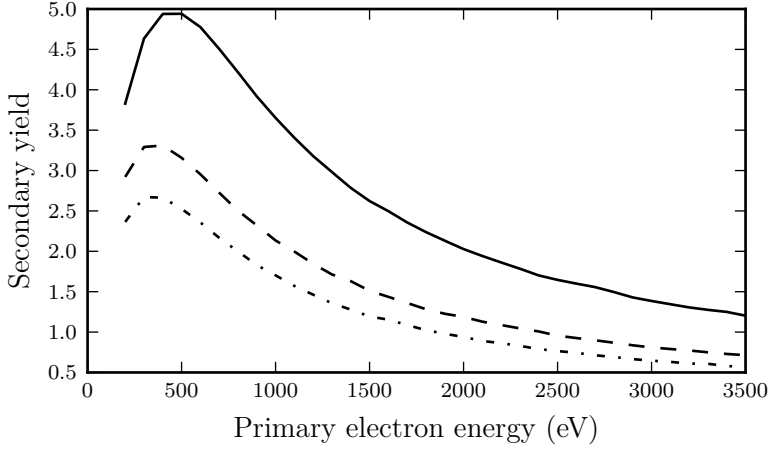
Figure 5.7: The reflection secondary electron yield for Si_3N_4 (solid line), $Si_{13}N_{15}$ (dashed line) and Si_7N_7 (dash-dotted line).

silicon nitride and this helps in preventing charge up effects.

5.2.3 Dopant distribution

Up to now we have only looked at silicon rich silicon nitride where the extra silicon atoms are distributed homogeneously over the material with the same crystal structure as pure silicon nitride. In this case, every extra silicon atom introduces one dangling bond, as it replaces one nitrogen atom in the crystal structure. Other distributions of the extra silicon atoms are also possible. One option would be that the extra silicon atoms group together in clusters. In these clusters, at least some of the dangling bonds can be removed, i.e. two silicon atoms both with a dangling bond can bond to each other, thus removing two dangling bonds. As a result, we expect the energy loss peaks due to the extra silicon atoms to decrease for such a dopant distribution. Indeed, when we compare the energy loss function of Si_7N_7 with silicon clusters to that of homogeneous Si_7N_7 in Figure 5.8, we see the energy loss peaks below 10 eV decrease. The energy loss function of Si_7N_7 with silicon clusters has energy loss peaks at 0.6 eV, 2.5 eV, 3.4 eV. The energy loss peaks are such that in between 2 eV and 10 eV, the energy loss functions
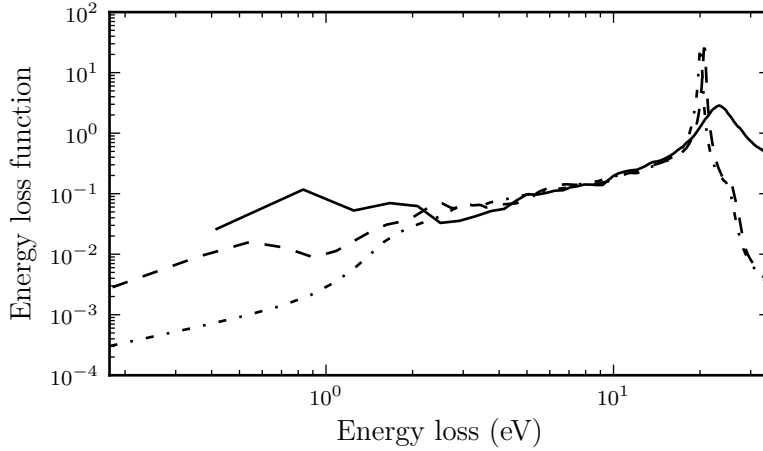
Figure 5.8: The energy loss functions for the different structures of Si_7N_7. The extra silicon atoms can be distributed homogeneously (solid line) or in clusters (dashed line) over the material, or the material as a whole can be amorphous (dash-dotted line).

for homogeneous and clustered Si_7N_7 are comparable and below 2 eV, the energy loss function for clustered Si_7N_7 is lower than that for homogeneous Si_7N_7. A third possibility is amorphous Si_7N_7. In this case, all atoms are allowed to relax and possibly even more of the dangling silicon bonds can be removed. The energy loss function for amorphous Si_7N_7 in Figure 5.8 indeed shows less low energy loss peaks, which seems to suggest that more silicon dangling bonds are removed. The energy loss function of amorphous Si_7N_7 has only one real energy loss peak left at 2.5 eV. For both the clustered and the amorphous Si_7N_7 the bulk energy loss peak is shifted from 24 eV to 20 eV and becomes more narrow. In fact, both peaks become more like the bulk plasmon peak of silicon (see Figure 2.13).

The removal or decrease of these energy loss peaks is expected to increase the secondary electron yield. When we allow the extra silicon atoms to form clusters and remove (part of) the dangling bonds, we remove (part of) the lattice defects. This decreases the probability for an electron travelling in the material to scatter at such a defect. The same holds for the amorphous
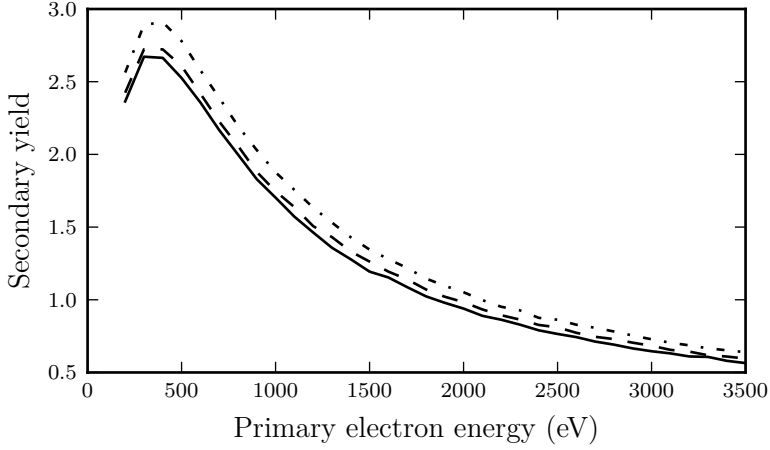
Figure 5.9: The reflection secondary electron yield for Si_7N_7 with the extra silicon atoms distributed homogeneously (solid line) and in clusters (dashed line) over the material, and the yield for amorphous Si_7N_7 (dash-dotted line).

Si_7N_7. In this case, the material is allowed to relax and remove (part of) the lattice defects naturally. This is a more effective way of removing the lattice defects, as we see in the energy loss function, where there are less energy loss peaks present for amorphous Si_7N_7 than for clustered Si_7N_7. We expect the secondary electron yield to increase when increasingly more lattice defects are removed. Indeed, in Figure 5.9 we see the maximum secondary electron yield increase. When we go from Si_7N_7 with homogeneously distributed silicon atoms to clustered silicon atoms, the maximum secondary electron yield increases from 2.67 at 350 eV to 2.72 at 350 eV, which is a small increase of 1.9 %. The increase in maximum secondary electron yield for amorphous Si_7N_7 is more prominent; the yield increases to 2.9 at 350 eV, a total increase of 8.5 %.

5.2.4   Hydrogen contamination

Hydrogen contamination can be present in silicon nitride as mentioned previously. Here we discuss the effect of hydrogen contamination in homogeneous Si_7N_7. We look at three exaggerated cases: $Si_7N_7H^{Si}$ where all hydrogen
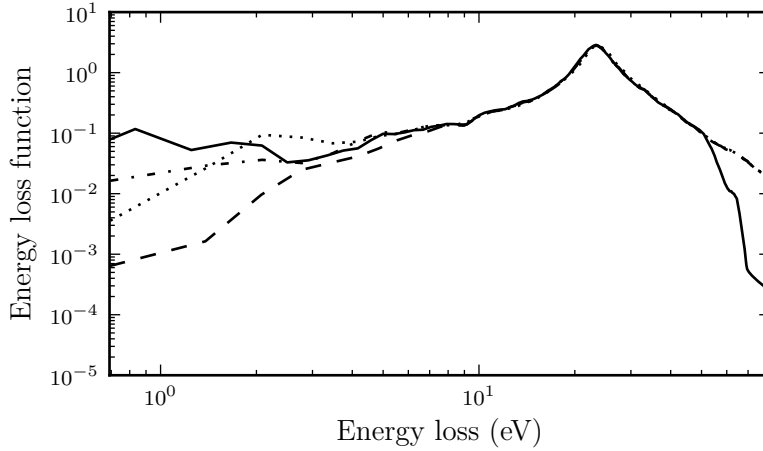
Figure 5.10: The energy loss functions for homogeneous Si_7N_7 (solid line), $Si_7N_7H^{Si}$ (dashed line), $Si_7N_7H^{N}$ (dash-dotted line), and $Si_7N_7H_2^{Si,N}$ (dotted line).

atoms are bonded to a silicon atom (1), or $Si_7N_7H^{N}$ all hydrogen atoms are bonded to a nitrogen atom (2) or $Si_7N_7H_2^{Si,N}$ where there are two hydrogen atoms present for every seven silicon and nitrogen atoms, one of these two is bonded to a silicon and one to a nitrogen atom (3). The effect of the hydrogen on the energy loss function is shown in Figure 5.10. The energy loss function of $Si_7N_7H^{Si}$ has only one energy loss peak left at 2.5 eV. In this case, the hydrogen atoms remove dangling bonds of the extra silicon atoms and decrease the inelastic scattering probability. When all the hydrogen atoms are bonded to nitrogen atoms ($Si_7N_7H^{N}$), the energy loss function shows no real energy loss peaks below 10 eV, although it is higher than when the hydrogen is bonded to silicon. When more hydrogen atoms are added, in $Si_7N_7H_2^{Si,N}$ the energy loss peaks at 0.8 eV and 1.7 eV disappear, but a new peak arises at 2 eV. The bulk energy loss peak gets a bigger high energy loss tail, in all cases when there is hydrogen contamination present. This is again more like the bulk energy loss peak for pure silicon nitride. Although the maximum of the bulk energy loss peak is not affected by the hydrogen contamination.
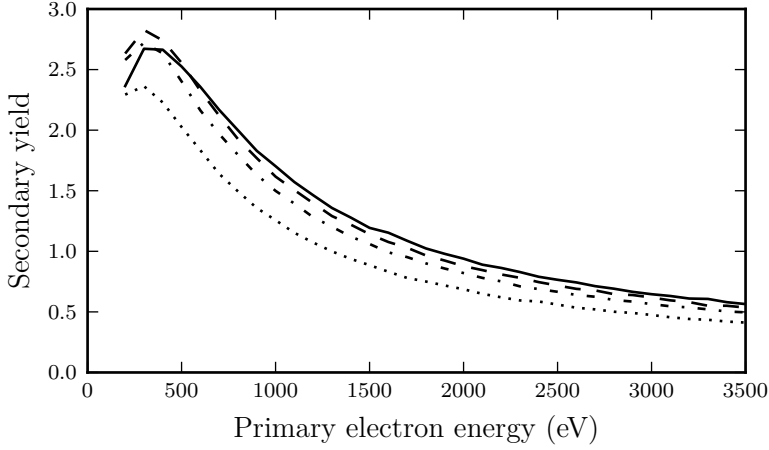
Figure 5.11: The reflection secondary electron yield for homogeneous Si_7N_7 (solid line), $Si_7N_7H^{Si}$ (dashed line), $Si_7N_7H^{N}$ (dash-dotted line), and $Si_7N_7H_2^{Si,N}$ (dotted line).

We expect the maximum secondary electron yield to be higher for $Si_7N_7H^{Si}$ than for $Si_7N_7H^{N}$, because in $Si_7N_7H^{Si}$ the hydrogen atoms can more effectively remove the silicon dangling bonds than in $Si_7N_7H^{N}$. For $Si_7N_7H_2^{Si,N}$ we expect the maximum secondary electron yield to be the lowest, because now the hydrogen atoms bonded to nitrogen atoms will cause new lattice defects. We indeed see this in Figure 5.11, where the secondary electron yield of $Si_7N_7H^{N}$ is 2.7 at 300 eV, slightly lower than that of $Si_7N_7H^{Si}$, which is 2.8 at 300 eV. The secondary electron yield of $Si_7N_7H_2^{Si,N}$ is lower still with 2.4 at 300 eV.

When we compare the maximum secondary electron yields to that of homogeneous Si_7N_7 we see the maximum secondary electron yield of $Si_7N_7H^{N}$ is the same as Si_7N_7, the maximum yield of $Si_7N_7H^{Si}$ is increased by 4 %, and the maximum secondary electron yield of $Si_7N_7H_2^{Si,N}$ is decreased by 11 %. So although it is a stretch to say that the hydrogen contamination is beneficial to the secondary electron yield, a small amount of contamination is not harmful at least.

5.3   Conclusion

In the case of silicon rich silicon nitride, the band structure and energy loss function depending on doping level are not known from experiments. We have used the band structure and energy loss function calculated *ab initio* with density functional theory by Tao [58] to perform secondary electron yield simulations. By the use of these density functional calculations, we can very precisely control the exact composition and structure of the silicon rich silicon nitride we want to investigate. We have investigated the effect of the doping level, the distribution of dopants over the material and the effect of hydrogen contamination. The only parameter for which we were not able to determine a value was the acoustic deformation potential. However, we did find that experimental values for the secondary electron yield maximum and its respective primary energy could be used to fit the acoustic deformation potential. Additionally we do not expect the acoustic deformation potential to depend on the doping level. Hence we chose to set the acoustic deformation potential to 12 eV. This choice makes it possible to simulate the secondary electron yield for the different forms of silicon nitride and to compare the results qualitatively.

Increasing the doping level leads to a decrease in maximum secondary electron yield of 34 % for $Si_{13}N_{15}$ and 46 % for Si_7N_7 compared to Si_3N_4.

The extra silicon atoms in silicon rich silicon nitride will introduce dangling bonds that cause the secondary electron yield to decrease. The exact distribution of these extra silicon atoms determines how much the secondary electron yield decreases. When the extra silicon atoms are placed in clusters in Si_7N_7 to remove some of the dangling bonds, the maximum secondary electron yield increases by 1.9 % compared to homogeneous Si_7N_7. A more effective way to remove the lattice defects is to let the silicon rich silicon nitride relax to amorphous Si_7N_7. Then the maximum secondary electron yield increases by 8.5 % compared to homogeneous Si_7N_7. Note that this is still lower than the maximum secondary electron yield of Si_3N_4 and $Si_{13}N_{15}$.

If there is hydrogen contamination present in Si_7N_7, we found that this hydrogen contamination can remove (part of) the dangling silicon bonds and

for Si_7N_7H the hydrogen atoms are not harmful to the secondary electron yield. It does not matter much whether the hydrogen is bonded to silicon or nitrogen atoms in this case. The maximum secondary electron yield for $Si_7N_7H^N$ is the same as for homogeneous Si_7N_7 and the maximum secondary electron yield for $Si_7N_7H^{Si}$ increases by 4 % compared to homogeneous Si_7N_7. However, increasing the amount of hydrogen contamination further to obtain $Si_7N_7H_2^{Si,N}$ will cause the maximum secondary electron yield to decrease by 11 % compared to homogeneous Si_7N_7.

Chapter 6

X-ray photoelectron spectroscopy

In the previous chapter we have discussed secondary electron emission of silicon rich silicon nitride. During this project, we also wanted to investigate the effect of different doping levels in an experimental setup. At the time we thought X-ray photoelectron spectroscopy (XPS) would be a good method to compare the effects of different doping levels. The first part of this chapter covers the results of our attempts to use XPS to obtain information about the secondary electron yield of different samples.

The second part of this chapter covers simulations we did to reproduce the experimental XPS spectra. We would like to warn the reader in advance that the simulator itself was not designed for this purpose. It was designed to simulate electrons incident on a sample and the resulting secondary electron trajectories. In the case of XPS simulations, the primary particles are photons. The simulator does have the option to simulate photons incident on a sample, but this has its limits. For example, photon energies below 250 eV are not possible within our simulation package. In other words, we have pushed the limits of our simulation package.

6.1   Experiments

Initially we wanted to determine the secondary electron yield of silicon rich silicon nitride with different doping levels and different surface terminations. For this purpose, multiple samples of silicon rich silicon nitride with different doping levels and different surface terminations were fabricated [5]. However, at the time we did not have an experimental setup available to directly measure the secondary electron yield of a sample. We did have access to the National Synchrotron Light Source (NSLS) at Brookhaven National Laboratory. In fact, we performed our experiments in the last weeks before the NSLS was decommissioned to make place for the NSLS-II. For our experiments, we used beamline U1 where we could irradiate the samples with low-energetic photons and detect the produced photoelectrons and secondary electrons [63].

The original idea of the experiments was to perform XPS experiments on the silicon rich silicon nitride samples at two different photon energies, one just below and one just above the nitrogen Auger edge. The expectation was that the main difference between the secondary electron peaks of these two spectra would be due to the secondary electrons created by nitrogen Auger electrons. Then the idea was to estimate the total number of Auger electrons N_{Auger} from the detected number of Auger electrons. An estimate for the secondary electron yield due to the Auger electrons $SEY(E_{Auger})$ would then be

$$SEY(E_{Auger}) = \frac{\Delta SE}{N_{Auger}}, \tag{6.1}$$

Where ΔSE is the difference between the secondary electron peaks of the two spectra. The idea was that in this way, we could get an idea of the relative secondary electron yields of the different silicon rich silicon nitride samples.

In order to use this method, we would need to see a clear Auger peak, so that we could easily determine the number of Auger electrons detected. Before we go on, we would like to give a rough estimate of the probability per incident photon to detect an Auger electron. For this estimate, we will use the probability that a photon is absorbed at a certain depth. In Equation

2.71 the dependence of the photon intensity on the depth in the sample was given. From this we can derive the probability $P_{abs}(z, \nu)$ that a photon is absorbed at a specific depth as

$$P_{abs}(z, \nu) = \frac{-1}{I_0} \frac{dI(z, \nu)}{dz} = \frac{1}{\lambda(\nu)} e^{-z/\lambda_\gamma(\nu)}, \qquad (6.2)$$

where $\lambda_\gamma(\nu)$ is the energy dependent photon absorption length. For our estimate we also need the probability that an Auger electron escapes the sample without losing energy. This means that the electron does not scatter inelastically before reaching the surface. For a first order approximation, we will assume the Auger electron is travelling towards the surface and we will ignore elastic scattering. The probability $P_e(z, E)$ that the Auger electron does not scatter inelastically before reaching the sample surface is

$$P_e(z, E) = e^{-z/\lambda_i(E)}, \qquad (6.3)$$

where $\lambda_i(E)$ is the energy dependent inelastic mean free path of the Auger electrons. Now we want to get an upper bound for the probability per incident photon that an Auger electron is produced and that it escapes the sample. If we assume that every absorbed photon results in one nitrogen Auger electron, the total probability P_{esc} per incident photon that an Auger electron escapes becomes

$$P_{esc}(E, \nu) = \int_0^\infty P_e(z, E) P_{abs}(z, \nu) \, dz = \frac{\lambda_i(E)}{\lambda_i(E) + \lambda_\gamma(\nu)}. \qquad (6.4)$$

At the photon energy we will be using (420 eV), the photon absorption length is 147 nm (extracted from [30]). For the nitrogen Auger electrons, the inelastic mean free path will be 1 nm (extracted from the calculated inelastic mean free path for homogeneous Si_7N_7 in the previous chapter). Plugging these numbers into Equation 6.4 gives a probability per incident photon of 0.7 % that an Auger electron escapes. We would like to point out that this is an upper estimate. In reality, not every photon will be absorbed by a nitrogen K-shell electron and thus, not every absorbed electron can lead to

a nitrogen Auger electron. We also did not take the initial direction of the Auger electrons and elastic scattering into account. If we would take all these effects into account, the probability for the Auger electrons to escape would become even lower. A probability of 0.7 % that an Auger electron is emitted with its initial energy is very low, so depending on the detector noise, the method proposed in Equation 6.1 might not be a very feasible method.

6.1.1   Sample preparation

The samples used for the experiments were $1\,\mu m$ thick silicon rich silicon nitride, produced with plasma enhanced chemical vapour deposition, on top of silicon substrates. With energy dispersive X-ray spectroscopy in a scanning electron microscope, we determined the silicon to nitrogen ratios of the different doping levels to be 45/55 for the lowest, 49/51 for the intermediate and 50/50 for the highest doping level [63]. Note that $Si_{13}N_{15}$ is somewhere in between the lowest and the intermediate doping level and Si_7N_7 is equal to the highest doping level. Another aspect we wanted to investigate was how a surface termination affects the secondary electron yield of a sample. For this purpose we performed hydrogen termination by leaving the samples in an RF plasma system and heating the samples to 500 degrees Celsius exposing them to a ~ 50 mTorr plasma for 1 hour. On other samples we performed oxygen termination by placing them under a UV lamp in air for 16 hours. Hydrogen termination is expected to increase the secondary electron yield of silicon nitride [64]. Oxygen termination could be used in combination with alkali metals or hydrogen termination in order to increase the secondary electron yield [65]. In this case, the oxygen atoms would be bonded to the surface and the alkali metal or hydrogen atoms would be bonded to the oxygen atoms, forming dipoles that decrease the electron affinity of the surface.

6.1.2   Experimental setup

The XPS experiments were done at beamline U1 at the NSLS as mentioned previously. Beamline U1 was one of the beamlines at the VUV ring, containing 2.8 GeV electrons. The angular momentum of the electrons changed

when they orbited the VUV ring. As a result, the electrons lost energy and emitted photons. Before these photons ended up in one of the beamline end stations, the photons were collimated and sent through a monochromator to get one single wavelength at the end station.

At beamline U1 the photons were then used to irradiate the sample, where the incoming photon direction was parallel to the surface normal of the samples. At an angle α of 45 degrees with the surface normal, a cylindrical mirror analyser (CMA) was placed to detect the electrons emitted by the sample as a result of the incoming photons, see also Figure 6.1. This CMA counted the number of electrons and detected their kinetic energy. Only electrons emitted inside the opening angle of the detector were detected. In our case this meant that electrons for which the angle β with the detector central axis was between 39 and 45 degrees were detected [66]. It was also possible to put a voltage of -15 V on the samples so that escaped electrons with only a few eV could still easily reach the detector.
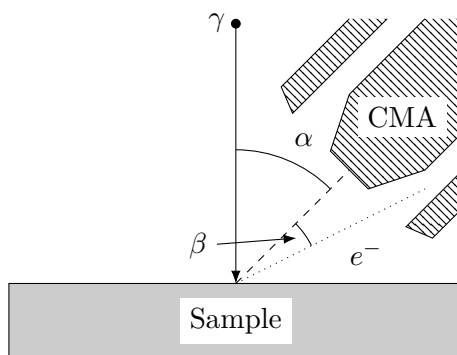

Figure 6.1: The experimental XPS setup. The direction of the incoming photons (γ) is parallel to the sample surface normal. The cylindrical mirror analyser (CMA) central axis is placed under an angle α to the surface normal. Emitted electrons are detected by the CMA when their angle β with the detector central axis falls inside the detector opening angle.

6.1.3   Experimental results

As mentioned previously, we irradiated the silicon rich silicon nitride samples
with photons with an energy just below and an energy just above the nitrogen
Auger edge. From the nitrogen binding energies in [30] we can deduce that
the nitrogen Auger edge is at 410 eV, so we chose our photon energies to be
400 eV and 420 eV. In Figure 6.2 the spectrum at 420 eV for an untreated
silicon rich silicon nitride sample is shown. In this case, the highest doping
level (50/50) was used and the sample was not biased. Note that the x-axis
gives the kinetic energy of the electrons as detected by the detector.

Figure 6.2: Experimental XPS spectrum of silicon rich silicon nitride (50/50)
at a photon energy of 420 eV. The sample was not biased.

The secondary electron peak is very high with a maximum of 380 counts
per second; we need to zoom in to see the photoelectron and Auger electron
peaks in the inset. We see silicon photoelectron peaks at 263 eV and 314 eV
and a nitrogen photoelectron peak at 389 eV. Around 373 eV we see some-
thing that could be the nitrogen Auger peak, but it is a very small peak.
Lastly, we see a peak at 133 eV, which we cannot explain when we take only
silicon and nitrogen into account. However, the samples might be contam-
inated. In fact, carbon contamination would explain the photoelectron peak

at 133 eV perfectly.

Now if we want to use Equation 6.1, we have to determine the number of electrons in the nitrogen Auger peak. In order to do this we need to subtract the background from the Auger peak. However, hence we need to determine the background. In Figure 6.3 a detail of the spectrum from Figure 6.2 is shown. The grey area marks the nitrogen Auger peak and two different choices for the background are given by the dashed and dotted lines. These two different choices lead to either 0.32 or 0.39 Auger electrons detected per second. This is a difference of about 20 %. The difference between the maximum yield of $Si_{13}N_{15}$ and Si_7N_7 in Figure 5.7 was also 20 %. Which means that if we see a difference in the yield obtained using Equation 6.1 for different materials, we do not know whether this difference is because the yield of the samples is different or if this is a result of our choice for the background. In other words, the uncertainty in determining the background makes it impossible to use Equation 6.1 in order to compare the estimated yields for the different doping levels and terminations.

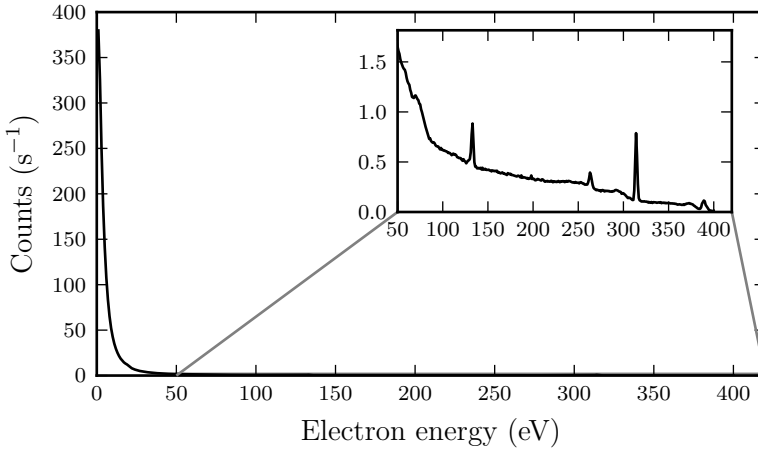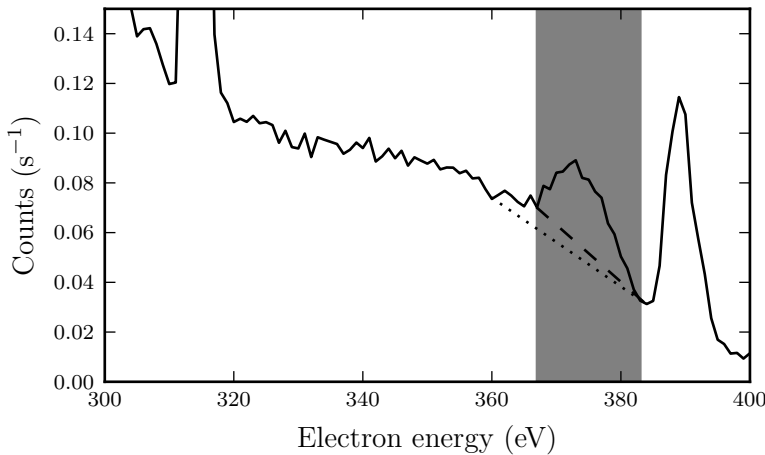Figure 6.3: Detail of the experimental XPS spectrum of silicon rich silicon nitride (50/50) at a photon energy of 420 eV. The sample was not biased. The nitrogen Auger peak is marked by the grey area. Two different choices for the background are given by the dashed and the dotted lines.

Instead we decided to take the total number of electron counts. When the total electron count is consistently higher at different photon energies for a certain sample than for another sample, it is safe to say that the yield for that sample is higher. Note that it is important that the number of photons that went into both spectra needs to be the same in order to be able to make this comparison. The number of photons varies slowly with energy. The variation is small enough that it would not have been a problem if we would have used the method proposed in Equation 6.1, but we do need to be careful when comparing the total number of electron counts at different energies. Also note that since we compare the total electron counts, we have normalised all spectra to the electron current in the VUV ring so as to normalise the spectra on the same number of photons. Even though we don't know exactly how many photons went into each spectrum, we can safely assume that the number of photons is equal for spectra taken at the same photon energy. The total number of electron counts for the spectrum shown in Figure 6.2 is 2074 counts per second.

6.1.3.1   Surface termination

First we will look at the effect of the different surface terminations on the total number of electron counts for the highest doping level (50/50). We had three samples with the highest doping level: one untreated, one hydrogen terminated and one oxygen terminated. In Figure 6.4 part of the XPS spectrum for the oxygen terminated sample is shown. We do not see a nitrogen Auger peak nor do we see a clear nitrogen photoelectron peak. It seems the oxygen termination treatment affected the top layers of the sample in such a way as to remove the nitrogen. After argon sputtering, we did see a nitrogen Auger peak again, so it seems the sputtering removed the top layers that were affected by the oxygen termination treatment. However, now the oxygen termination is probably also removed. So we cannot say with certainty that we measured on an oxygen terminated sample.

We had more luck with the hydrogen terminated sample. The spectrum for the hydrogen terminated high doping level silicon rich silicon nitride for a photon energy of 420 eV is shown in Figure 6.5. We see the same

Figure 6.4: Part of the experimental XPS spectrum of oxygen terminated silicon rich silicon nitride (50/50) at a photon energy of 420 eV. The sample was not biased.
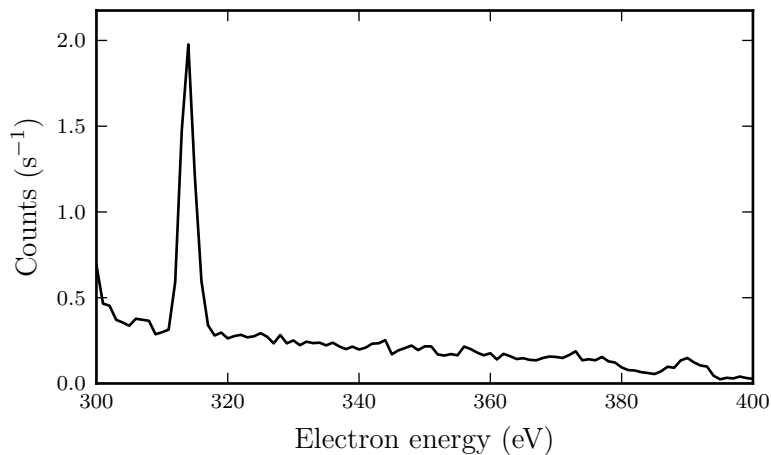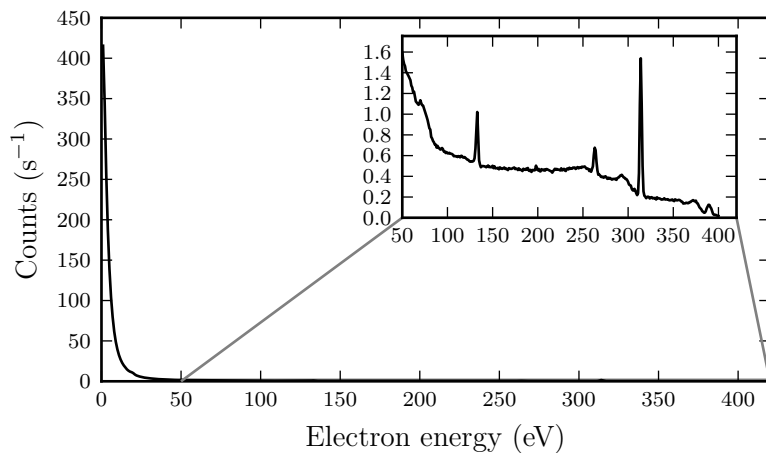

Figure 6.5: Experimental XPS spectrum of hydrogen terminated silicon rich silicon nitride (50/50) at a photon energy of 420 eV. The sample was not biased.

photoelectron and Auger peaks as we did for the untreated sample. The total number of electron counts for the spectrum in Figure 6.5 is 2124. This

photon energy (eV)	untreated	hydrogen terminated
150	3653	7314
200	2950	8456
250	2224	6237
300	934	1676
400	550	860

Table 6.1: The experimental total electron count for untreated and hydrogen terminated silicon rich silicon nitride (50/50). The total electron count for the hydrogen terminated sample is consistently higher than for the untreated sample. In all cases the samples were biased by -15 V.

is higher than for the untreated sample, however, it is only one measurement.

So we decided to take XPS spectra of both samples at more photon energies. In Figures 6.6 and 6.7 the spectra for the untreated and hydrogen terminated high doping level silicon rich silicon nitride at 150 eV and 400 eV are compared. Note that the samples were biased by -15 V. In both cases the secondary electron peak is higher for the hydrogen terminated sample compared to the untreated sample.
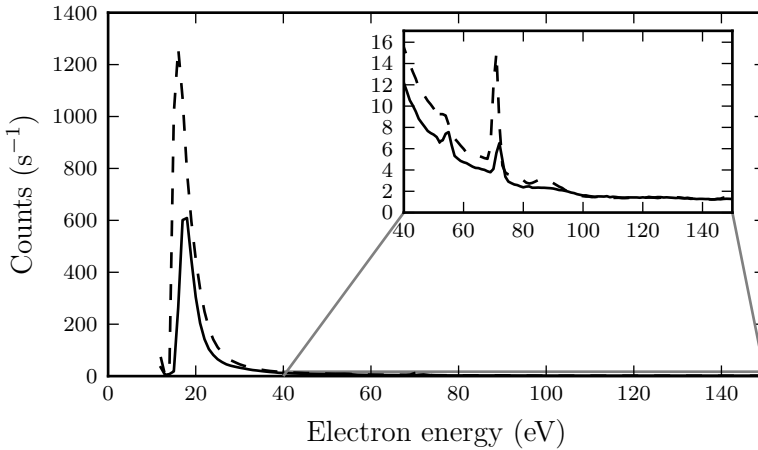

Figure 6.6: Experimental XPS spectra of untreated (solid line) and hydrogen terminated (dashed line) silicon rich silicon nitride (50/50) at a photon energy of 150 eV. The samples were biased by -15 V.
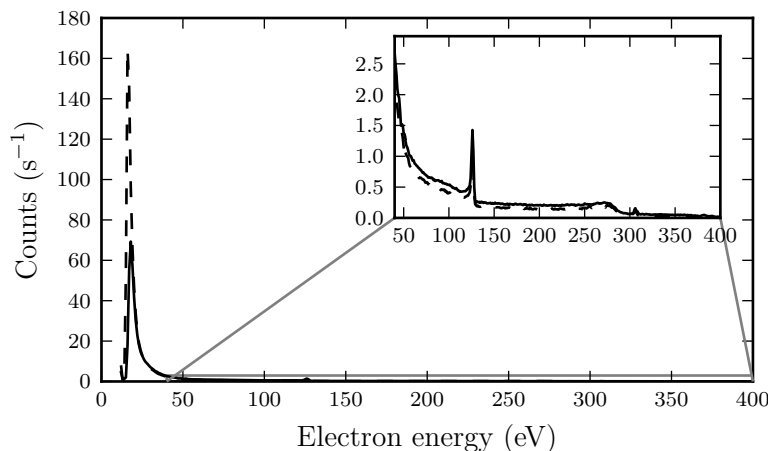
Figure 6.7: Experimental XPS spectra of untreated (solid line) and hydrogen terminated (dashed line) silicon rich silicon nitride (50/50) at a photon energy of 400 eV. The sample is biased by -15 V.

The total electron counts for the spectra at all investigated energies are shown in Table 6.1. The total electron counts for the hydrogen terminated sample are consistently higher than for the untreated sample. This indicates that the secondary electron yield of silicon rich silicon nitride indeed increases when a sample is hydrogen terminated.

6.1.3.2   Doping level

Now we will look at the effect of the different doping levels on the XPS spectra. We had samples with three different doping levels. Unfortunately, the samples with the lowest doping level (45/55) suffered from charging and we could not use their spectra. We had one sample of the intermediate doping level, which was hydrogen terminated. The full XPS spectrum of this sample, at a photon energy of 420 eV, is shown in Figure 6.8.

The sample was not biased and the total electron count is 1851, which is lower than for the hydrogen terminated high doping level sample (2124). However, in the previous chapter we saw that the secondary electron yield decreases with increasing doping level, so this result is not what we expec-
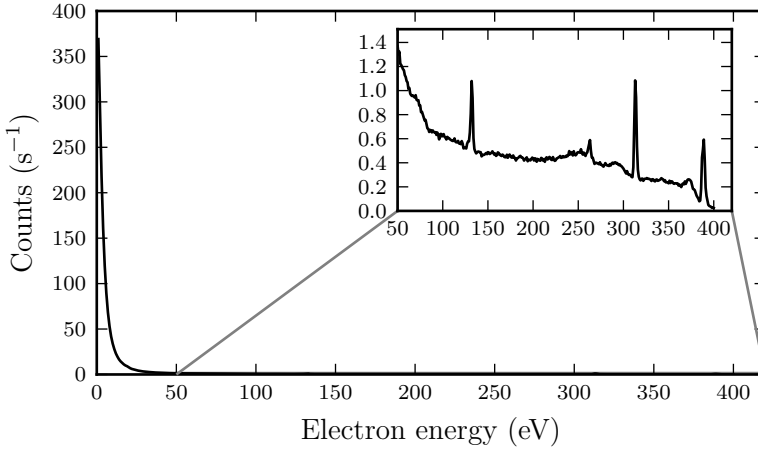
Figure 6.8: Experimental XPS spectrum of hydrogen terminated silicon rich silicon nitride of intermediate doping level (49/51) at a photon energy of 420 eV. The sample was not biased.

ted. Charging might be an explanation of why the total count rate for the (49/51) sample is lower than for the (50/50) sample. The lowest doping level samples (45/55) visibly suffered from charging effects. It could be that the intermediate doping samples (49/51) still suffered from charging effects, thus decreasing the total electron count.

6.2   Simulations

With our simulation package, we are able to choose a photon as primary particle in order to simulate an XPS spectrum. In these simulations, we placed a detector just above the sample. The simulated detector did not detect or disturb the incoming photons, but it did detect all electrons that escaped from the sample. For all following simulation results we simulated 2 million photons hitting the samples and all electrons emitted by the sample were detected.

The full simulated XPS spectrum of homogeneous Si_7N_7 is shown in Figure 6.9 and the total electron count is 127112. Note that we cannot
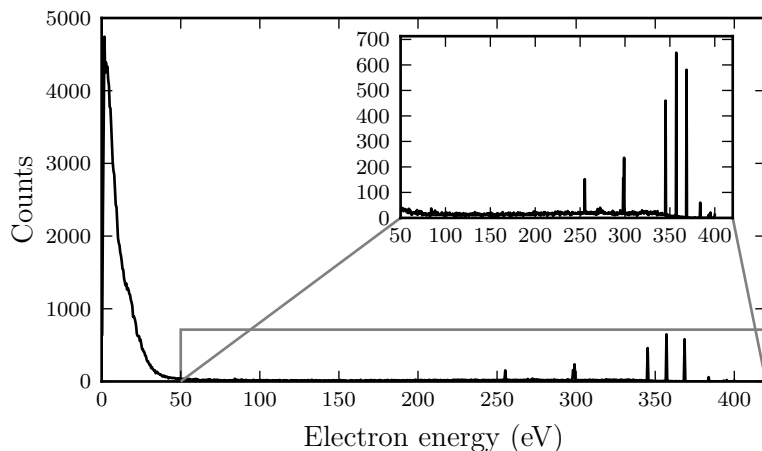
Figure 6.9: Simulated XPS spectrum of homogeneous Si_7N_7.

compare the total electron count to the experimental results, since we do not know the number of photons that irradiated the samples per second in the experiments. What we can do however, is compare the simulated spectrum qualitatively to the experimental spectrum in Figure 6.2. The high energy peaks present are two silicon photoelectron peaks at 255 eV and 299 eV, a nitrogen photoelectron peak at 384 eV and three nitrogen Auger peaks at 345 eV, 357 eV and 369 eV. All these peaks are at slightly different energies than their counterparts in the experimental results. This points to a difference between the shell energies of the silicon and nitrogen atoms used in the simulations and the actual shell energies. The shell energies used in the simulations are atomic shell energies [32]. However in a solid, the combined potential landscape of all atoms shifts the (outer) shell energies. Since this is not taken into account in the simulations, it is only logical that the simulated peaks are slightly shifted compared to the experimental peaks. We also see three nitrogen Auger peaks in the simulation results compared to only one in the experimental results. There are three Auger peaks, because either the L1, L2 or L3 electron is emitted as Auger electron.

Another difference between the experimental spectrum and the simulated spectrum is the width of the photon and Auger peaks. The simulated peaks

are very narrow, not at all like the experimental peaks. In the simulations we
have an ideal detector; it detects all electrons and it has an infinite energy
resolution. In reality, a detector is never perfect; its opening angle and
resolution will affect the experimental results. In the next sections, we will
change the parameters of the simulated detector more in agreement with the
experimental circumstances and obtain a simulated spectrum which closer
resembles the experimental spectrum.

6.2.1   Opening angle

First we will take the positioning and opening angle of the detector as shown
in Figure 6.1 into account. This means that we implemented a check for every
electron emitted by the simulated sample to see if its direction was inside
the opening angle of the detector. If the electron direction was inside the
opening angle, it was counted, otherwise the emitted electron was discarded.
The resulting spectrum is shown in Figure 6.10 and the total electron count
is 6528. The high energy peaks all decreased in height and the photoelectron
peaks at 255 eV and 384 eV have disappeared into the noise of the spectrum.
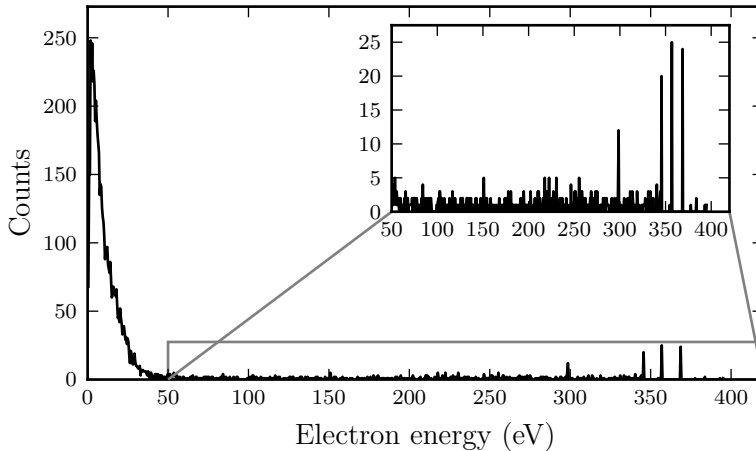
Figure 6.10: Simulated XPS spectrum of homogeneous Si_7N_7 taking the
detector opening angle into account.

6.2.2   Detector resolution

The second effect that the detector has on the measured spectrum is the detector resolution. In the simulations, we can 'detect' the exact energy of the electrons. However, in reality, the detector will have a finite resolution. During our experiments, the detector had a spectral resolution of approximately 1.6 eV full width at half maximum (FWHM). In order to take this detector resolution into account, we have performed a convolution between the spectrum as shown in Figure 6.10 and a Gaussian function with a FWHM of 1.6 eV. The resulting spectrum is shown in Figure 6.11. The total electron count is 6473. Now the simulated spectrum looks more like the spectrum in Figure 6.2. However, until now we have ignored the fact that there was a carbon peak present in the experimental spectra, which we of course do not see in the simulated spectrum, since it was not taken into account.
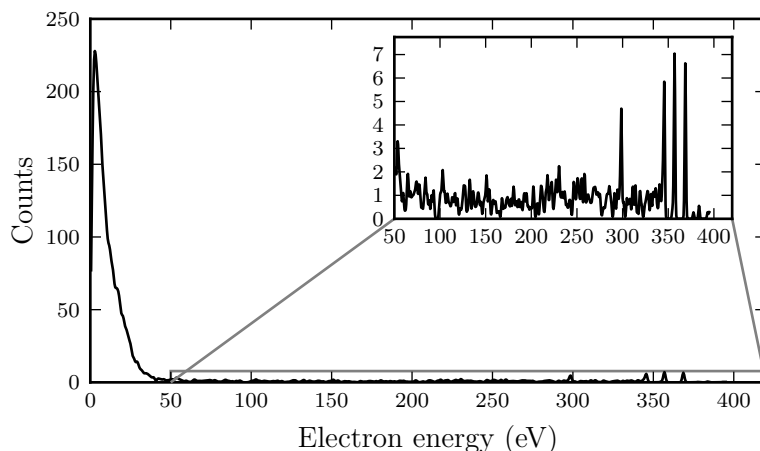

Figure 6.11: Simulated XPS spectrum of homogeneous Si_7N_7 taking the detector resolution as well as the detector opening angle into account.

6.2.3   Carbon

To account for the carbon contamination in the experimental results, we have simulated the effect of a 0.5 nm thick graphite layer on top of homogeneous

Si_7N_7. The resulting spectrum is shown in Figure 6.12. The total secondary electron count then becomes 5808. Now we also see a carbon photoelectron peak at 116 eV in the spectrum. At 369 eV we see a nitrogen Auger peak. The silicon photoelectron peak at 314 eV and the nitrogen Auger peaks at 345 eV and 357 eV that were present before might still be present, but are hard to distinguish in between the noise. Next to the carbon photoelectron peak at 116 eV, we see three extra new peaks arise at 243 eV, 252 eV and 260 eV. A simulation of a graphite sample pointed out that these peaks are carbon Auger electrons.
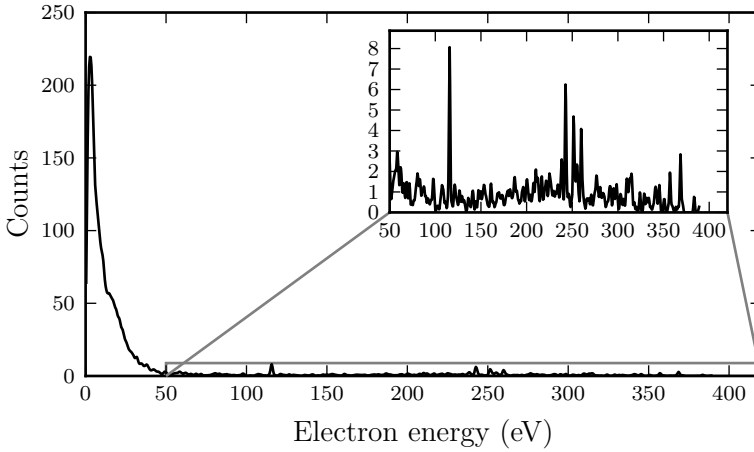
Figure 6.12: Simulated XPS spectrum of homogeneous Si_7N_7 with a 0.5 nm graphite surface contamination layer taking the detector opening angle as well as the detector resolution into account.

Comparing the simulated and experimental spectra qualitatively is not very feasible. There are simply too many unknowns; the thickness and exact form (density) of the carbon contamination layer in the experiments and the number of photons that went into the experimental spectra are unknown. Comparing the number of electrons in the photoelectron and Auger peaks is also difficult, exactly for the same reasons why we did not use the method proposed in Equation 6.1. However, what we can do is look at the dependence of the total number of electron counts on the photon energy for homogeneous

photon energy (eV)	Counts Si_7N_7	Counts $Si_{13}N_{15}$
250	4991	5593
300	5264	6006
400	3733	4361

Table 6.2: The total electron counts as simulated for homogeneous Si_7N_7 and $Si_{13}N_{15}$ with a 0.5 nm graphite surface contamination layer.

Si_7N_7 and $Si_{13}N_{15}$.

We simulated XPS spectra for homogeneous Si_7N_7 and $Si_{13}N_{15}$ with a 0.5 nm graphite surface contamination layer at different photon energies. The resulting total electron counts are given in Table 6.2. Note that GEANT4 cannot simulate photons below 250 eV, so we cannot simulate all energies in Table 6.1. Again we have to be careful when comparing the values in Table 6.2 to those in Table 6.1. The samples were biased by -15 V during the experiments, but in the simulations we do not have the possibility to bias the samples. What we can say is that the simulation results do not give the same trends as the experimental results; the total electron count for $Si_{13}N_{15}$ is higher than for Si_7N_7, contradictory to the experimental results, where the highest doping level sample had the higher total electron count. However, it might be the case that the intermediate doping level sample suffered from charging effects during the experiments, which is not modelled in the simulations. In the experimental results, the total electron count decreases with increasing photon energy from 250 eV to 400 eV, in the simulation results the total electron count increases when the photon energy is increased from 250 eV to 300 eV and decreases again for 400 eV photons. However, again we have to be careful with our comparison; exactly 2 million photons were used for all simulation results. In the experiments, we do not know the number of photons and the number of photons changes with the photon energy.

6.2.4   Surface sensitivity

Similarly to how we looked at the creation escape length of electrons in alumina (see Figure 4.2) we can also look at the creation escape length of the photoelectrons created in a simulation of an XPS experiment. XPS is a sur-

face sensitive method, the photoelectron creation escape length can give us a measure of how surface sensitive XPS actually is. In Figure 6.13 the probability density function of the creation depth of all emitted photoelectrons at a photon energy of 420 eV is shown.
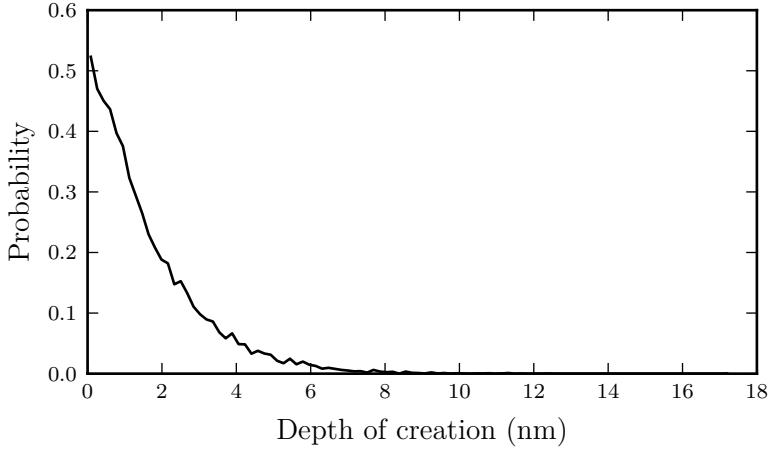
Figure 6.13: Probability density function of the creation depth of emitted photoelectrons from homogeneous Si_7N_7 at a photon energy of 420 eV. Note that the probability density function is normalised with a bin width of 0.17 nm.

Now we will fit the same Equation that we used for the electron creation escape length in alumina; Equation 4.1. This fit gives a creation escape length for the photoelectrons of $\lambda_{esc} = 1.68$ nm. Note that in this case all photoelectrons that escaped the sample are taken into account, not just the photoelectrons that escaped with their initial energy or the ones that were inside the detector opening angle.

6.3   Conclusion

This chapter consisted of two parts, in the first part experimental results were discussed. The experimental method we planned to use to determine the secondary electron yield using the Auger peak in the XPS spectra did not

work. So we decided to compare the total electron count of the spectra for the different surface terminations and doping levels of silicon rich silicon nitride. The experimental results showed that hydrogen termination increases the secondary electron yield of (silicon rich) silicon nitride as expected in [64]. The experiments also resulted in a lower total electron count for the intermediate doping level (49/51) than for the high doping level (50/50) silicon rich silicon nitride. We had expected the opposite results from our secondary electron yield simulations in the previous chapter. It might be that the (49/51) sample suffered from charging effects during the experiments.

In the second part of this chapter, we have tried to simulate XPS spectra of Si_7N_7 and $Si_{13}N_{15}$ with and without carbon contamination. The first simulation results looked very different from the experimental results. Taking the effects of the detector resolution and opening angle into account helps somewhat to make the spectra look more similar to the experimental spectra, but there are still differences.

We saw that the position of the high energy electron peaks is different in the simulation and the experimental results. This is due to the fact that the simulations use atomic shell energies, whereas the outer shell energies are expected to shift in a solid.

The simulated and experimental total electron counts are also different. However, we did not expect to find an exact match, since too many material parameters are unknown. We do not know the exact material parameters of the carbon contamination, nor do we know the amount (thickness) of the contamination. We also do not know the number of photons that went into making the experimental spectra and there is no charging in the simulations.

We would also like to point out that the Sauter distribution [31], which is used to determine the direction in which photoelectrons are emitted, might affect the relative heights of the photoelectron peaks. In Chapter 2 we reasoned that although the Sauter distribution is strictly speaking only correct for K-shell electrons in hydrogen, we could use this distribution because in most practical applications the mean free path of the (photo)electrons is much shorter than that of the photons. However, in this chapter we are specifically interested in the photoelectrons that do escape the sample. In

our simulations we saw that the photoelectrons typically escape without any interaction with the sample, or in some cases after one elastic scattering event. This means that the initial direction of the photoelectrons, which is governed by the Sauter distribution, directly affects the probability to escape for the photoelectrons. In the simulation results, we saw that the silicon photoelectron peak at 255 eV disappeared when we took the opening angle of the detector into account. The spectra with carbon contamination showed carbon Auger peaks again at 243 eV, 252 eV and 260 eV. Now we could say that the experimental peak at 263 eV is a carbon Auger peak since this follows from the simulations. However, since the Sauter distribution directly affects the probability for the photoelectrons to escape, it might well be that the experimental peak does contain both silicon photoelectrons and carbon Auger electrons and the simulations simply do not reproduce this correctly.

What we could do with the simulations was show that XPS is indeed a surface sensitive experimental method by determining the photoelectron creation escape length λ_{esc}. From our simulations it followed that $\lambda_{esc} = 1.68$ nm for homogeneous Si_7N_7 at a photon energy of 420 eV.

Although we were able to bridge the biggest differences between the simulation and experimental results, the method we initially wanted to use to compare the different doping levels and surface terminations did not work. There still remain differences between the experimental and simulation results. More work is needed in order to investigate these differences further and maybe be able to remove them. Then maybe the simulation package can be used to accurately predict XPS spectra, although this was not the intended purpose of the simulation package.

Chapter 7

Design of prototype tynodes

Now that we have a simulation package that is able to simulate the secondary electron yield in reflection mode as well as in transmission mode and that we have tried to replicate experimental XPS spectra with the simulation package, we would like to use the simulation package for the purpose for which it was developed. The motivation for developing the simulation package was to be able to predict the best thickness for prototype tynodes to be used in the **Ti**med **P**hoton **C**ounter (TiPC). In [67] and [68] magnesium oxide looks like a promising material to be used as tynode material. So in this chapter we will use the simulation package to predict the optimum membrane thickness and the accompanying optimum energy for the primary electrons for magnesium oxide.

7.1 Material parameters

We were able to find most of the material parameters for magnesium oxide. These are listed in Appendix A. Two material parameters deserve more explanation; the energy loss function and the acoustic deformation potential.

7.1.1 Energy loss function

The energy loss function for magnesium oxide we used is from [60] and it is shown in Figure 7.1.
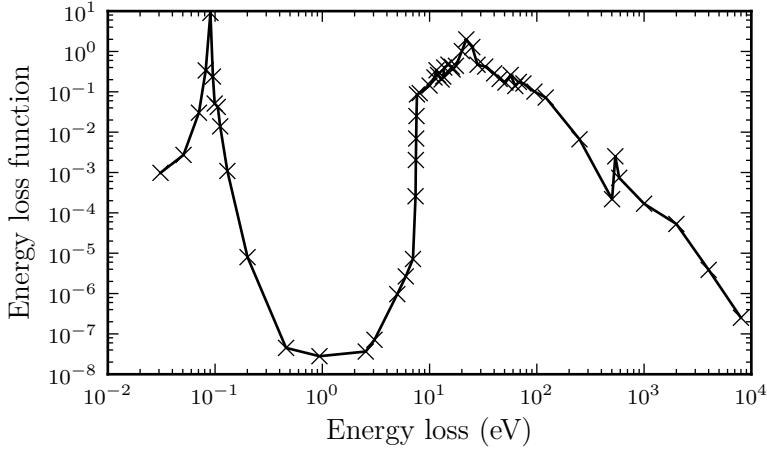
Figure 7.1: The energy loss function of magnesium oxide from [60].

Below 0.1 eV we see a longitudinal optical phonon loss peak, followed by the wide band gap of 7.8 eV [69, 70]. At 22 eV we see the bulk plasmon loss peak, from 57 eV and up we see inner shell excitations of magnesium and oxygen.

7.1.2   Acoustic deformation potential

We were not able to find the acoustic deformation potential of magnesium oxide. Similar as for silicon nitride we decided to 'fit' the acoustic deformation potential by simulating the secondary electron yield for the acoustic deformation potential in the range of 2 eV to 15 eV. A few of the resulting reflection secondary yield curves are shown in Figure 7.2.

Similar as for silicon nitride we see that the maximum secondary electron yield and the optimum primary energy both decrease with increasing acoustic deformation potential. In Figures 7.3 and 7.4 this dependence is shown in more detail. In literature we found several experiments to measure the reflection secondary electron yield of magnesium oxide films on substrates [35, 68, 71–73]. We were not able to find experimental values for bulk magnesium oxide. Jokela et al. report they could not measure magnesium oxide films

Figure 7.2: The reflection secondary electron yield of magnesium oxide for different values of the acoustic deformation potential ϵ_{ac}.
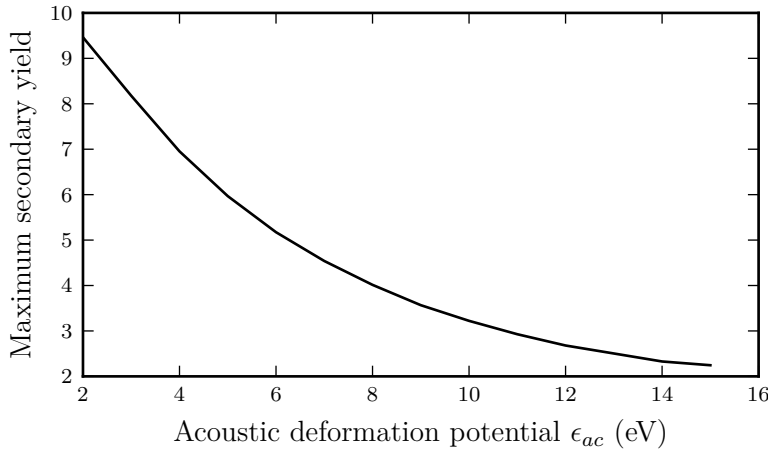
Figure 7.3: The maximum reflection secondary electron yield of magnesium oxide for different values of the acoustic deformation potential ϵ_{ac}.

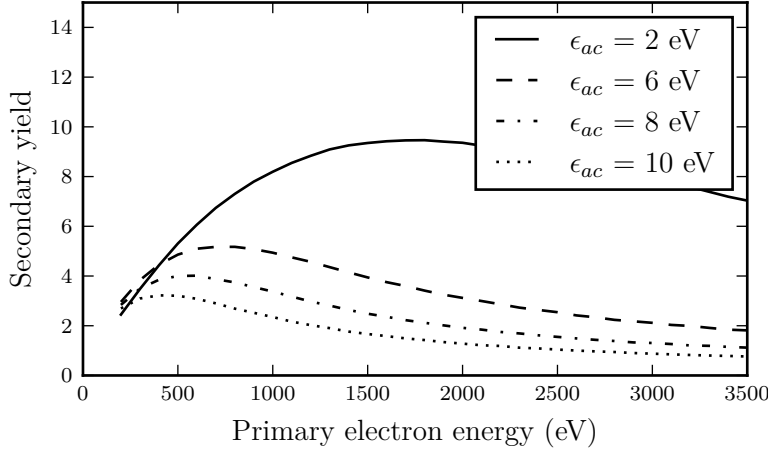over 200 nm, since these samples suffered from charging effects. The obtained experimental yield ranges from 3.3 for 100 nm magnesium oxide on a silicon substrate [73] to 24.3 for a 0.5 mm thick single crystal of magnesium oxide
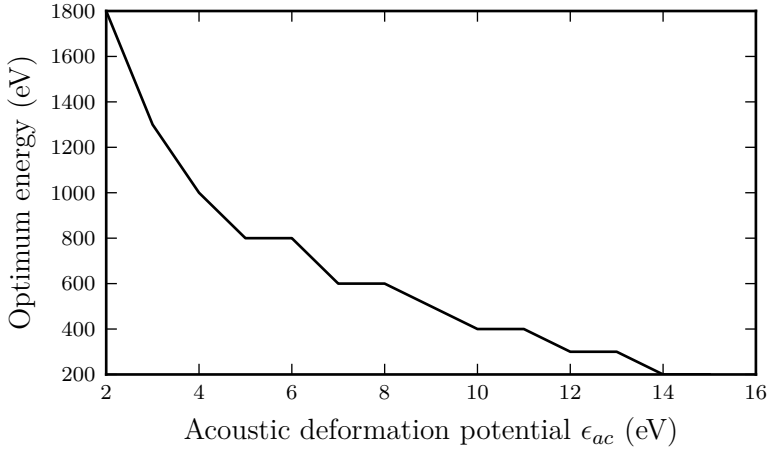
Figure 7.4: The optimum primary electron energy for magnesium oxide for different values of the acoustic deformation potential ϵ_{ac}.

on a tungsten, or tungsten coated with graphite, substrate [72]. Jokela et al. measured a maximum yield of almost 7 for a 200 nm magnesium oxide membrane on top of a boron doped silicon substrate [71]. The optimum primary energy ranges from approximately 600 eV to 1300 eV in the above mentioned experiments and hence can also not be used to 'fit' the acoustic deformation potential. Here we will choose an acoustic deformation potential of 4 eV. The maximum reflection secondary electron yield is then 6.95, at 1000 eV.

7.2 Simulated yield curves

We have simulated the secondary electron yield curves for different membrane thicknesses of magnesium oxide membranes. The simulation geometry was identical to the one depicted in Figure 4.1 in Chapter 4. The goal of these simulations is to find the optimum membrane thickness to get the highest transmission secondary electron yield as possible. In literature we found that magnesium oxide films suffer from charging effects when the film's thickness is too high. Especially for the last tynodes it is important to solve charge up

issues by either doping the tynode to create some conductance or by coating the tynode with a thin conducting layer. The first tynode however, will suffer significantly less from charge up effects since the absolute number of electrons emitted by this tynode will be small. This is why we will perform two different membrane thickness optimisations in this section; one for uncoated magnesium oxide membranes and one for chromium coated magnesium oxide membranes.
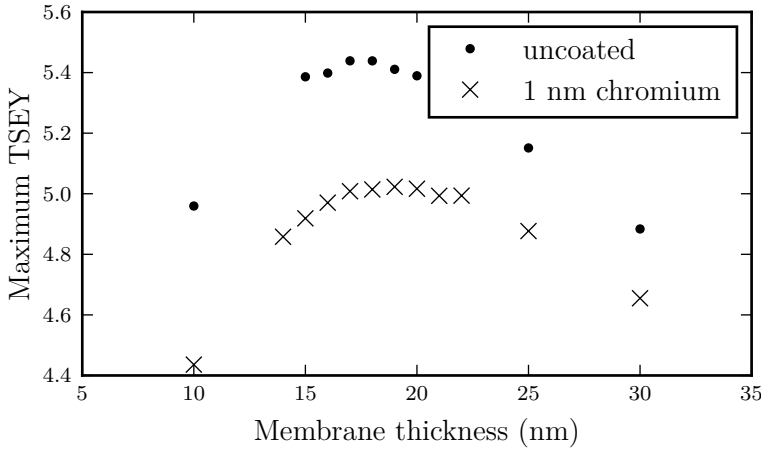
Figure 7.5: The maximum transmission secondary electron yield (TSEY) for magnesium oxide membranes depending on the membrane thickness. The maximum transmission secondary electron yield reaches its maximum value for a 17 nm membrane.

The maximum transmission secondary electron yield dependence on the membrane thickness is shown in Figure 7.5 for both the uncoated and the chromium coated magnesium oxide membranes. The chromium coated membranes have a 1 nm chromium coating on the top (i.e. the reflection side). We expect the chromium coating to decrease the reflection yield, since the secondary electron yield of chromium is lower than that of magnesium oxide. We also expect the transmission secondary electron yield to decrease since there will be extra material present (the chromium) in which less (transmission) secondary electrons are created than there would be in magnesium

Figure 7.6: The simulated yield curves for a 17 nm magnesium oxide membrane. The reflection secondary electron yield (R SEY, solid line) is higher than the transmission secondary electron yield (T SEY, dashed line) and has a lower optimum energy. The reflection backscatter electrons (R BSE, dash-dotted line) are already present at very low energies. The transmission backscatter electrons (T BSE, dotted line) only start to escape from the membrane at a primary energy of 600 eV.

oxide. In Figure 7.5 we indeed see that the maximum transmission secondary electron yield of the chromium coated magnesium oxide is lower than the maximum yield for the uncoated membranes. We also see that the optimum membrane thickness is 17 nm for uncoated and 19 nm for chromium coated magnesium oxide. The yield curves for the optimum membrane thicknesses are shown in Figures 7.6 and 7.7. The maximum transmission secondary electron yields are 5.4 at 1300 eV and 5.0 at 1550 eV for the uncoated and the chromium coated magnesium oxide respectively. We also see that the reflection secondary electron yield of the chromium coated membrane is significantly lower than for the uncoated membrane, just as we had expected.

In Chapter 1 we stated that a signal of 1000 electrons is necessary at the pixel input pads of a Timepix chip. With the yields of 5.4 and 5.0 for the uncoated and coated magnesium oxide, a stack of 5 tynodes will result in a signal of more than 1000 electrons per incoming electron at the first
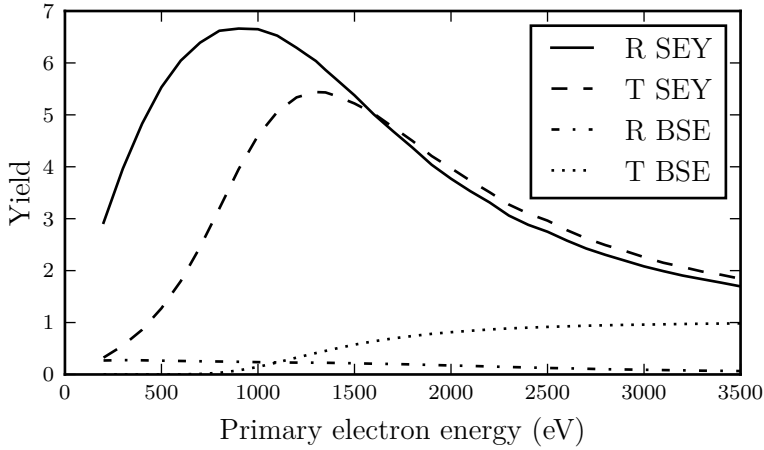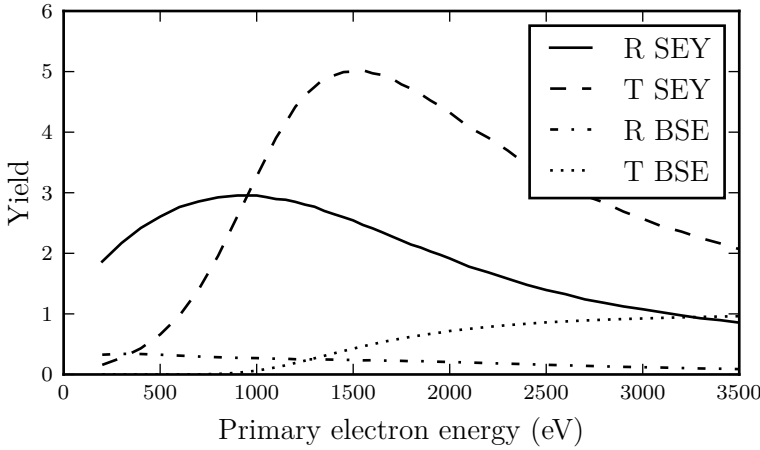
Figure 7.7: The simulated yield curves for a 19 nm chromium coated magnesium oxide membrane. The reflection secondary electron yield (R SEY, solid line) is lower than the transmission secondary electron yield (T SEY, dashed line) and has a lower optimum energy, due to the chromium coating. The reflection backscatter electrons (R BSE, dash-dotted line) are already present at very low energies. The transmission backscatter electrons (T BSE, dotted line) only start to escape from the membrane at a primary energy of 700 eV.

tynode. In Chapter 1 we also discussed the distance between the tynodes in relation to the voltage that can be put between two consecutive tynodes. We calculated that at 500 V 25 µm would be a safe distance. Now we see, however, that the optimum voltage would be 1300 V or 1550 V. This means the distance between the tynodes needs to be increased to 65 µm and 78 µm for uncoated and coated magnesium oxide respectively.

7.3   Secondary electron creation points

Now we can also look at the electron creation lengths for the coated and the chromium coated magnesium oxide membranes at their respective optimum thicknesses and optimum primary energies. In Figures 7.8 a) and c) we see the probability density functions for the creation points of secondary
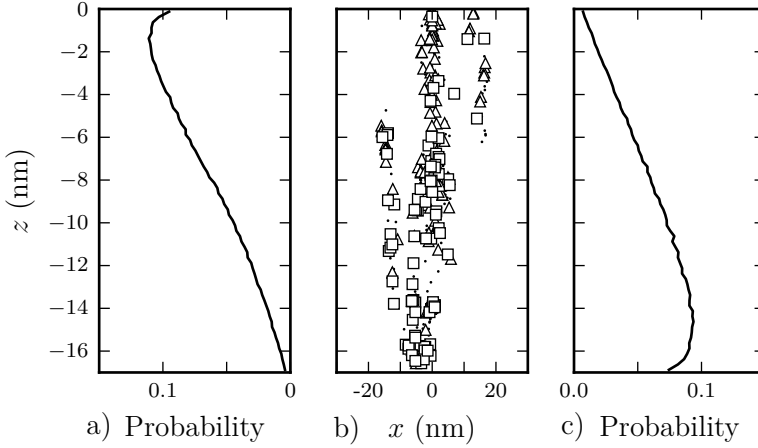
Figure 7.8: Simulation of a 17 nm magnesium oxide membrane, bombarded with 1300 eV electrons. The probability density function of the creation depth for electrons that leave the membrane on the top side (resp. bottom side) is shown in **a)** (resp. **c)**). Note that the probability density function is normalised with a bin width of 0.25 nm. **b)** All points where electrons are created during a simulation with 15 primary electrons are shown. The triangles and squares denote creation points of electrons that were able to escape on the reflection and transmission side respectively. The dots denote creation points of absorbed electrons. z is defined as the depth with respect to the irradiated surface. x is the distance to the beam position projected on the x-axis. Both axes are as defined in Figure 4.1.

electrons for the uncoated membranes in reflection and transmission mode respectively. When we fit Equation 4.1 we get $\lambda_{esc,R} = 7.89$ nm for reflection and $\lambda_{esc,T} = 10.81$ nm for transmission. The probability density functions for the creation points of secondary electrons for the chromium membranes in reflection and transmission mode are shown in Figures 7.9 a) and c) respectively. One big difference with the uncoated membrane is that there are almost no electrons created in the top 1 nm layer that are able to escape the membrane. Because of this we get an error when we try to fit Equation 4.1. Once we exclude the chromium coating from our fit, we get $\lambda_{esc,R} = 8.72$ nm in reflection mode and $\lambda_{esc,T} = 9.76$ nm in transmission mode. Note that the
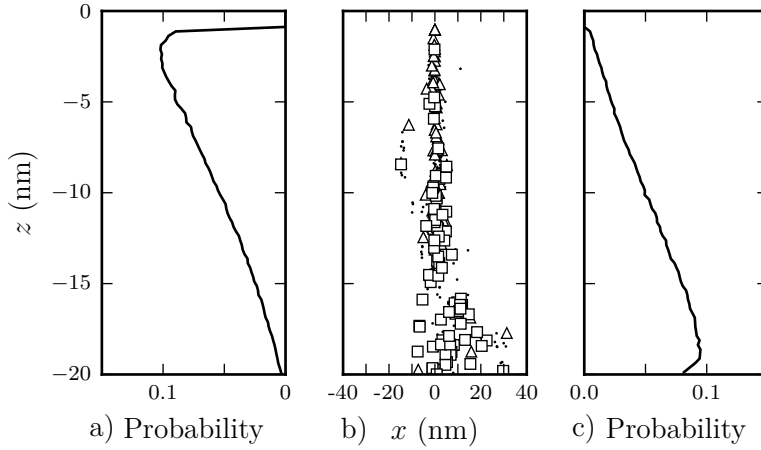
Figure 7.9: Simulation of a 19 nm magnesium oxide membrane coated with 1 nm chromium and bombarded with 1550 eV electrons. The probability density function of the creation depth for electrons that leave the membrane on the top side (resp. bottom side) is shown in **a)** (resp. **c)**). Note that the probability density function is normalised with a bin width of 0.25 nm. **b)** All points where electrons are created during a simulation with 15 primary electrons are shown. The triangles and squares denote creation points of electrons that were able to escape on the reflection and transmission side respectively. The dots denote creation points of absorbed electrons. z is defined as the depth with respect to the irradiated surface. x is the distance to the beam position projected on the x-axis. Both axes are as defined in Figure 4.1.

reflection secondary electrons still have to travel through the 1 nm chromium coating before they can escape; $\lambda_{esc,R}$ just describes the exponential decay of the probability density function of the creation points inside the magnesium oxide.

In Figures 7.8 b) and 7.9 b) we see the creation points of the secondary electrons in the uncoated and chromium coated membranes respectively. The shape of the 'creation' cloud for the chromium coated membrane starts out with a very small radius and flares out towards the bottom of the membrane. This is unlike the shape of the 'creation' cloud for the uncoated membrane, which has a more oval shape. It seems like the effect of the chromium layer is

that the primary electron energy has to be increased for the primary electrons to travel through the chromium and reach the magnesium oxide. Apparently, these electrons still have quite some residual energy left and the optimum membrane thickness for the magnesium oxide needs to be thicker than in the uncoated case in order to slow down the primary electrons to create secondary electrons.

7.4   Conclusion

In this chapter we have used the simulation package to determine the optimum thickness for prototype magnesium oxide tynodes. For uncoated membranes we determined that the optimum thickness is 17 nm, resulting in a maximum transmission secondary electron yield of 5.4 at 1300 eV.

However, magnesium oxide is known to suffer from charging effects, to overcome the charging effects, we could coat the top of the tynodes with a 1 nm chromium coating. In that case, the optimum membrane thickness becomes 19 nm + 1 nm chromium, resulting in a maximum transmission secondary electron yield of 5.0 at 1550 eV.

In both cases a stack of 5 tynodes is needed in order to end up with more than 1000 electrons after the last tynode per incoming electron.

Chapter 8

Conclusions

The purpose of this thesis research was to improve an existing simulation package so that it is able to predict the transmission secondary electron yields of tynode prototypes to be used for TiPC. In order to do this, we have further developed the electron interaction models from an existing simulation package. We also have extracted the mean free path calculations from the simulation package and developed the cross section tool. The new models reproduce experimental values for the (reflection) backscatter and secondary electron yields of silicon, gold and alumina slightly worse than the original models. However, the original models contained some errors and phenomenological parameters which are no longer present in the new models.

The simulation package can be used to simulate the dependence of the transmission secondary electron yield of a membrane on the membrane thickness. These simulations give insight in the differences between reflection and transmission secondary electron yields of membranes. The shape of the electron cloud inside the sample can be investigated as well as the dependence of the transmission secondary electron yield on the membrane thickness. As a result it is possible to optimise the membrane thickness to obtain the maximum transmission secondary electron yield and the accompanying optimum primary electron energy. This thickness optimisation was done for alumina membranes. The optimum membrane thickness of alumina membranes is 8 nm.

The simulation package can also be used in combination with *ab initio* density functional theory calculations. Density functional theory makes it possible to control the exact structure and composition of the material while calculating the necessary material parameters for a secondary electron simulation. In this way the effect of doping level and dopant distribution in a material can be investigated.

XPS experiments were performed in an attempt to get a measure of the secondary electron yield of silicon rich silicon nitride with different doping levels and different surface terminations. These experiments did not give absolute values for the yield and some of the samples suffered from charging effects. We were able, however, to determine that hydrogen termination increases the secondary electron yield of silicon rich silicon nitride. The simulation package was used in an attempt to reproduce the experimental XPS spectra. After taking the effects of the detector resolution and opening angle into account, there were still differences between the experimental and simulated spectra. This is mainly because the simulation package was not designed for this purpose and by trying to reproduce the experimental spectra, we have pushed the simulation package to its limits.

Finally we have used the simulation package to design prototype tynodes made of magnesium oxide. We have performed this optimisation for uncoated magnesium oxide and for magnesium oxide with a 1 nm chromium coating. In both cases a stack of 5 tynodes is needed in order to be able to realise the TiPC, however, the chromium coated membranes do need a higher primary energy to obtain their maximum transmission secondary electron yield.

We did succeed in developing a simulation package that can be used to simulate transmission secondary electron yields for membranes to help with the design of prototype tynodes to be used in the TiPC. The simulated yields should only be used qualitatively and not quantitatively, however. Once we have a candidate material, the simulation package can be used to optimise the membrane thickness. Then the range of thicknesses for prototypes tynodes can be narrowed down to a few different thicknesses close to the simulated optimum thickness. On top of that, it is easier to design experiments to measure the transmission secondary electron yield of the prototype tynodes,

since the simulations also predict a value for the optimum primary electron energy.

More work is necessary to develop a simulation package of which all results can be used quantitatively. Although it might be necessary to split the simulation package into smaller packages, each optimised for a specific material (group). However, during this project, the goal was also to have one all-round simulation package, thus concessions in the models are necessary. Another problem is that the necessary material parameters are not always available. So often we have to make an educated guess, and again the resulting secondary electron yield curves can only be used qualitatively instead of quantitatively. One example of a material parameter that is often unknown is the acoustic deformation potential. We have shown it is possible to make an educated guess of the acoustic deformation potential by simulating the yield curves for different values of the acoustic deformation potential and choosing the acoustic deformation potential such that the reflection secondary electron yield is close to experimental values. This 'fitted' acoustic deformation potential can then be used to optimise the membrane thickness for example. This is not ideal, however. The simple act of 'fitting' the acoustic deformation potential to experimental values introduces uncertainties, since quite often experimental parameters such as the exact composition and possible surface contamination of the sample are not known exactly.

Bibliography

[1] Erik Kieft and Eric Bosch. Refinement of monte carlo simulations of electron–specimen interaction in low-voltage SEM. *Journal of Physics D: Applied Physics*, 41(21):215310, 2008.

[2] H. Van der Graaf and J. L. Visschers. Photon detector with high time and high spatial resolution. *Patent no. NL1039339*, 2012.

[3] Yevgen Bilevych, Stefan E. Brunner, Hong Wah Chan, Edoardo Charbon, Harry van der Graaf, Cornelis W. Hagen, Gert Nützel, Serge D. Pinto, Violeta Prodanović, Daan Rotman, Fabio Santagata, Lina Sarro, Dennis R. Schaart, John Sinsheimer, John Smedley, Shuxia Tao, and Anne M. M. G. Theulings. Potential applications of electron emission membranes in medicine. *Nuclear Instruments and Methods in Physics Research Section A: Accelerators, Spectrometers, Detectors and Associated Equipment*, 809:171–174, 2016.

[4] H. van der Graaf, Michiel Bakker, H. W. Chan, Edoardo Charbon, Fabio Santagata, P. Sarro, and Dennis R. Schaart. The tipsy single soft photon detector and the trixy ultrafast tracking detector. In *IEEE Nuclear Science Symposium and Medical Imaging Conference*, 2012.

[5] V. Prodanović, H. W. Chan, J. Smedley, A. Theulings, S. Tao, H. v d Graaf, and P. M. Sarro. Optimization of silicon-rich silicon nitride films for electron multiplication in timed photon counters. *Procedia Engineering*, 120:1111–1114, 2015.

[6] V. Prodanović, H. W. Chan, H. V. D. Graaf, and P. M. Sarro. Ultra-thin alumina and silicon nitride MEMS fabricated membranes for the electron multiplication. *Nanotechnology*, 29(15):155703, 2018.

[7] S. Agostinelli et al. Geant4 - a simulation toolkit. *Nuclear Instruments and Methods in Physics Research Section A: Accelerators, Spectrometers, Detectors and Associated Equipment*, 506(3):250–303, 2003.

[8] X. Llopart, R. Ballabriga, M. Campbell, L. Tlustos, and W. Wong. Timepix, a 65k programmable pixel readout chip for arrival time, energy and/or photon counting measurements. *Nuclear Instruments and Methods in Physics Research Section A: Accelerators, Spectrometers, Detectors and Associated Equipment*, 581(1-2):485–494, 2007.

[9] S. Giere, M. Kurrat, and U. Schümann. HV dielectric strength of shielding electrodes in vacuum circuit-breakers. In *20th International Symposium on Discharges and Electrical Insulation in Vacuum*, Tours, France, 2002.

[10] T. Verduin. *Quantum Noise Effects in e-Beam Lithography and metrology.* Thesis, Delft University of Technology, 2017.

[11] Zbigniew Czyżewski, Danny O'Neill MacCallum, Alton Romig, and David C. Joy. Calculations of Mott scattering cross section. *Journal of Applied Physics*, 68(7):3066, 1990.

[12] N. F. Mott and N.H.D. Bohr. The scattering of fast electrons by atomic nuclei. *Proc. R. Soc. Lond. A*, 124, 1929.

[13] H. Raith. Komplexe Atomstreuamplituden für die elastische Elektronensteuung an Festkörperatomen. *Acta Crystallographica Section A*, 24(1):85–93, 1968.

[14] Francesc Salvat, Aleksander Jablonski, and Cedric J. Powell. ELSEPA—Dirac partial-wave calculation of elastic scattering of electrons and positrons by atoms, positive ions and molecules. *Computer Physics Communications*, 165(2):157–190, 2005.

[15] E. Schreiber and H. J. Fitting. Monte Carlo simulation of secondary electron emission from the insulator SiO_2. *Journal of Electron Spectroscopy and Related Phenomena*, 124(1):25–37, 2002.

[16] H. J. Fitting, E. Schreiber, J. Ch Kuhr, and A. von Czarnowski. Attenuation and escape depths of low-energy electron emission. *Journal of Electron Spectroscopy and Related Phenomena*, 119(1):35–47, 2001.

[17] M. Sparks, D. L. Mills, R. Warren, T. Holstein, A. A. Maradudin, L. J. Sham, E. Loh, and D. F. King. Theory of electron-avalanche breakdown in solids. *Physical Review B*, 24(6):3519–3536, 1981.

[18] J. N. Bradford and S. Woolf. Electron-acoustic phonon scattering in SiO_2 determined from a pseudo-potential for energies of $E \geq E_{BZ}$. *Journal of Applied Physics*, 70(1):490, 1991.

[19] R. G. Keys. Cubic convolution interpolation for digital image-processing. *IEEE Transactions on Acoustics Speech and Signal Processing*, 29(6):1153–1160, 1981.

[20] J. C. Ashley. Interaction of low-energy electrons with condensed matter: stopping powers and inelastic mean free paths from optical data. *Journal of Electron Spectroscopy and Related Phenomena*, 46(1):199–214, 1988.

[21] D. R. Penn. Electron mean-free-path calculations using a model dielectric function. *Physical Review B*, 35(2):482–486, 1987.

[22] S. T. Perkins, D. E. Cullen, and S. M. Seltzer. Tables and graphs of electron-interaction cross sections from 10 eV to 100 GeV derived from the LLNL evaluated electron data library (EEDL), Z = 1-100. *Report UCRL-50400 (Lawrence Livermore National Laboratory)*, 31, 1991.

[23] J. Zemek, P. Jiricek, B. Lesiak, and A. Jablonski. Surface excitations in electron backscattering from silicon surfaces. *Surface Science*, 562(1-3):92–100, 2004.

[24] J. Ch Kuhr and H. J. Fitting. Monte carlo simulation of electron emission from solids. *Journal of Electron Spectroscopy and Related Phenomena*, 105(2-3):257–273, 1999.

[25] D. E. Cullen, J. H. Hubbell, and L. Kissel. Tables and graphs of photon-interaction cross sections from 10 eV to 100 GeV derived from the LLNL evaluated photon data library (EPDL). *Report UCRL-50400 (Lawrence Livermore National Laboratory)*, 6, 1989.

[26] D. E. Cullen, J. H. Hubbell, and L. Kissel. EPDL: the Evaluated Photon Data Library, '97 version. *Report UCRL-50400 (Lawrence Livermore National Laboratory)*, 6, 1997.

[27] R. Shimizu and Z. J. Ding. Monte carlo modelling of electron-solid interactions. *Reports on Progress in Physics*, 55(4):487–531, 1992.

[28] J. P. Ganachaud and A. Mokrani. Theoretical study of the secondary electron emission of insulating targets. *Surface Science*, 334(1-3):329–341, 1995.

[29] Francesc Salvat, José M. Fernández-Varea, and Josep Sempau. *PENELOPE, a code system for Monte Carlo simulation of electron and photon transport.* NEA, 2011.

[30] B. L. Henke, E. M. Gullikson, and J. C. Davis. X-ray interactions: photoabsorption, scattering, transmission, and reflection at e=50-30000 ev, z=1-92. *Atomic Data and Nuclear Data Tables*, 54(2):181–342, 1993.

[31] F. Sauter. Über den atomaren Photoeffekt in der K-Schale nach der relativistischen Wellenmechanik Diracs. *Ann. Phys.*, 11, 1931.

[32] S. T. Perkins, D. E. Cullen, M. H. Chen, J. H. Hubbell, J. Rathkopf, and J. Scofield. Tables and graphs of atomic subshell and relaxation data derived from the LLNL evaluated atomic data library (EADL), Z=1-100. *Report UCRL-50400 (Lawrence Livermore National Laboratory)*, 30, 1991.

[33] Maurizio Dapor. Secondary electron emission yield calculation performed using two different monte carlo strategies. *Nuclear Instruments and Methods in Physics Research Section B: Beam Interactions with Materials and Atoms*, 269(14):1668–1671, 2011.

[34] Maurizio Dapor. Monte Carlo simulation of secondary electron emission from dielectric targets. *Journal of Physics: Conference Series*, 402:012003, 2012.

[35] David C. Joy. *A database of electron-solid interactions*. EM Facility, University of Tennessee, and Oak Ridge National Laboratory, 2008.

[36] G. F. Dionne. Effects of secondary electron scattering on secondary emission yield curves. *Journal of Applied Physics*, 44(12):5361–5364, 1973.

[37] Gerald F. Dionne. Origin of secondary-electron-emission yield-curve parameters. *Journal of Applied Physics*, 46(8):3347, 1975.

[38] D. C. Joy and C. S. Joy. SEMATECH Report TT# 96063130A-TR. 1996.

[39] L. Reimer and C. Tollkamp. Measuring the backscattering coefficient and secondary electron yield inside a scanning electron microscope. *Scanning*, 3(1):35–39, 1980.

[40] K. Kanaya and H. Kawakatsu. Secondary-electron emission due to primary and backscattered electrons. *Journal of Physics D-Applied Physics*, 5(9):1727, 1972.

[41] T. E. Rothwell and P. E. Russell. *Microbeam Analysis -1988*. San Francisco Press, San Francisco, 1988.

[42] N. R. Whetten. *Methods in Experimental Physics, and 1962 IV*. Academic Press: New York, NY, USA, 1962.

[43] I. M. Bronstein and B. S. Fraiman. *Vtorichnaya Elektronnaya Emissiya*. Nauka, Moscow, Russia, 1969.

[44] D. A. Moncrieff and P. R. Barker. Secondary electron emission in the scanning electron microscope. *Scanning*, 1(3):195–197, 1978.

[45] R. Böngeler, U. Golla, M. Kässens, L. Reimer, B. Schindler, R. Senkel, and M. Spranck. Electron-specimen interactions in low-voltage scanning electron microscopy. *Scanning*, 15(1):1–18, 1993.

[46] K. Kanaya and S. Ono. *Electron Beam Interactions with Solids.* SEM Inc.:Chicago, Chicago, 1984.

[47] D. M. Suszcynsky, J. E. Borovsky, and C. K. Goertz. Secondary electron yields of solar system ices. *J. Geophysical Res.*, 97(E2):2611–2619, 1992.

[48] M. S. Prasad. personal communication with D. C. Joy, 2002.

[49] M. M. El-Gomati and A. M. D. Assa'd. *On the Measurement of the Backscattering Coefficient for Low Energy Electrons*, pages 325–331. Springer Vienna, Vienna, 1998.

[50] P. H. Dawson. Secondary electron emission yields of some ceramics. *Journal of Applied Physics*, 37(9):3644, 1966.

[51] J. B. Johnson and K. G. McKay. Secondary electron emission of crystalline MgO. *Physical Review*, 91(3):582–587, 1953.

[52] Robert W. Christy. Formation of thin polymer films by electron bombardment. *Journal of Applied Physics*, 31(9):1680–1683, 1960.

[53] K. M. Poole. Electrode contamination in electron optical systems. *Proceedings of the Physical Society of London Section B*, 66(403):542–547, 1953.

[54] A. E. Ennos. The sources of electron-induced contamination in kinetic vacuum systems. *British Journal of Applied Physics*, 5(Jan):27–31, 1954.

[55] I. A. Glavatskikh, V. S. Kortov, and H. J. Fitting. Self-consistent electrical charging of insulating layers and metal-insulator-semiconductor structures. *Journal of Applied Physics*, 89(1):440–448, 2001.

[56] H. Bruining. The depth at which secondary electrons are liberated. *Physica*, 3:1046–1052, 1936.

[57] M. Roos, V. Baranauskas, M. Fontana, H. J. Ceragioli, A. C. Peterlevitz, K. Mallik, and F. T. Degasperi. Electron field emission from boron doped microcrystalline diamond. *Applied Surface Science*, 253(18):7381–7386, 2007.

[58] S. X. Tao, A. M. M. G. Theulings, V. Prodanovic, J. Smedley, and H. van der Graaf. Optical properties of silicon-rich silicon nitride ($Si_xN_yH_z$) from first principles. *Computation*, 3(4):657–669, 2015.

[59] O. Madelung, U. Rössler, and M. Schulz, editors. *Landolt-Börnstein - Group III Condensed Matter Volume 41A1β: 'Group IV Elements, IV-IV and III-V Compounds. Part b - Electronic, Transport, Optical and Other Properties'*. Springer-Verlag Berlin Heidelberg, accessed 2018.

[60] Edward D. Palik. *Handbook of Optical Constants of Solids*. Academic Press. Inc., 1997.

[61] P. Y. Yu and M. Cardona. *Fundamentals of Semiconductors: Physics and Material Properties*. Springer, 4th edition, Berlin 1996, fourth edition 2010.

[62] V. J. Tekippe, H. R. Chandrasekhar, P. Fisher, and A. K. Ramdas. Determination of the deformation-potential constant of the conduction band of silicon from the piezospectroscopy of donors. *Physical Review B*, 6(6):2348–2356, 1972.

[63] J. Smedley, S. Schubert, J. Xie, M. Ruiz-Osés, X. Liang, E. Muller, H. Padmore, J. Wong, S. Hulbert, A. M. M. G. Theulings, S. Tao, and H. van der Graaf. Electron emission processes in photocathodes and dynodes. In *2014 IEEE Nuclear Science Symposium and Medical Imaging Conference (NSS/MIC)*, pages 1–4, 2014.

[64] S. X. Tao, A. Theulings, J. Smedley, and H. van der Graaf. DFT study of electron affinity of hydrogen terminated β-Si_3N_4. *Diamond and Related Materials*, 53:52–57, 2015.

[65] S. X. Tao, A. M. M. G. Theulings, J. Smedley, and H. van der Graaf. DFT study of electron affinity of alkali metal termination on clean and oxygenated β-Si$_3$N$_4$. *Diamond and Related Materials*, 58:214–220, 2015.

[66] H. Zhou. *Auger line shape measurements using high resolution positron annihilation induced Auger electron spectroscopy*. Thesis, University of Texas at Arlington, 1996.

[67] Harry van der Graaf, Hassan Akhtar, Neil Budko, Hong Wah Chan, Cornelis W. Hagen, Conny C. T. Hansson, Gert Nützel, Serge D. Pinto, Violeta Prodanović, Behrouz Raftari, Pasqualina M. Sarro, John Sinsheimer, John Smedley, Shuxia Tao, Anne M. M. G. Theulings, and Kees Vuik. The tynode: A new vacuum electron multiplier. *Nuclear Instruments and Methods in Physics Research Section A: Accelerators, Spectrometers, Detectors and Associated Equipment*, 2016.

[68] Slade J. Jokela, Igor V. Veryovkin, Alexander V. Zinovev, Jeffrey W. Elam, Qing Peng, Anil U. Mane, Floyd D. McDaniel, and Barney L. Doyle. The characterization of secondary electron emitters for use in large area photo-detectors. *AIP Conference Proceedings*, 1336:208–212, 2011.

[69] P. K. de Boer and R. A. de Groot. The conduction bands of MgO, MgS and HfO$_2$. *Journal of Physics: Condensed Matter*, 10(45):10241–10248, 1998.

[70] D. van Heijnsbergen, G. von Helden, G. Meijer, and M. A. Duncan. Infrared resonance-enhanced multiphoton ionization spectroscopy of magnesium oxide clusters. *J. Chem. Phys.*, 116(6):2400, 2002.

[71] S. J. Jokela, I. V. Veryovkin, A. V. Zinovev, J. W. Elam, A. U. Mane, P. Qing, and Z. Insepov. Secondary electron yield of emissive materials for large-area micro-channel plate detectors - surface composition and film thickness dependencies. *TIPP 2011 – Technology and Instrumentation in Particle Physics 2011*, 2011.

[72] N. Rey Whetten and A. B. Laponsky. Secondary electron emission of single crystals of MgO. *Journal of Applied Physics*, 28(4):515–516, 1957.

[73] Y. Ushio, T. Banno, N. Matuda, Y. Saito, S. Baba, and A. Kinbara. Secondary-electron emission studies on MgO films. *Thin Solid Films*, 167(1-2):299–308, 1988.

[74] http://www.webelements.com, 1993.

[75] K. Ohya, A. Chen, J. Kawata, K. Nishimura, D. Kato, T. Tanabe, and T. Kato. *ELECTRAN - Monte Carlo Program of Secondary Electron Emission from Monoatomic Solids under the Impact of 0.1 - 10 keV Electrons.* National Institute for Fusion Science, Toki, Japan, 1984.

[76] G. Chiarotti, editor. *Landolt-Börnstein - Group III Condensed Matter 24C: 'Interaction of Charged Particles and Atoms with Surfaces'.* Springer-Verlag Berlin Heidelberg, accessed 2018.

[77] https://ecee.colorado.edu/~bart/book/effmass.htm, 1997.

[78] U. Rössler and D. Strauch, editors. *Landolt-Börnstein - Group III Condensed Matter Volume 41A1α: 'Group IV Elements, IV-IV and III-V Compounds. Part α - Lattice Properties'.* Springer-Verlag Berlin Heidelberg, 2001.

[79] N. W. Ashcroft and N. D. Mermin. *Solid State Physics.* Brooks/Cole, Cengage Learning, Belmont, USA, 1976.

[80] W. M. Haynes, D. R. Lide, and T. J. Bruno. *CRC Handbook of Chemistry and Physics.* CRC Press, Boca Raton, Florida, 92nd edition, 2011.

[81] Elena O. Filatova and Aleksei S. Konashuk. Interpretation of the changing the band gap of Al2O3 depending on its crystalline form: Connection with different local symmetries. *The Journal of Physical Chemistry C*, 119(35):20755–20761, 2015.

[82] D. V. Morgan, A. E. Guile, and Y. Bektore. Stored charge in anodic aluminium oxide films. *Journal of Physics D: Applied Physics*, 13(2):307–312, 1980.

[83] R. G. Munro. Evaluated material properties for a sintered alpha-al$_2$o$_3$. *Journal of the American Ceramic Society*, 80:1919–1928, 1997.

[84] J. Shan, F. Wang, E. Knoesel, M. Bonn, and T. F. Heinz. Measurement of the frequency-dependent conductivity in sapphire. *Phys Rev Lett*, 90(24):247401, 2003.

[85] D. Gray, A. McCaughan, and B. Mookerji. Crystal structure of graphite, graphene and silicon. *Lecture*, (Cambridge: Massachusetts Institute of Technology), 2009.

[86] S. Ono and K. Sugihara. Theory of the transport properties in graphite. *Journal of Physical Society of Japan*, 21(5), 1966.

[87] Alan R. Selfridge. Approximate material properties in isotropic materials. *IEEE Transactions on Sonics and Ultrasonics*, 32(3):381–394, 1985.

[88] S. X. Tao. private communications. 2015.

[89] `https://ptable.com/`, 2017.

[90] W. Schaaffs, K.-H. Hellwege, and A. M. Hellwege, editors. *Landolt-Börnstein - Group II Molecules and Radicals 5 : '(Molecular Acoustics)'*. Springer-Verlag Berlin Heidelberg, accessed 2018.

[91] Ç. Kılıç and A. Zunger. n-type doping of oxides by hydrogen. *Applied Physics Letters*, 81(73), 2002.

[92] O. Madelung, U. Rössler, and M. Schulz, editors. *Landolt-Börnstein - Group III Condensed Matter Volume 41B: 'II-VI and I-VII Compounds; Semimagnetic Compounds'*. Springer-Verlag Berlin Heidelberg, accessed 2018.

Appendix A

Material parameters

Silicon

The parameters Kieft and Bosch used to define silicon are:

ρ_m	$= 2.33$ g/cm^3,	mass density
E_F	$= 7.83$ eV,	Fermi energy
E_G	$= 1.12$ eV,	band gap
EA	$= 4.05$ eV,	electron affinity
a	$= 5.43$ Å,	lattice constant
M_D	$= 1m_e$,	density of states mass
m_e^*	$= 1m_e$,	effective electron mass[1]
M	$= 28.1$ g/mole,	atomic mass
c_s	$= 9040$ m/s,	sound velocity
ϵ_{ac}	$= 9.2$ eV,	acoustic deformation potential

The parameters we used are:

ρ_m	$= 2.3290$ g/cm^3 [74]
E_F	$= 7.83$ eV [75]
E_G	$= 1.12$ eV [1]
EA	$= 4.05$ eV [1]
a	$= 5.430710$ Å [76]
M_D	$= 1.08m_e$ [77]

---

[1]From now on we will omit the values for M_D and m_e^* when both are equal to $1m_e$.

m_e^* $= 0.26 m_e$ [77]

M $= 28.0855$ g/mole [74]

Longitudinal phonon parameters:

α $= 2.00 \cdot 10^{-7}$ m^2/s [10],   parameter related to bending of dispersion relation

c_s $= 9130$ m/s [78]

ϵ_{ac} $= 9.2$ eV [78]

Transversal phonon parameters:

α $= 2.26 \cdot 10^{-7}$ m^2/s [10]

c_s $= 5842$ m/s [78]

ϵ_{ac} $= 5.0$ eV [78]

Gold

The parameters Kieft and Bosch used to define gold are:

ρ_m $= 19.3$ g/cm^3

E_F $= 9.11$ eV

W_f $= 5.38$ eV,   work function

M $= 196.97$ g/mole

ρ_R $= 2.44 \cdot 10^{-8}$ Ωm,   resistivity

The parameters we used are:

ρ_m $= 19.30$ g/cm^3 [74]

E_F $= 5.53$ eV [79]

W_f $= 5.38$ eV [75]

a $= 4.0782$ Å [76]

M $= 196.97$ g/mole [74]

ρ_R $= 2.2 \cdot 10^{-8}$ Ωm [74]

Longitudinal phonon parameters:

c_s $= 3240$ m/s [80]

ϵ_{ac} $= 4.86$ eV   (calculated)

Transversal phonon parameters:

c_s $= 1200$ m/s [80]

ϵ_{ac} $= 1.80$ eV (calculated)

Alumina

The parameters Kieft and Bosch used to define alumina are:

ρ_m $= 3.98$ g/cm^3

E_G $= 7.0$ eV

EA $= 1.0$ eV

a $= 4.76$ Å

M_{Al} $= 26.98$ g/mole

M_O $= 16.0$ g/mole

c_s $= 8010$ m/s

ϵ_{ac} $= 13.0$ eV

The parameters we used are:

ρ_m $= 3.98$ g/cm^3 [1]

E_F $= 0.0$ eV [81]

E_G $= 7.0$ eV [81]

EA $= 1.0$ eV [82]

a $= 4.76$ Å [83]

M_{Al} $= 26.982$ g/mole [74]

M_O $= 15.999$ g/mole [74]

Single phonon parameters:

c_s $= 8009$ m/s [83] weighted average of longitudinal and transversal sound velocity

ϵ_{ac} $= 13.0$ eV [84]

Silicon dioxide

ρ_m $= 2.648$ g/cm^3 [80]

E_F $= 0.0$ eV [1]

E_G $= 9.0$ eV [1]

EA $= 0.9$ eV [1]

a $= 5.45$ Å [1]

M_{Si} $= 28.085$ g/mole [74]

M_O $= 15.999$ g/mole [74]

Single phonon parameters:

c_s $= 3560$ m/s [1]

ϵ_{ac} $= 2.6$ eV [1]

Graphite

ρ_m $= 2.267$ g/cm^3 [74]

E_F $= 8.64$ eV [1]

E_G $= 0.0$ eV [1]

EA $= 4.6$ eV [1]

a $= 2.46$ Å [76, 85]

M $= 12.011$ g/mole [74]

Longitudinal phonon parameters:

c_s $= 21000$ m/s [86]

ϵ_{ac} $= 16.2$ eV [86]

Transversal phonon parameters:

c_s $= 3960$ m/s [86]

ϵ_{ac} $= 3.73$ eV [86]

Silicon nitride (Si$_3$N$_4$)

ρ_m $= 3.27$ g/cm^3 [87]

E_F $= 7.5602$ eV [58]

E_G $= 4.7$ eV [58]

EA $= 1.5$ eV [1]

a $= 5.2647$ Å [58]

M_{Si} $= 28.0855$ g/mole [74]

M_N $= 14.007$ g/mole [74]

Single phonon parameters:

c_s $= 7833$ m/s [87]

ϵ_{ac} $\quad = 12.0$ eV

Silicon nitride ($Si_{13}N_{15}$)

ρ_m $\quad = 3.27$ g/cm^3 [87]

E_F $\quad = 7.8376$ eV [58]

E_G $\quad = 4.4$ eV [58]

EA $\quad = 1.5$ eV [1]

a $\quad = 6.8115$ Å [58]

M_{Si} $\quad = 28.0855$ g/mole [74]

M_N $\quad = 14.007$ g/mole [74]

Single phonon parameters:

c_s $\quad = 7833$ m/s [87]

ϵ_{ac} $\quad = 12.0$ eV

Silicon nitride (homogeneous Si_7N_7)

ρ_m $\quad = 3.27$ g/cm^3 [87]

E_F $\quad = 9.8$ eV [58]

E_G $\quad = 3.9$ eV [58]

EA $\quad = 1.5$ eV [1]

a $\quad = 10.5$ Å [58]

M_{Si} $\quad = 28.0855$ g/mole [74]

M_N $\quad = 14.007$ g/mole [74]

Single phonon parameters:

c_s $\quad = 7833$ m/s [87]

ϵ_{ac} $\quad = 12.0$ eV

Silicon nitride (clustered Si_7N_7)

ρ_m $\quad = 3.27$ g/cm^3 [87]

E_F $\quad = 9.9834$ eV [58]

E_G $\quad = 3.6$ eV [58]

EA = 1.5 eV [1]

a = 10.5294 Å [58]

M_{Si} = 28.0855 g/mole [74]

M_N = 14.007 g/mole [74]

Single phonon parameters:

c_s = 7833 m/s [87]

ϵ_{ac} = 12.0 eV

Silicon nitride (amorphous Si_7N_7)

ρ_m = 3.27 g/cm^3 [87]

E_F = 9.5434 eV [88]

E_G = 3.5 eV [88]

EA = 1.5 eV [1]

a = 10.6612 Å [88]

M_{Si} = 28.0855 g/mole [74]

M_N = 14.007 g/mole [74]

Single phonon parameters:

c_s = 7833 m/s [87]

ϵ_{ac} = 12.0 eV

Silicon nitride ($Si_7N_7H^{Si}$)

ρ_m = 3.27 g/cm^3 [87]

E_F = 9.2148 eV [58]

E_G = 4.5 eV [58]

EA = 1.5 eV [1]

a = 5.3306 Å [58]

M_{Si} = 28.0855 g/mole [74]

M_N = 14.007 g/mole [74]

Single phonon parameters:

c_s = 7833 m/s [87]

ϵ_{ac} = 12.0 eV

Silicon nitride ($Si_7N_7H^N$)

ρ_m	= 3.27 g/cm^3 [87]
E_F	= 10.2520 eV [58]
E_G	= 3.4 eV [58]
EA	= 1.5 eV [1]
a	= 5.3306 Å [58]
M_{Si}	= 28.0855 g/mole [74]
M_N	= 14.007 g/mole [74]

Single phonon parameters:

c_s	= 7833 m/s [87]
ϵ_{ac}	= 12.0 eV

Silicon nitride ($Si_7N_7H^{Si,N}$)

ρ_m	= 3.27 g/cm^3 [87]
E_F	= 9.8418 eV [58]
E_G	= 3.9 eV [58]
EA	= 1.5 eV [1]
a	= 5.3306 Å [58]
M_{Si}	= 28.0855 g/mole [74]
M_N	= 14.007 g/mole [74]

Single phonon parameters:

c_s	= 7833 m/s [87]
ϵ_{ac}	= 12.0 eV

Chromium

ρ_m	= 7.19 g/cm^3 [89]
E_F	= 7.25 eV [75]
W_f	= 4.5 eV [75]
a	= 2.91 Å [74]

M $= 51.996$ g/mole [74]

ρ_R $= 1.25 \cdot 10^{-7}$ Ωm [89]

Longitudinal phonon parameters:

c_s $= 6850$ m/s [90]

ϵ_{ac} $= 17.1$ eV (calculated)

Transversal phonon parameters:

c_s $= 3980$ m/s [90]

ϵ_{ac} $= 10.0$ eV (calculated)

Magnesium oxide

ρ_m $= 3.58$ g/cm^3 [1]

E_F $= 0.0$ eV [1]

E_G $= 7.8$ eV [69, 70]

EA $= 1.37$ eV [91]

a $= 4.2112$ Å [69]

M_{Mg} $= 24.305$ g/mole [74]

M_O $= 15.999$ g/mole [74]

Single phonon parameters:

c_s $= 3231$ m/s [92]

ϵ_{ac} $= 4.0$ eV

Appendix B

Simulation package

The simulation package is split into two modules; the cross section tool and the Monte Carlo tool. The cross section tool is written in Python and can be found on `https://github.com/eScatter/cstool` as the *cstool* package. The Monte Carlo simulation package is based upon GEANT4 and can be found on `https://github.com/eScatter/lowe-g4/tree/hdf5`. A flow-chart detailing the simulation package can be found at the end of this appendix in Figure B.1.

We would like to point out that the latest version of the Monte Carlo package is found in the *hdf5* branch of the *lowe-g4* package and that this only works with the *tmfp* branch of the *cstool* package `https://github.com/eScatter/cstool/tree/tmfp`.

The simulation package used in this work is based upon GEANT4, which is a very big package and is not optimised for these kind of simulations in terms of calculation speed.

Below we will give a quick overview of the steps needed to run a simulation with the simulation package used in this thesis. Although in theory it is possible to install both packages on Windows, we have not tested this and the installation steps assume the package is going to be used under Linux.

B.1 Cross section tool

The cross section tool is a tool for compiling the cross sections for a material in a .mat file that will be used by the Monte Carlo simulation package to define a material. Here we will include a manual for installing the cross section tool *cstool* based on the README on `https://github.com/eScatter/cstool/blob/tmfp/README.rst`. This will be followed by a short explanation of the different files necessary when a new material is added. Currently, the *cstool* module needs both the *pyelsepa* and *cslib* packages to be installed, preferably in a VirtualEnv (so that you don't muck-up your Python installation).

B.1.1 Installation

Before installing the *cstool* first Docker needs to be installed. This can be found at `https://www.docker.com/` and has its own manuals. We will not repeat those here, but assume Docker is already installed. To setup an environment for *cstool*, first make sure you have the correct version of Python (these commands may vary slightly from system to system):

```
> python3 --version # version should be 3.5 or higher
Python 3.5.3
```

clone the needed repositories:

```
> git clone http://github.com/eScatter/cslib.git
...
> git clone http://github.com/eScatter/pyelsepa.git
...
> git clone -b tmfp http://github.com/eScatter/cstool.git
...
```

create a virtual environment:

```
> python3 -m venv cstool-env
...
> source ./cstool-env/bin/activate
```

```
(cstool-env) >
```

You may need to update pip at this point:

```
> pip install --upgrade pip
```

Now we need to install cslib and pyelsepa:

```
(cstool-env) > cd cslib
(cstool-env) ./cslib> pip install .
(cstool-env) ./cslib> cd ../pyelsepa
(cstool-env) ./pyelsepa> pip install .
(cstool-env) ./pyelsepa>
```

And we have to install the Docker image for ELSEPA, make sure you have downloaded adus_v1_0.tar.gz:

```
(cstool-env) ./pyelsepa> docker -v # make sure you have the
    latest
Docker version 1.13.1, build 092cba372
(cstool-env) ./pyelsepa> cd docker
(cstool-env) ./pyelsepa> ls
adus_v1_0.tar.gz Dockerfile README.md
(cstool-env) ./pyelsepa> docker build -t elsepa .
...
Successfully built <some hex-code>
```

Now we need to install cstool:

```
(cstool-env) ./pyelsepa> cd ../cstool
(cstool-env) ./cstool> pip install .
```

Now we need to get the data files for ionisation:

```
(cstool-env) ./cstool> cd data/endf
(cstool-env) ./cstool/data/endf> . fetch-endf.sh
(cstool-env) ./cstool/data/endf> unzip ENDF-B-VII.1-
    atomic_relax.zip
```

```
(cstool-env) ./cstool/data/endf> unzip ENDF-B-VII.1-electrons.
    zip
```

Now you should be ready to run the example in examples/cs.py:

```
(cstool-env) ./cstool> ENDF_DIR=./data/endf python examples/cs.
    py data/materials/silicon.yaml
```

B.1.2 Defining a new material

In order to define a new material, the *cstool* needs two input files; a .yaml file containing the material parameters in the `data/materials` directory and a .dat file containing the energy loss function in the `data/elf` directory. The contents of the `silicon.yaml` file are shown below. Example files for gold and alumina are also included in the *cstool* package.

```
name: silicon
rho_m: 2.3290 g/cm³ # Mass density
elf_file: data/elf/df_Si.dat # Directory and name of the file
    with the energy loss function

band_structure:
    model: semiconductor # Other options are insulator and
        metal
    fermi: 7.83 eV # Fermi energy
    band_gap: 1.12 eV # Band gap
    affinity: 4.05 eV # Electron affinity

phonon:
    model: dual # For silicon the dual branch acoustic phonon
        model is used
    lattice: 5.430710 Å # Lattice constant
    m_dos: 1.08 m_e # Density of state mass, default is 1 m_e
    m_eff: 0.26 m_e # Effective mass, default is 1 m_e
    single: # In case the single phonon model is used
```

```
        c_s: 6938 m/s # Speed of sound
        eps_ac: 6.4 eV # Acoustic deformation potential
    longitudinal: # Parameters for longitudinal branch
        alpha: 2.00e-7 m²/s # Parameter relating to bending of
            dispersion relation, default is 0 m²/s
        c_s: 9130 m/s # Speed of sound
        eps_ac: 9.2 eV # Acoustic deformation potential
    transversal: # and transversal branch parameters
        alpha: 2.26e-7 m²/s # Parameter relating to bending of
            dispersion relation, default is 0 m²/s
        c_s: 5842 m/s # Speed of sound
        eps_ac: 5.0 eV # Acoustic deformation potential

elements:
    Si: { count: 1, Z: 14, M: 28.0855 g/mol }
```

Below the contents of the df_Si.dat file are also included. The first line contains the binding energies of the outer shell electrons in the material. These are all the binding energies below 100 eV. Binding energies above 100 eV will be disregarded by the simulation package, since in that case the binding energies of EPDL97 [25, 26] will be used. For silicon, the list of binding energies starts with the band gap of 1.12 eV. The line ends with -1, to signal that this is the complete list of outer shell binding energies. Note that for silicon the K shell binding energy (1839 eV) is also included. This will be disregarded in the simulation as this energy is larger than 100 eV (and is certainly not an outer shell binding energy). The next lines until the end of the file contain the energy loss function. Each line has two values; the energy in eV and the value of the energy loss function (unitless). The last line with −1 −1 signals the end of the file.

```
1.12 5 8.9 100 1839 -1
0.01116 1.45249E-05
0.04959 4.57441E-06
0.07191 1.82492E-05
```

```
0.07513 6.24973E-05
0.08307 6.19974E-06
0.09051 1.51494E-05
0.09919 8.83799E-06
0.1103 1.03996E-05
0.1289 1.83492E-06
0.1376 4.22982E-06
0.1736 8.39965E-07
0.1798 1.22495E-06
0.248 9.89653E-09
0.4568 1.22902E-10
1.06 6.87849E-08
1.1 5.91084E-07
1.5 0.000201807
2 0.000738292
2.5 0.001809896
3 0.003758113
3.5 0.020559831
4 0.024934123
4.3 0.021016573
5.2 0.057223291
5.36 0.054990309
6 0.061012204
8 0.106934663
10 0.211555291
11 0.313137224
12.5 0.646758418
14 1.489513067
16 3.614241782
18 3.06515778
20 0.877669987
25.3 0.08694452
30.24 0.043370068
```

```
40 0.024858833
49.59 0.015144286
59.04 0.009529418
82.66 0.003635796
99.19 0.001809121
102 0.048723208
150 0.032988672
201 0.016760782
250 0.008623961
504 0.000826479
1016 6.78875E-05
1815 7.86209E-06
1860 8.16167E-05
2000 6.38182E-05
4000 5.12708E-06
8000 3.54308E-07
-1 -1
```

B.2   Monte Carlo simulation package

The simulation package is based on GEANT4 and as such it needs GEANT4 to be installed. Now there are two options if anyone wants to install the simulation package, either they follow the README on `https://github.com/eScatter/lowe-g4/blob/hdf5/README.md`. This README assumes the reader is familiar with the installation procedure of GEANT4. Or, the far easier option, the reader can use the Dockerfile on `https://github.com/eScatter/lowe-g4/tree/hdf5/docker`. In both cases, one needs to download GEANT4.10.02.p02.tar.gz, note that the simulation package will not work out of the box with any other version of GEANT4 than exactly this version. At the time of writing, this version of GEANT4 is available at `http://cern.ch/geant4-data/releases/geant4.10.02.p02.tar.gz`. In the next section we will detail the installation of the simulation package

using the Dockerfile.

B.2.1   Installation

Here we assume Docker is already installed, otherwise we refer to the Docker website for downloads and manuals: `https://www.docker.com/`. Once Docker is installed, the Monte Carlo simulation package can be installed with the following steps:

```
wget http://cern.ch/geant4-data/releases/geant4.10.02.p02.tar.
    gz
wget https://github.com/eScatter/lowe-g4/blob/hdf5/docker/
    Dockerfile
docker build -t geant4 .
```

This last statement built a docker image named `geant4`. This image can be used to run simulations, but the data will not be stored permanently and will be lost once the image is exited. In order to keep the data, a docker container needs to be made from the image:

```
docker run -it --name geant4container geant4
```

From now on the container can be started with:

```
docker start -ai geant4container
```

Once the container is running, one can find a small example in `/usr/src/lowe-g4/Examples/Transmission` which can be run with:

```
./run.sh
```

B.2.2   Running a simulation

In the directory `Examples/Transmission` multiple files are found that all combined form the input for one simulation. Here we will list the files and folders present with a short explanation of what is in the file.

1. The directory `Kieft_and_Bosch_materialfile`; This directory contains one file; `KB_SEMmaterials.xml` which contains the material definitions from Kieft and Bosch [1] as were in the original simulation package. We have included this as a reference if one wants to add a new material.

2. The directory `mac`; This directory contains two files; `Pointsource.mac`, which contains the definition of the primary particle source, and `energy.mac`, in which the energy of the particle source is set and the output files are defined.

3. `BulkSample.gdml`; This file contains the geometry of the sample and the detectors.

4. `SEMmaterials.xml`; This file contains the definition of the material name and the density (needed for GEANT4).

5. `YieldCurve.gdml`; This file reads in the geometry from `BulkSample.gdml` and sets which volumes are the detectors.

6. `YieldCurve.mac`; This file contains the GEANT4 macro to run the simulation, the primary energies to be used in the simulation are set in this file.

7. `run.sh`; This file calls the GEANT4 macro and sets the material of the sample.

8. `silicon.mat.hdf5`; This is the material file which is output by the *cstool*.

We encourage the interested reader to look at the files on `https://github.com/eScatter/lowe-g4/tree/hdf5/Examples/Transmission`. Below we will put a small example of what steps are necessary in order to define a new material and use it in a simulation.

First the material, for example gold, needs to be calculated with the *cstool*. The output file `gold.mat.hdf5` needs to be copied to the `Examples/Transmission` directory. Then the definition of gold needs to be added to the file `SEMmaterials.xml`:

```
 <material Z="79" formula="Au" name="gold" >
  <D value="19.30" />
  <atom value="196.97" />
 </material>
```

Now all we need to do is set the material in `run.sh` to silicon instead of gold, or alternatively, if we wanted to run two consecutive simulations, we could set `run.sh` to:

```
#!/bin/sh
job=results
for material in silicon gold
do
        echo Starting job for ${material}
        sed "s/MATERIAL/${material}/g" YieldCurve.mac > Yield${
            material}.mac
        SEM YieldCurve.gdml Yield${material}.mac > Yield${
            material}.log 2>&1
        echo Done with job ${job} for ${material}
done
```

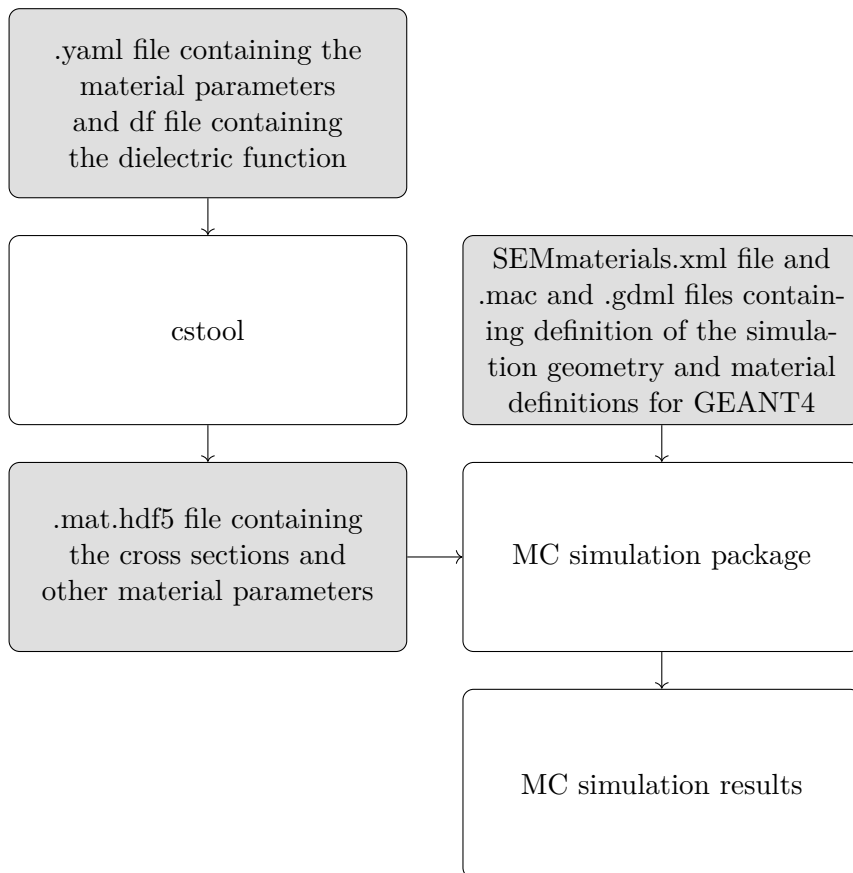This would run two simulations, first one for a silicon sample and then one for a gold sample.

Figure B.1: Flowchart of the simulation package.

Dankwoord

Al vanaf het eerste practicum dat ik tijdens mijn studie deed, wilde ik promoveren. Deze wens ben ik de rest van mijn studie blijven koesteren en ik wil mijn promotor Harry van der Graaf er dan ook voor bedanken dat hij mij de mogelijkheid heeft geboden om daadwerkelijk te promoveren. Hij heeft mij de vrijheid gegeven om binnen zijn onderzoek mijn eigen richting te kiezen en telkens moedigde hij mij aan om elke kans die ik kreeg met beide handen aan te pakken; ik mocht naar elke conferentie die ik interessant vond en geen cursus was te veel. Toen ik begon aan mijn promotie wist ik nog niet wat ik 'later' wilde worden. Door alle mogelijkheden die ik tijdens mijn promotie heb gekregen van Harry, heb ik dit voor mezelf uit kunnen zoeken en daar ben ik hem zeer dankbaar voor.

Ook ben ik veel dank verschuldigd aan mijn tweede promotor Kees Hagen. Pas halverwege mijn promotie werd hij mijn dagelijks begeleider en later ook een van mijn promotoren. Ik zat op dat moment vast en wist zelf niet goed meer hoe ik verder kon met het onderzoek. Tijdens zeer fijne vakinhoudelijke discussies heeft Kees mij geholpen om door de bomen het bos te zien en om weer vertrouwen te krijgen in mijn eigen vaardigheden.

Dit proefschrift had er heel anders uitgezien wanneer Erik Kieft en Eric Bosch van FEI Company niet bereid waren geweest tot het delen en openbaar maken van hun simulatiepakket. Hiervoor en voor hun bereidwilligheid om de natuurkundige modellen te bespreken, wil ik beide bedanken. Het was heel bijzonder om te zien dat Erik Kieft van alles terug kon vinden in jaren oude aantekeningen wanneer wij met een ingewikkelde vraag kwamen over hun simulatiepakket.

The next two people I would like to thank do not speak Dutch, so I will thank them in English. I would like to thank John Smedley for his interest in my research and for giving us the possibility to perform XPS experiments in Brookhaven National Laboratory. Even after I left the US he continued the experiments up until the NSLS was decommissioned. When I was back at home in the Netherlands, he was my contact if I had questions about the setup used in the experiments or anything else necessary to interpret the experimental results.

I would also like to thank Shuxia Tao for helping me to get started during the first two years of my PhD. Together we found the article of Kieft and Bosch that led us to their simulator. Shuxia also performed the *ab initio* density functional theory simulations that I used in my Monte Carlo simulations to define silicon rich silicon nitride. I would like to thank her for her contribution to my PhD research.

Ook wil ik Johannes Hidding van eScience Center bedanken. Zijn bijdrage aan de *cstool* is zeer waardevol geweest. Hij heeft de opzet van de *cstool* in Python gemaakt, waardoor wij onze aandacht volledig op de modellen konden richten.

Vaak wordt een promotieonderzoek binnen een en dezelfde afdeling uitgevoerd. Ik heb het genoegen gehad om niet op een, maar op drie verschillende locaties te mogen werken. Bij deze wil ik alle collega's van RID, MInT en Nikhef hartelijk bedanken voor de prettige sfeer en de vele al dan niet werkgerelateerde discussies die hebben bijgedragen aan mijn persoonlijke ontwikkeling. In het bijzonder wil ik Kerim Arat, Luc van Kessel en Thomas Verduin bedanken voor de prettige samenwerking tijdens de tweede helft van mijn promotie.

Een promotieonderzoek kan natuurlijk niet worden uitgevoerd zonder de steun van familie en vrienden. Ik ben dan ook zeer dankbaar dat ik deze in overvloed heb mogen ontvangen. In het bijzonder wil ik mijn ouders Henk en Anita, zus Erica en broer Maarten bedanken. Zij hebben mij altijd aangemoedigd mijn hart te volgen en staan altijd klaar met een luisterend oor of advies. Henk, Nel en Erica hebben daarnaast vele woensdagen op Tijmen opgepast, zodat ik rustig kon schrijven. Zonder hun hulp had het

aanzienlijk langer geduurd voor dit proefschrift eindelijk af was.

Ook wil ik Terry bedanken, mijn steun en toeverlaat, je maakt me altijd aan het lachen wanneer het nodig is en ook wanneer het juist even niet zou moeten. Jij hebt mij door de dieptepunten gesleept en je zorgt ervoor dat ik genoeg tijd vrij maak om te genieten van het leven. Samen kunnen we genieten van onze mooie zoon Tijmen, die nu net wakker begint te worden van zijn middagdutje.

Annemarie Theulings
Bleiswijk, december 2019